ISSN 2367-7570

Workshop
"Solar Influences on the Magnetosphere, Ionosphere and Atmosphere"

Book of Proceedings

Eighth Workshop

Sunny Beach, Bulgaria, May 30 - June 3, 2016

Organized by:

Space Research and Technologies Institute

Bulgarian Academy of Sciences

Scientific Organizing Committee

Editors: **Katya Georgieva, Dimitar Danov, Boian Kirov**

CONTENT

CONTENT

Proceedings of
Eighth Workshop "Solar Influences on the Magnetosphere, Ionosphere and Atmosphere"
Sunny Beach, Bulgaria, *May 30 - June 3, 2016*

Decameter Solar Drift-Pair Bursts

Stanislavsky A.[1,2], *Konovalenko A.* [1], *Koval A. 1, Volvach Ya.*[1]

[1] Institute of Radio Astronomy of the NASU, Ukraine;
[2] V.N. Karazin Kharkiv National University, Ukraine
E-mail: astex@ukr.ua

Abstract

In this consideration we give a new sight on the study of the solar bursts historically called drift pairs (DPs). Having a simple morphology on dynamic spectra of radio records (two short components separated in time, and often they are very similar) and discovered at the dawn of radio astronomy, their features remain unexplained totally up to now. Generally, the DPs are observed during the solar storms of type III bursts, but not every storm of type III bursts is associated with DPs. Detected by ground-based instruments at decameter and meter wavelengths, the DP bursts are limited in frequency bandwidth. They can drift from high frequencies to low ones and vice versa. Their frequency drift rate may be both lower and higher than typical rates of type III bursts at the same frequency range. The development of low-frequency radio telescopes and data processing provide additional possibilities in the research. In this context the fresh observations of DPs, performed during the summer campaign of 2015, are just discussed. They were implemented by updated tools of the UTR-2 radio telescope at 9-33 MHz. This allows us to get new information about such bursts in decameter wavelengths.

Introduction

The drift-pair bursts have long been known [1], but the understanding of the mechanism of their generation is not as successful for the type III bursts or the type II bursts. The DPs appear as two parallel drifting ridges, similar to each other, on the dynamic spectrum. Most of the radio observations of such bursts were performed at 60-80 years of the last century [2-7]. The most recent papers [8,9] were devoted to the study of decameter drift-pair bursts by utilizing the radio telescope UTR-2 [10]. The manifestations of solar DP activity occur at decameter and meter wavelengths (up to 80 MHz) during the solar storms of the type III bursts. The relationship between the DPs and the type III bursts are unclear so far. In recent years, thanks to advances in low-frequency radio astronomy, the quality of radio observations of solar bursts by ground-based instruments has increased significantly (see, for example, [11] and references therein). The aim of this report is to present recent observations of DPs useful for the study of their properties as well as for finding interrelations between them.

Observations and Facilities

During the observations, the UTR-2 radio telescope was operated in the mode including four sections of the north-south array of the antenna. The total effective area of these four sections is 50 000 m^2 with the beam pattern size of $1^o \times 15^o$ at 25 MHz. The solar radio emission was received from the antenna to the digital receiver/spectrometer operating with the time resolution of 50 ms and the frequency resolution of 4 kHz. On 10-12 July 2012 we observed some hundreds of solar DP bursts with both forward and reverse drift (see, as an example, the dynamic spectrum on Figure 1). Most of the registered DPs were really pairs on the dynamic spectrum, but we have also detected some vertical DPs as well as several single and multiple bursts like DPs. The frequency drift rate of DPs varies from event to event in the frequency range 9-33 MHz and in time. The drift rate histogram of forward DPs (or briefly FDPs) was a symmetric shape with the average equal to about -0.74 ± 0.28 MHz s^{-1}, whereas for reverse DPs (RDPs) the mean becomes 1.36 MHz s^{-1} under the histogram with a long tail. Basically the flux of the DP bursts was some hundreds s.f.u. Recall here that 1 s.f.u. $=10^{-22}$

W/(Hz m^2). In each drift pair we can distinguish two components almost identical in frequency-time properties. Each of them had the duration equal to about 1-2 s, and the time delay between the components was 1.5-2.5 s.

On 10-12 July of 2015, according to the space-based observations of STEREO, GOES and SOHO, the solar activity was weak, i.e. some C-class X-ray flares. The solar events were accompanied with the active regions NOAA AR 12381 located N14W25 on 10 July of 2015. The sunspot group belonged to the magnetic β class.

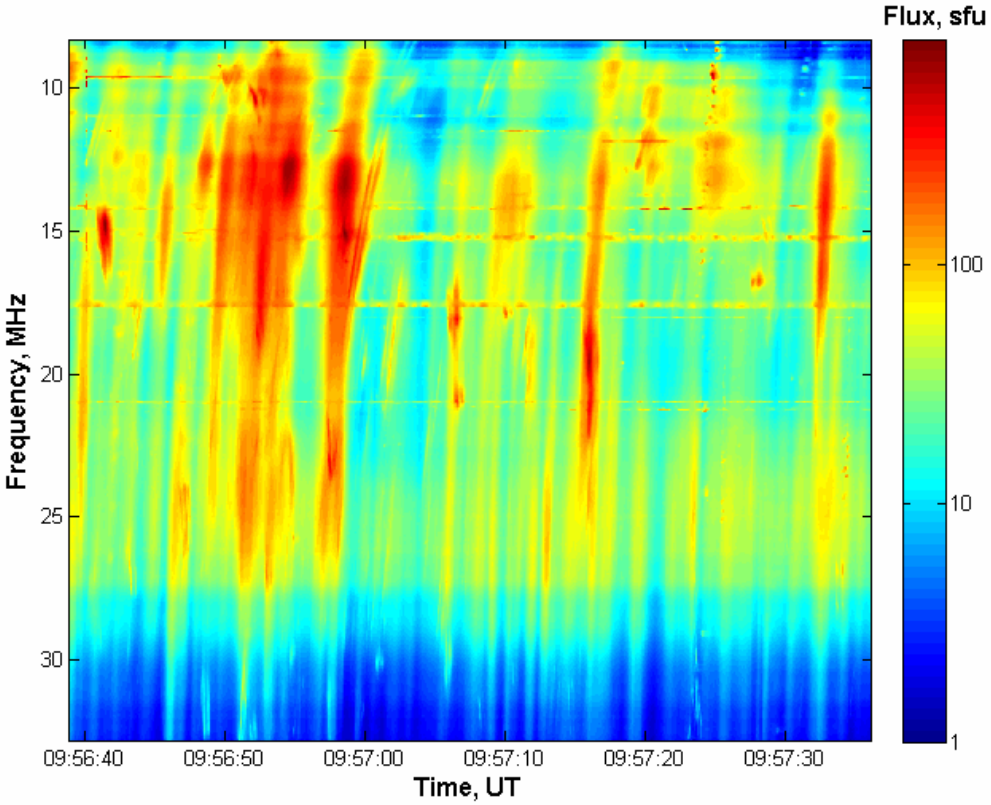

Fig.1. Illustrative dynamic spectrum of the drift-pair bursts imposed on type III bursts obtained from the UTR-2 observations on 11 July of 2015. The horizontal bright lines on the dynamic spectrum were caused by intensive interferences due to broadcast radio stations.

Interpretations

The simplest interpretation of the DP generation was based on the assumption that the drift pairs are similar to the type III bursts in the mechanism of generation, but the first component escapes directly from the corona whereas the second component is a reflection (an echo) [1]. Unfortunately, any similar "echo" for other types of bursts is not observed. On the other hand, the scattering of the reflected radiation would produce the second element more diffuse (than the first component) not observed too. The contradictions have led to the development of other models for understanding the mechanism provoking the generation of DPs [4,5,12-14]. Their detailed analysis was presented in [8,15]. The main outcome of this overview is that most of the interpretations can explain only a limited number of characteristics typical for DPs, and any simple interpretation based on one or two observational facts like frequency drift rate and so on will not explain all the features of the DPs self consistently.

In this context the theory of Zaitsev and Levin [14] can be considered as promising. The model is based on the excitation of plasma waves in those layers of the corona where the condition of double plasma resonance is satisfied. This approach provides some very

important clues to understand the strange cases of DPs such as vertical DPs, DP chains and others. Any other model [4,5,12,13] cannot explain their generation. In fact, the vertical DPs, which occur simultaneously in all the frequencies, are difficult to interpret by means of a moving source, as any exciting agent responsible for such bursts will travel with velocities faster than velocity of light that is impossible. Nevertheless, the formula of frequency drift rate for DPs derived in [14] contains the denominator tending to zero under certain conditions. First this feature has been noticed by Thejappa [15]. However, the general solution of this task has not been found yet. Thus, it would be useful to consider the problem.

For this purpose, we write the denominator equal to zero as a differential equation (see more details in [14,15])

$$\frac{1}{2N_e}\frac{\partial N_e}{\partial z} - \frac{1}{H}\frac{\partial H}{\partial z} = A\frac{\sqrt{N_e}}{H}, \tag{1}$$

where N_e is the electron density of the solar corona, H the magnetic field strength, A the constant (under assumptions of [15] it was equal to 0. 00093). If we denote $M = \sqrt{N_e}/H$, then the above equation takes the simplest form

$$\frac{1}{M}\frac{\partial M}{\partial z} = AM. \tag{2}$$

Its solution reads

$$M(z) = \frac{M(0)}{1 - AM(0)z^2}, \tag{3}$$

where $M(0) = \sqrt{N_e(0)}/H(0)$ is the boundary condition. If, as an example, we use the Dulk-McClean model of magnetic field strength $H(z) = 0.5(z + a - 1)^{-1.5}$ [16] and the Newkirk model of electron density $N_e = 4.2 \times 10^4 \times 10^{4.2/(z+a)}$ [17] for solar corona, then the formula (4.9) of [15] will be obtained right away whereas the formula (4.13) of [15] gives an rough estimate only. In particular, the parameter $a = 1.4$ corresponds to the plasma frequency equal to ~65 MHz in the Newkirk model [15]. It should be pointed out that the found solution includes two variables, $N_e(z)$ and $H(z)$. Only one of them may be independent whereas another will be dependent on the former. As $M = \sqrt{N_e}/H$ is a fraction, there are two different cases in the behavior of $N_e(z)$ and $H(z)$. Observe that the variable $M(z)$ tends to infinity as $z \to z_{cr}$. Therefore, if the electron density (independent variable) decreases with height in solar corona, then the magnetic field strength (dependent one) drops too. But if the magnetic field strength (independent variable) falls with height, then the electron density (dependent one) will tend to infinity. In any case the result of this analysis will be the same, i.e. the frequency drift rate of such DPs tends to infinity in the framework of this theory [14].

Now therefore, more detailed radio observations of DPs (with high resolution) require building a new model of DP generation. As it is not yet, any empirical study, i.e. the searching of empirical implicit dependences between DP properties, is of undoubted interest.

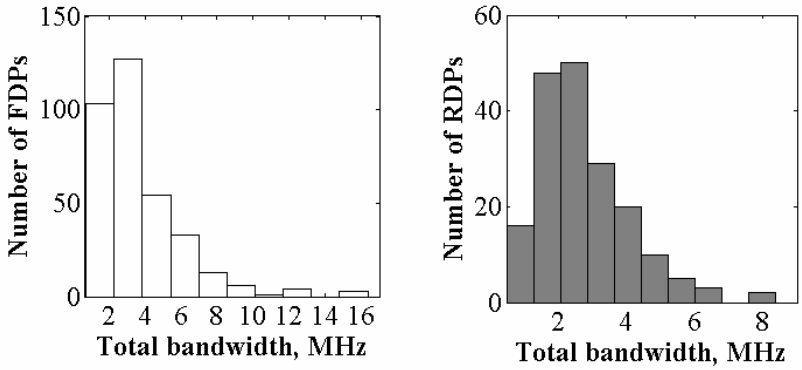

Fig.2. Frequency bandwidth histograms obtained for FDPs and RDPs according to the observations in 10-12 July of 2015.

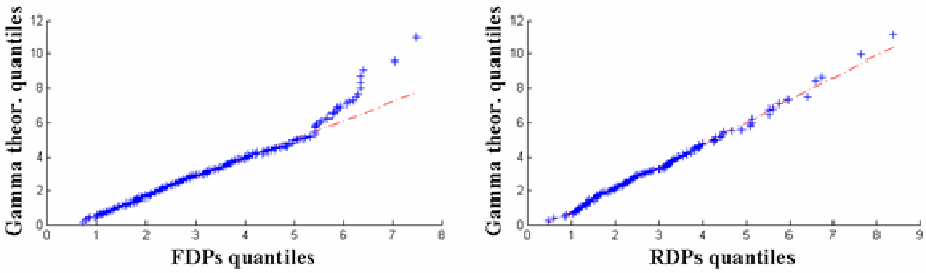

Fig.3. Q-Q plot used to compare both FDPs and RDPs samples with a theoretical Gamma distribution sample.

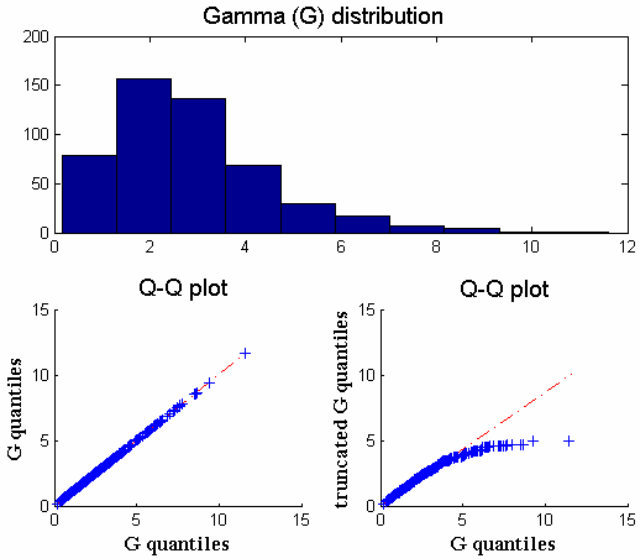

Fig.4. Numerical simulation of random samples with the Gamma distribution (histogram drawing top). The Q-Q plots present two cases: the left picture compares two ordinary Gamma theoretical samples whereas the right panel indicates a difference between the theoretical Gamma sample and its truncated sample.

Results

The total frequency bandwidth of DPs is one of simple parameters which are easy to measure in the radio data. In the frequency range of our radio instrument the DP bursts have clearly a limited frequency bandwidth. Their appearance in frequency-time plane (dynamic spectrum) has a random nature. The same goes for the central frequency of DPs. The total frequency bandwidth was determined for each component of any DP observed in our session of observations. This relative value is equal to the difference between the maximum frequency and minimum one, which we established in each recorded DP. Unfortunately, our observations do not permit us to cover the entire radio band where the DPs originate. It is interesting to note that the observations clearly showed that high-frequency edges of the long DPs were located upward the frequency band of the UTR-2 radio telescope. This imposes certain restrictions on the results. This problem will be considered further. Figure 2 presents the frequency-bandwidth distributions of DPs.

The obtained histograms of random values (frequency bandwidth) are clearly asymmetric, i.e. they should be characterized at least by three moments (mean, variation and skewness). This case may correspond to the Gamma distribution [18]. This assumption has been verified by the quantile-quantile (Q-Q) plot used to compare experimental samples with a theoretical distribution sample [19]. At first we have compared two random samples (FDPs and RDPs) by the Q-Q plot. From this it follows that the samples have almost the same distribution for the values of FDPs from the smallest bandwidths up to ~10 MHz as well as in RDPs from the smallest ones up to ~7 MHz. However, the long DPs (with the bandwidth about 8-15 MHz) have different distributions in these species. This is not surprising because in our experimental data the long DPs had a forward drift, as a rule. This was confirmed, if the long DPs were deleted from the samples.

The next important step is to detect the distribution itself for bandwidths of FDPs and RDPs, respectively. With this in mind we compare the collections of data with samples governed by the theoretical Gamma distribution. The corresponding Q-Q plots are seen in Figure 3. Indeed, the experimental samples obey the Gamma distribution, especially it concerns to RDPs. By numerical simulations (see Figure 4) we can explain the influence of the truncation of sample observations on the Q-Q plot. Consequently, the truncation leads to the deviation of the left picture shown in Figure 3.

Summary

Following the study, we have established that the total frequency bandwidth of DPs has a random nature and satisfies the Gamma distribution. Some deviations from this distribution take place because the observations had a limited frequency band. Therefore, a part of the DP sample was not received by our instrument. Nevertheless, this did not prevent to fulfill the statistical analysis of DP properties. In the future we plan to provide our observations of DPs by means of a new ukrainian ultrabroadband radio telescope GURT (Giant Ukrainian Radio Telescope) being built now in Ukraine [11]. It has a wider frequency band for solar observations (from 10 to 80 MHz) that will be enough to cover almost the entire frequency range of solar radio emission where DPs occur.

Acknowledgements

We thank the GOES and SOHO teams for developing and operating the instruments and we are grateful for their open data policy. This research was partially supported by Research Grant "Synchronized simultaneous study of radio emission of solar system objects by low-frequency ground- and space-based astronomy" from the National Academy of Sciences of Ukraine.

References

[1] Roberts J.A. Evidence of echoes in the solar corona from a new type of burst // Aust. J. Phys. – 1958. – 11. – P:215-234.
[2] de la Noë J., Møller-Pedersen B. Relationship between drift pair bursts and decametre type III solar radio emission // Astron. Astrophys. – 1971. – 12. – P:371-378.
[3] Ellis G.R.A. Fine structure in the spectra of solar radio bursts // Aust. J. Phys. – 1969. – 22. – P:177-188.
[4] Møller-Pedersen B., Smith R.A., Mangeney A. A theory of a solar radio burst - The drift pair // Astron. Astrophys. – 1978. – 70. – P:801-813.
[5] Abranin E.P., Bazelian L.L., Goncharov N.Iu., et al. Some results of observations of solar radio bursts of the 'drifting pairs' type near frequencies of 25 and 12.5 MHz // Sov. Astron. – 1977. – 21. – P: 82-88.
[6] Suzuki S., Gary D.E. Position and polarization of solar drift pair bursts // Proc. Astron. Soc. Australia. – 1979. – 3. – P:379-383.
[7] Thejappa G., Gopalswamy N., Sastry C.N., Aubier M.G. Some interesting features in the drift pair phenomena of solar decametric radiation // ESA Spec. Publ., ESA SP-251. – 1986. – P:121-125.
[8] Melnik V.N., Konovalenko A.A., Dorovskyy V.V., et al. Solar drift pair bursts in the decameter range // Solar Phys. – 2005. – 231. – P:143-155.
[9] Litvinenko G.V., Shaposhnikov V.E., Konovalenko A.A., et al. Quasi-similar decameter emission features appearing in the solar and jovian dynamic spectra // Icarus. – 2016. – 272. – P: 80–87.
[10] Braude S.Ya., Megn A.V., Ryabov B.P., Sharykin N.K., Zhouck I.N. Decametric survey of discrete sources in the Northern sky. I - The UTR-2 radio telescope: Experimental techniques and data processing // Astrophys. and Space Sci. – 1978. – 54. – P:3-36.
[11] Konovalenko A., Sodin L., Zakharenko V., et al. The modern radio astronomy network in Ukraine: UTR-2, URAN and GURT // Experim. Astron. – 2016. – 41. – P:1-38.
[12] Zheleznyakov V.V. On the origin of solar radio bursts in the meter-wavelength range // Sov. Astron. – 1965. – 9. – P: 191-197.
[13] Melrose D.B. Fine structures in decametric noise storms: possible mechanisms // in Benz A.O. and Zlobec P. (eds.), Proc. of the 4th CESRA Workshop on "Solar Radio Storms", Trieste Observatory, Trieste. – 1982. – P:182-218.
[14] Zaitsev V.V., Levin B.H. On the mechanism of generation of solar radio bursts of the "drifting pairs" type // Sov. Astron. – 1978. – 22. – P:223-227.
[15] Thejappa G. The radio bursts from the outer corona // PhD thesis, Bangalore University, 1988.
[16] Dulk G.A., McLean D.J. Coronal magnetic fields // Solar Phys. – 1978. – 57. – P:279-295.
[17] Newkirk C.Jr. Coronal magnetic fields // in Macris C.J. (ed.) "Physics of the Solar Corona", D.Reidel, Dordrecht . – 1971. – P: 66-87.
[18] Meyer P.L. Introductory probability and statistical applications, 2nd ed., Addison-Wesley, Reading, MA, 1970.
[19] Wilk M.B., Gnanadesikan R. Probability plotting methods for the analysis of data // Biometrika (Biometrika Trust) . – 1968. – 55. – P:1-17.

Proceedings of
Eighth Workshop "Solar Influences on the Magnetosphere, Ionosphere and Atmosphere"
Sunny Beach, Bulgaria, *May 30 - June 3, 2016*

Properties of the Long Drift-Pair Bursts from Decameter Observations of 2015

Volvach Ya.[1], *Stanislavsky A.*[1,2], *Konovalenko A.* [1], *Koval A.* [1]

[1] Institute of Radio Astronomy of the NASU, Ukraine;
[2] V.N. Karazin Kharkiv National University, Ukraine
E-mail: yarvolvach@ukr.net

Abstract

In this report we consider the solar drift-pair (DP) bursts forming the longest patterns on dynamic spectra obtained from the UTR-2 radio telescope observations at 9-33 MHz during 10-12 July of 2015. The experimental study was carried out with high time (50 ms) and frequency (4kHz) resolution. This set of DPs includes about 7% of the total number of recorded DPs. Their patterns occupied about 8-15 MHz in the frequency band. As a rule, the long DPs drifted from higher to lower frequencies (forward DPs) except for one reverse long DP, drifting from lower to higher frequencies. According to our observational data in July of 2015, the average frequency bandwidth was 3.6 MHz for forward DPs, whereas for reverse DPs it was 2.82 MHz. Our basic attention was focused on the frequency drift rates of the long bursts. Their resemblance with the solar S-bursts is discussed.

Introduction

The investigations of solar drift-pair (DP) bursts have been launched with the pioneering work of Roberts in 1958 [1]. He was the first who drew attention to a special form of radiation observing from the solar corona. Each of such bursts consists of two short components separated in time, the second repeating the first on dynamic spectra of the radio emission. DPs are relatively rare events which occur during the solar storms of type III bursts [2]. They drift from high frequencies to low ones and vice versa. Attempts to find an explanation for this manifestation of solar activity were taken by the scientific community in many times, but origins of many features of DPs remain unclear up to now.

The last comprehensive studies of DP properties from the observations of solar radio emission in July of 2002 were presented by Melnik et al. [4]. However, the observations used the analog multichannel receiver (10-30 MHz), tuned to selected 60 frequencies with the frequency bandwidth 10 kHz in each frequency channel, and DSP (Digital Spectral Polarimeter) was carried out the fast Fourier analysis in the continuous frequency band 17.6-29.8 MHz with frequency (12 kHz) and time (100 ms) resolution. In the present days the observations of DPs can be performed with higher time and frequency resolution from 9 to 33 MHz due to the progress in the receiving equipment. The aim of this study is to update the previous results concerning the DPs in decameter wavelengths.

Observations

The solar data from the UTR-2 antenna array were recorded by a new two-channel digital receiver/spectrometer [3] in the continuous frequency band of 9-33 MHz with the time resolution of 50 ms and the frequency resolution of 4 kHz. In the solar observations on 10-12 July of 2015 we have obtained 301 DP bursts from which 92 were reverse DPs (RDP), and 209 were forward DPs (FDP). For forward DPs the average frequency bandwidth was 3.6 MHz, whereas for reverse DPs it was 2.82 MHz. We have selected the longest ones of them. They contained 20 long FDPs and the only one long RDP. Their bandwidth was about 8-15 MHz. As an example, the dynamic spectrum of such long DPs is shown in Figure 1.

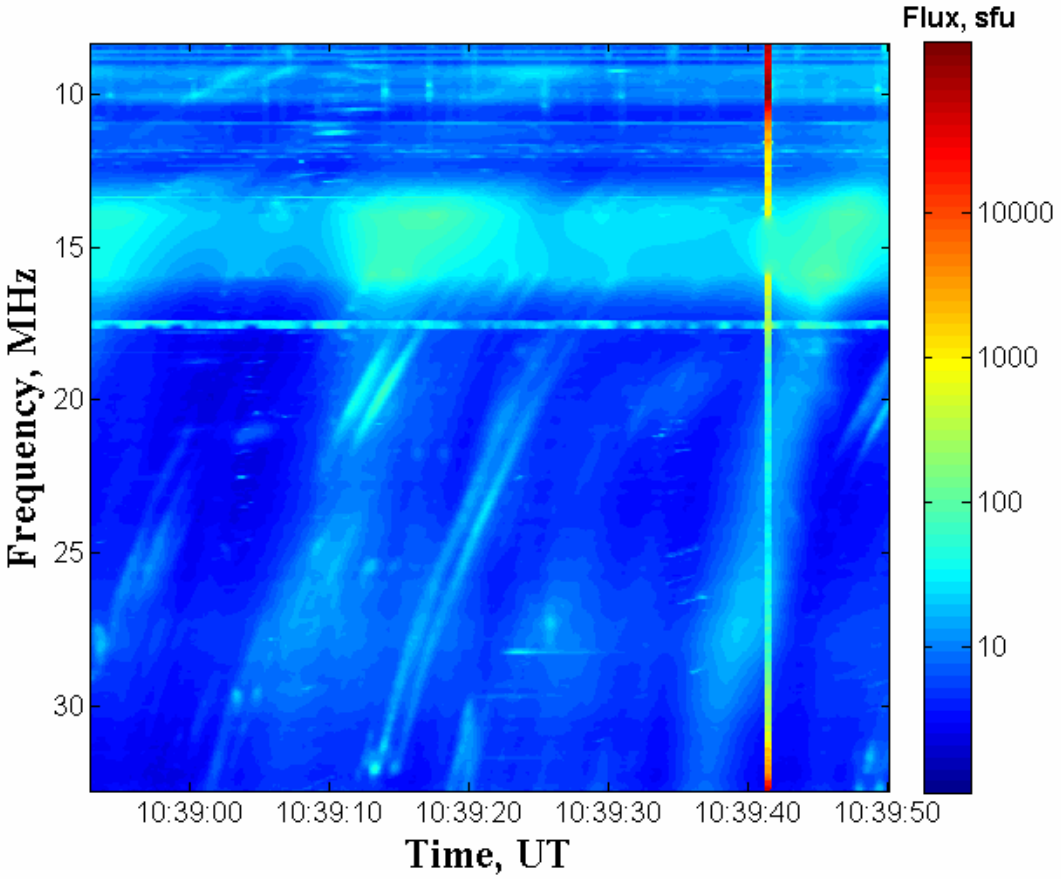

Fig.1. Dynamic spectrum of some long DPs recorded by the UTR-2 radio telescope on 11 July 2015. Here the bright vertical line indicates a phase shifter switching, and the conspicuous horizontal line was caused by interferences.

The occurrence of the DPs and the storm of type III bursts in 10-12 July of 2015 was associated with active regions on the solar disc. At that time the most active region was NOAA AR 12381 (N14W25 on 10 July of 2015). On the day before it was located near the central meridian (see more details in http://www.solarmonitor.org/).The sunspot group belonged to the magnetic β class, having both positive and negative magnetic polarities with a simple division between them. The solar activity was accompanied by some weak solar X-ray flares of C class.

Data Processing

Although the DP bursts are similar in appearance on dynamic spectra, they differ in frequency bandwidth, central frequency, total duration, slope and others. The frequency drift properties of long DPs are matter of the present analysis. To determine the best function fitting the frequency drift of DPs, for each component of DPs we found the time t_i for each frequency $f_i i$ (within the frequency band, where the given DP was detected) corresponding to the "centre" of the intensity hump for the DP burst under consideration. As a fitting function, we take the form

$$f(t) = a(t-b)^{-\gamma}, \tag{1}$$

where a,b,γ are the parameters leading to the best-fitting result. It is not difficult to show that in this case the frequency drift rate satisfies to the relation

$$\dot{f}(f) = Kf^{\nu}, \tag{2}$$

where K and ν are the constants, depending only on a and γ, namely $K=-\gamma a^{-1/\gamma}$ (negative drift rate) and $\nu=1+1/\gamma$. Note that the doted symbol means the time derivative.

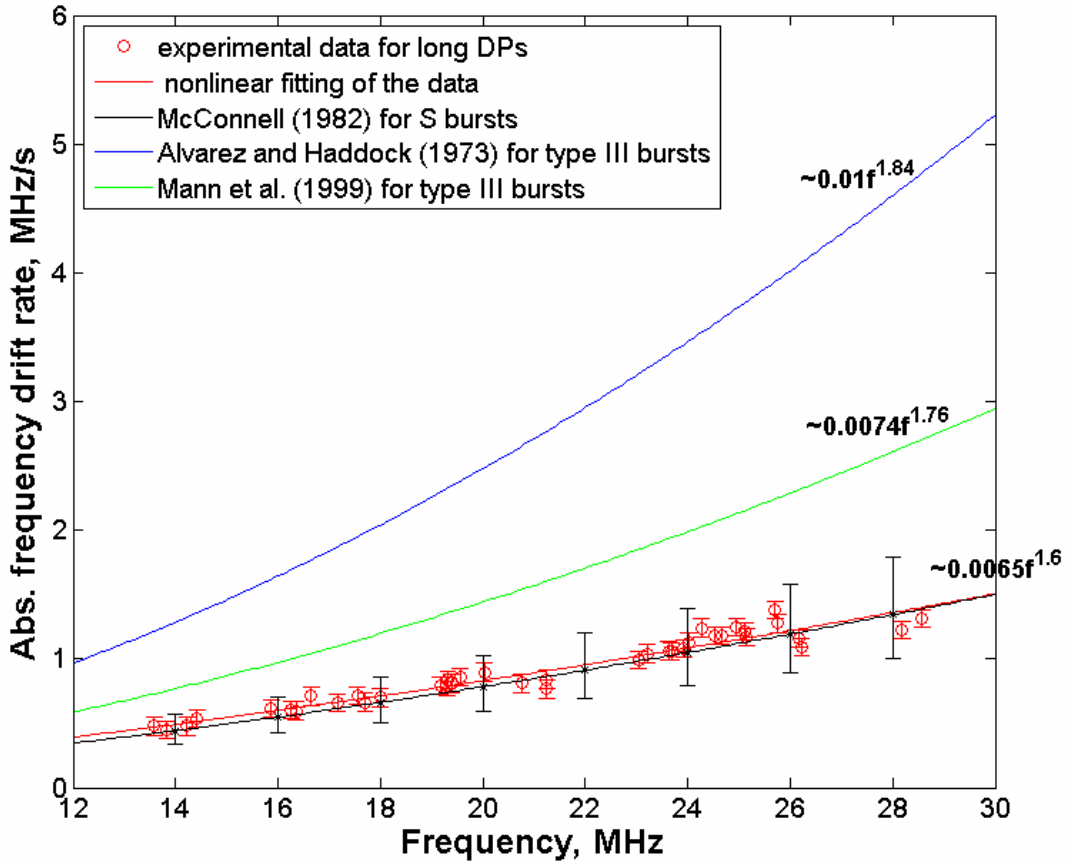

Fig.2. Comparative analysis of the absolute frequency drift rates for long DPs, type III bursts and solar S-bursts in dependence of frequency at decameter wavelengths with the use of data from various references (see them in the end of this report). Each circle corresponds to a single DP for which the frequency drift rate is determined on the central frequency of this chosen long DP.

Results

Based on the above processing procedure, we have analyzed frequency-time properties of the long DPs. The results are presented in Figure 2. The frequency drift rate of long DPs is lower than the rates in the typical type III bursts at decameter wavelengths, but it is similar to the solar S-bursts in the same frequency range of observations according to McConnell [5]. In the case of the long DPs the best fitting of their frequency drift rate satisfies to the equation (here the frequency in MHz and the frequency drift rate in MHz/s)

$$\dot{f}(f) = -0.01 f^{1.47}. \quad (3)$$

Following the study, we have established that formula (1) precisely are suitable for the description of frequency drift rates of the long DPs observed in 10-12 July of 2015. Our comprehensive analysis clearly shows that the functional form of the frequency drift rate of DPs in dependence of frequency is very similar to the case of the type III solar bursts [6,7] , but the model parameters are obtained different. If we consider the value at 20 MHz, then the typical frequency drift rate of type III bursts is expected either -2.48 MHz/s (according to the model [6]) or -1.44 MHz/s (following the model [7]), respectively, whereas the long DPs tend to -0.82 MHz/s.

Acknowledgements

This research was partially supported by Research Grant "Synchronized simultaneous study of radio emission of solar system objects by low-frequency ground- and space-based astronomy" from the National Academy of Sciences of Ukraine.

References

[1] Roberts J.A. Evidence of echoes in the solar corona from a new type of burst // Aust. J. Phys. – 1958. – 11. – P:215-234.
[2] de la Noë J., Møller-Pedersen B. Relationship between drift pair bursts and decametre type III solar radio emission // Astron. Astrophys. – 1971. – 12. – P:371-378.
[3] Ryabov V.B., Vavriv D.M., Zarka P., et al. A low-noise, high-dynamic-range, digital receiver for radio astronomy applications: an efficient solution for observing radio-bursts from Jupiter, the Sun, pulsars, and other astrophysical plasmas below 30 MHz // Astron. Astrophys. – 2010. – 510. – id.A16.
[4] Melnik V.N., Konovalenko A.A., Dorovskyy V.V., et al. Solar drift pair bursts in the decameter range // Solar Phys. – 2005. – 231. – P:143-155.
[5] McConnell D. Spectral characteristics of solar S bursts // Solar Phys. – 1982. – 78. – P:253-269.
[6] Alvarez H., Haddock F.T. Solar wind density model from km-Wave type III bursts // Solar Phys. – 1973. – 29. – P:197-209.
[7] Mann G., Jansen F., MacDowall R.J., Kaiser M.L., Stone R.G. A heliospheric density model and type III radio bursts // Astron. Astrophys. – 1999. – 348. – P:614-620.

The investigations of the interplanetary scintillations at decameter wavelengths: the present state and perspectives

Kalinichenko N.N. [1], *Konovalenko A.A.* [1], *Brazhenko A.I.* [2], *Ivantishin O.L.* [3], *Lytvynenko O.A* [1], *Olyak M.R.* [1], *Bubnov I.N.* [1], *Yerin S.N.* [1]

[1] Institute of Radio Astronomy of NASU, Ukraine;
[2] Gravimetrical observatory of Geophysical institute of NASU, Ukraine;
[3] Institute of physics and mechanics of NASU, Ukraine;
E-mail: kalinich@rian.kharkov.ua

Abstract

The present state of the IPS investigations at decameter wavelengths: radio telescopes, equipment and methods are discussed. We also describe some interesting results devoted to the long term monitoring of the solar wind beyond Earth's orbit, the detection of the large scale disturbances associated with active processes at the Sun and the reconstructions of the solar wind stream structure. Emphasis is placed on perspectives of IPS investigations which are particularly connected with the creation of Giant Ukrainian Radio Telescopes (GURT).

Introduction.

Interplanetary scintillation (IPS) phenomenon is known to arise when the radiation from small size radio source is scattered by density irregularities in the interplanetary plasma, producing a diffraction pattern on the Earth's surface. The motion of the interplanetary irregularities converts the diffraction pattern into temporal intensity fluctuations [1]. Analysis of IPS characteristics (IPS technique) allows the conclusions to be made on the solar wind parameters (speed, density, spectral index of interplanetary turbulence spectrum etc). The efficiency of IPS technique, among others, depends on the observational frequency. High frequencies (higher than 100 MHz) are effective at elongations less than 90 degrees. Low frequencies (lower than 100 MHz) allow us to obtain the solar wind parameters both at small (less than 90 degrees) and large (more than 90 degrees) elongations [2-4]. The last ones correspond to the solar wind beyond Earth's orbit where high frequencies are only slightly scattered by rarefied interplanetary plasma.

URAN Radio Telescope System.

We carry out IPS observations at decameter wavelengths (8 - 32 MHz) with URAN radio telescope system containing 5 radio telescopes including the largest in the world decameter radio telescope UTR-2 [5,6] (fig. 1-3).

Fig.1. Ukrainian decameter radio telescopes for IPS observations on the map.

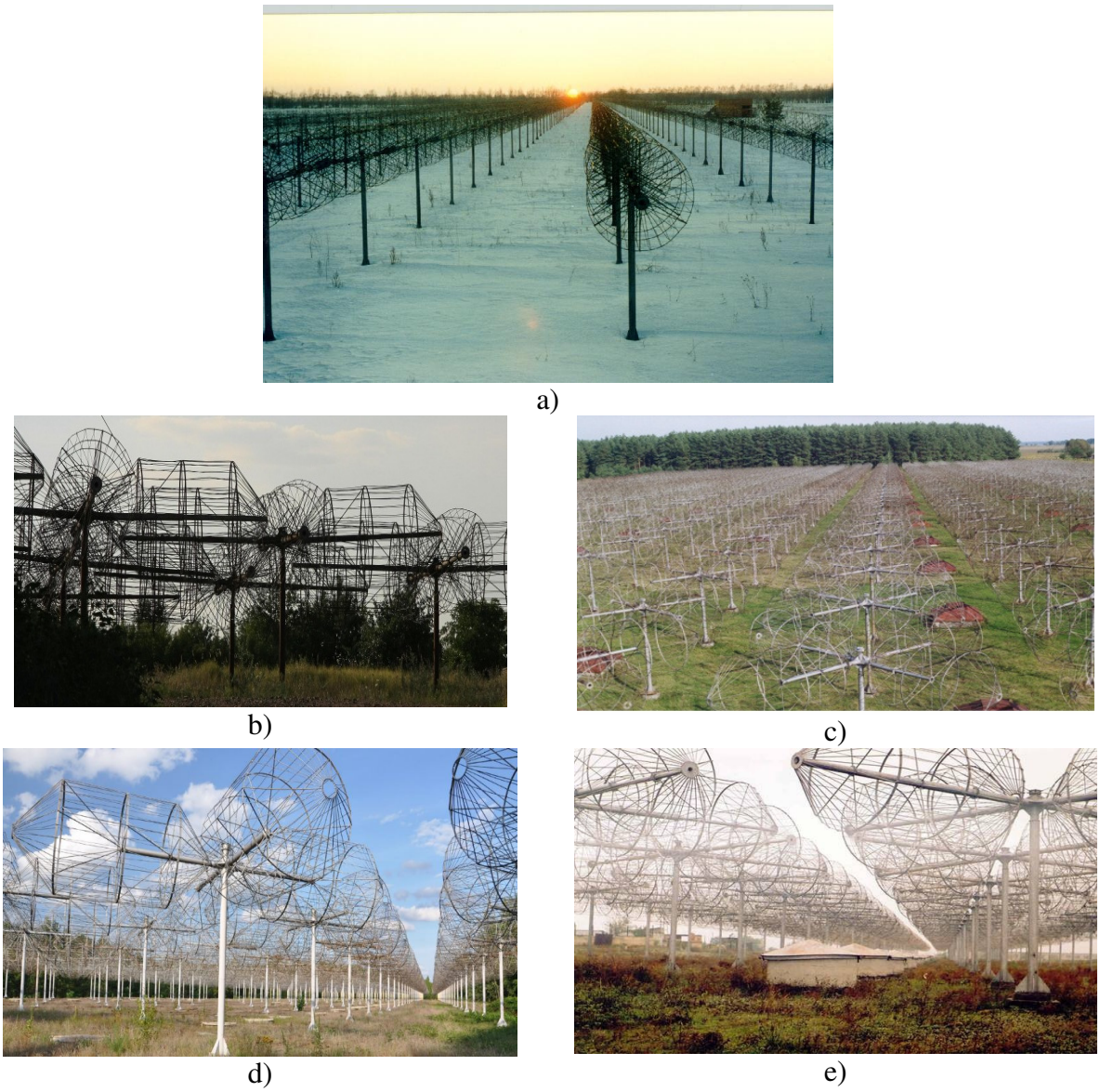

Fig.2. Outward appearances of Ukrainian decameter radio telescopes for interplanetary and ionospheric scintillation observations (a) - UTR-2, b) - URAN-1, c) - URAN-2, d) - URAN-3, e) - URAN-4).

Records are obtained by using digital spectrum analyzers with parameters: instant band of analysis is 33 MHz (sampling frequency is 66 MHz); the number of channels is 8192; the time and frequency resolutions are 0.5 ms and 4 kHz, respectively; the ADC resolution is 16 bit. The use of the high linearity wideband receivers mentioned above and records from several radio telescopes allows us to apply a special technique for selecting data, which are not corrupted by Earth's ionosphere and interferences, and to achieve sensitivity that is close to maximal. In particular such receivers enable us to carry out observations even at daytime in presence of strong interference.

Data Processing.

*Data pr*ocessing consists *in estimation of power spectrum* $P(\nu)$ (1), scintillation index m (2) and the velocity of harmonics of spatial cross-spectrum $V(\Omega)$ (3):

$$P(\nu) = |F(\nu)|^2 / T, \qquad (1)$$

where $F(\nu)$ is Fourier transform of $I(t)$ process, ν is the fluctuation frequency, T is the duration of time series.

$$m = \frac{\sigma_{IPS}}{\overline{I(t)}} = \frac{\sqrt{\sigma^2_{(IPS+n)} - \sigma^2_n}}{\overline{I(t)}} \quad (2)$$

where $\overline{I(t)}$ is the mean intensity of the radio source, σ^2_{IPS}, σ^2_n, $\sigma^2_{(IPS+n)}$ - are the dispersions of the interplanetary scintillations, noise and their sum estimated from the power spectrum.

$$V(\Omega) = \frac{\Omega r}{\Delta\varphi(\Omega)} \quad (3)$$

where $\Delta\varphi(\Omega) = \mathbf{arctan}\frac{\mathbf{Im}W(\Omega)}{\mathbf{Re}W(\Omega)}$ is the phase of the spatial cross-correlation function $W(\Omega)$, $\Omega = 2\pi f$, r - base.

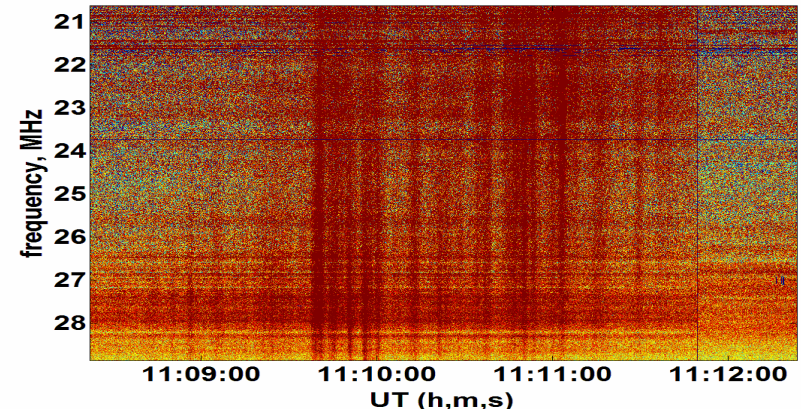

a)

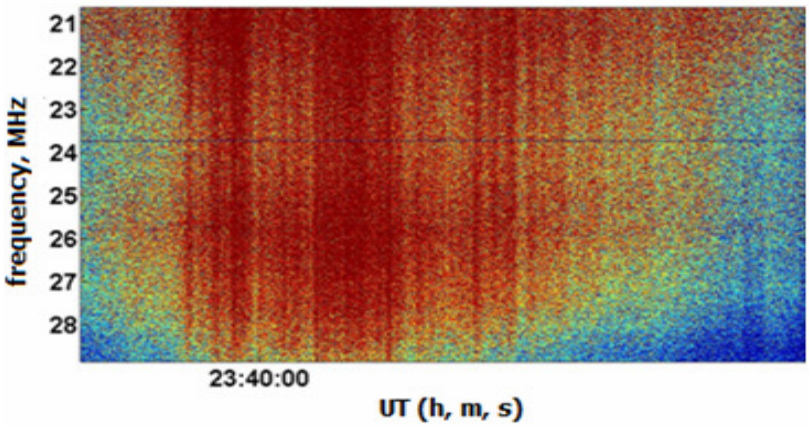

b)

Fig.3. Dynamic spectra of IPS at: a small elongation (a) - 40 degrees and large elongation (b) - 170 degrees. Radio telescope UTR-2. Radio sources: a) - 4C21.53, b) - 3C196.

Solar wind parameters are usually obtained by fitting theoretical characteristics to the observed ones and using multi-flow model of the solar wind. At high frequencies for the calculations of the theoretical characteristics the phase screen model is usually used. However, at the large elongations and at the low frequencies the scattering medium is essentially expanded and the most scattering layer is situated near an observer, so the use of phase screen model is not correct. We use Feynman path-integral technique in our case [2].

Results of Observations.

Stream structure of solar wind.

Analysis of data from spacecrafts near Earth's orbit shows the presence of the solar wind streams with different velocities [7]. Does stream structure remain at distances more than 1 a.u. from the Sun? Fig. 4 answers to this question. Sometimes at least three streams can be seen at large distances from the Sun by IPS observations at large elongations.

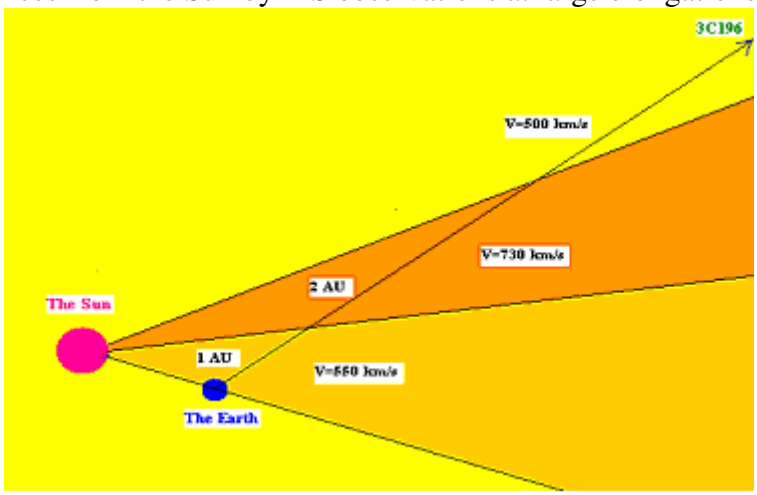

Fig. 4. The stream structure of the solar wind on the line of sight to the radio source 3C196 (October 2006). The data was obtained with UTR-2 and URAN-2 radio telescopes.

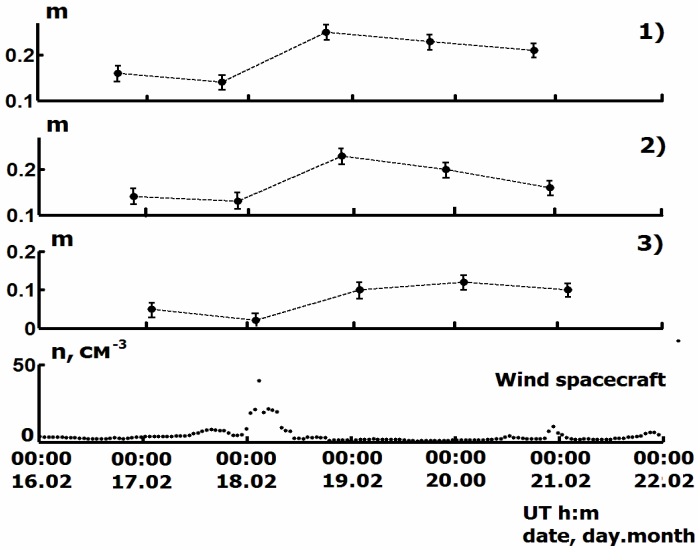

Fig.5. The behavior of the scintillation index during 5 days for observed radio sources (1 - 3C144, 2 - 3C196, 3 - 3C273) and the proton density in the solar wind measured by NASA spacecraft Wind (the bottommost panel of the Figure). Valentine's Day CME.

ICME beyond Earth's orbit.

ICME reveals itself in IPS data at decameter wavelengths as sharp increases of scintillation index and width of power spectrum (fig. 5 and fig 6 correspondingly). Why are ICME observations beyond Earth's orbit important? As ICMEs continue slowing at the distances of several a.u. from the Sun, the investigations of ICME dynamic beyond Earth's orbit will allow us to construct a reliable model of ICME propagation in Heliosphere. Such model for instance makes possible a precise prediction of the arrival time of ICME at the Earth.

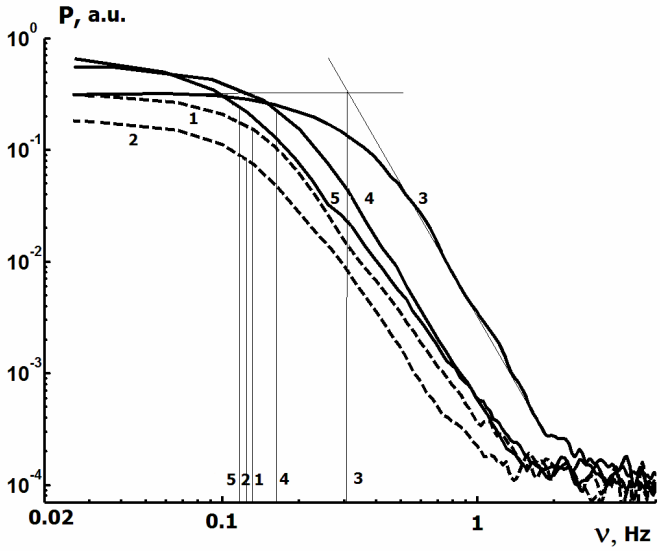

Fig.6. The power spectra for the radio source 3C144: 1 - 16.02.2011, 2 - 17.02.2011, 3 - 18.02.2011, 4 - 19.02.2011, 5 - 20.02.2011. Valentine's Day CME.

Annual statistics of solar wind parameters.

Large enough volume of experimental data allows us to obtain the annual statistic of the solar wind parameters. Compare the solar wind velocity for two years in a declining period of solar activity (fig. 7). It is seen the difference in histograms for two years.

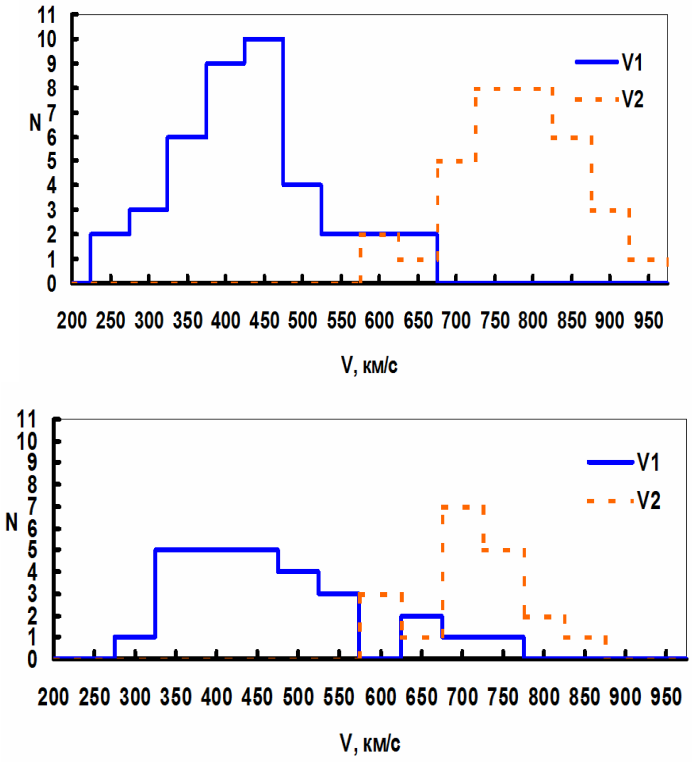

Fig.7. The histograms of the solar wind velocity for two years in a declining period of solar activity. V1 and V2 are the velocities of the slow and high speed streams correspondingly.

Perspectives.

Further progress in IPS investigations at decameter wavelengths we link, among others things, with the creation of Giant Ukrainian Radio Telescopes (GURT) (Frequency range 10 – 80 MHz) in Gracove, Ukraine. The new radio telescope GURT has been built near the radio telescope UTR-2 (fig. 8). It consists of 25-element sub-arrays. It is planed that GURT will include about 100 sub-arrays. At present 3 sub-arrays are fully equipped and 9 sub-arrays are partially equipped. GURT allows us to carry out more effective observations at small elongations (less than or about 70 degrees) in the frequency range 40 to 80 MHz with lower level of interference at day time. Also it enables us to use more effectively our method of separation of interplanetary and ionospheric scintillations.

Fig.8. North-South arm of the radio telescope UTR-2 (foreground) and the radio telescope GURT behind it (white color).

Conclusions

IPS observations at decameter wavelengths allow us to obtain the solar wind parameters, reconstruct the stream structure of the solar wind and to fund and study ICMEs. The new radio telescope GURT (10 – 80 MHz) enables us to rise the efficiency of such investigations especially at small solar elongations (less than 70 – 80 degrees).

References

[1] Hewish, A., Scott, P.F., and Wills, D. Interplanetary Scintillation of Small Diameter Radio Sources // Nature. - 1964. - 203, №4951. - P. 1214-1217.

[2] Falkovich, I.S., Konovalenko A.A., Kalinichenko, N.N., Olyak M.R., Gridin, A.A., Bubnov, I.N., Brazhenko A.I., Lecacheux A., Rucker H. Dispersion Analysis of Interplanetary Scintillations at Decameter Wavelengths: First Results // Radio Physics and Radio Astronomy. 2010. 1, №1 P. 3-9.

[3] Kalinichenko N.N. Scintillations of Radio Source 4C21.53 at Decameter wavelengths and elongations 43o-138o // Radio Physics and Radio Astronomy. -2012. -3, №2. - P. 131-138.

[4] Olyak M.R. Large-scale structure of solar wind and geomagnetic phenomena. // JATF. -2012. - 86. - P. 34-40.

[5] Braude, S.J., Megn, A.V., Sodin, L.G.: 1978, Radio telescope of decameter wave range UTR-2, Antennas, Moscow, P. 28.

[6] Megn, A.V., Sharykin, N.K., Zakharenko, V.V., Bulatsen, V.G. Brazhenko, A.I., Vashishin, R.V. : // Radiofizika i radioastronomia. - 2003. - 8. - P. 345.

[7] Burlaga L.F., Lazarus A.J. Lognormal distribution and spectra of solar wind plasma fluctuations: WIND 1995–1998 // Journal of Geophysical Research: Space Physics. - 2000. - P. 2357–2364.

Proceedings of
Eighth Workshop "Solar Influences on the Magnetosphere, Ionosphere and Atmosphere"
Sunny Beach, Bulgaria, *May 30 - June 3, 2016*

Radio Emission of the Quiet Sun at 20 and 25 MHz According to Interferometer Observations with the UTR-2 Radio Telescope

Shepeliev V.[1] *, Melnik V.*[1] *, Brazhenko A.*[2] *, Dorovskyy V.*[1] *, Poedts S.*[3] *, Rucker H.*[4]

[1] Institute of Radio Astronomy, Kharkiv, Ukraine
[2] Institute of Geophysics, Gravimetrical Observatory, Poltava, Ukraine
[3] Catholic University of Leuven, Leuven, Belgium
[4] Commission for Astronomy, Graz, Austria
E-mail: shep@rian.kharkov.ua

Abstract

We report observations of the solar radio emission at frequencies of 20.0 and 25.0 MHz by radio interferometers with different baselines composed of sections of North-South and East-West arms of the UTR-2 radio telescope. The interferometer measurements were accompanied with wide band observations within 8–33 MHz with the URAN-2 radio telescope. There was only one day when strong sporadic radio emission consisting of type III, type II and type IV bursts have been observed. There was no solar activity in the decameter range on other days of the observational session. A flux density of the quiet Sun in that period is estimated to lie within 1050–1100 Jy and 1480–1570 Jy at 20.0 and 25.0 MHz, correspondingly. An angular size of the quiet Sun in equatorial and polar directions was 55′ and 49′ at 20.0 MHz and 50′ and 42′ at 25.0 MHz. Brightness temperatures of solar corona radio emission was found to be Tb =5.1·105 K and Tb =5.7·105 K at 20.0 and 25.0 MHz, respectively.

Introduction

Radio emission of the quiet Sun was studied in a wide frequency range since the forties of the last century. The measurements were mainly made at mm-, cm-, dm- and m- wavelengths and only rare investigations were performed in the decameter range. The very first observation of the quiet Sun at these low frequencies were made in 1971 with the Arecibo radio telescope at 29.3 and 36.9 MHz [1]. In the late 70s, such studies at the decameter wavelengths were performed with the Clark Lake radio telescope at a set of frequencies [2, 3], and with the UTR-2 at 25.0 MHz [4]. In the 80s, the quiet Sun was observed with Indian GMRT radio telescope at 34.0 MHz [5, 6] and with the Clark Lake radio heliograph [7]. In the years of the last solar minimum of 2008–2009, radio emission of the quiet Sun was observed with the URAN-2 radio telescope [8], and with the UTR-2 radio heliograph in 2010 [9]. These studies have revealed that solar flux density, angular size, and brightness temperature measured during deep minima and those obtained in the years of increasing phase of the solar activity differ significantly, that is the parameters of the quiet Sun are non-stationary. It is of current interest to analyze in what way the diameter of the Sun and its brightness temperature vary during the 11-years cycle and how these parameters are affected by such strong phenomena as CMEs which essentially excite the solar corona.

Here we report the observations of the quite Sun at the decameter wavelengths during the period since 27 May to 2 June 2014 with the UTR-2 and URAN-2 radio telescopes. We have used a set of interferometers formed of the N-S and E-W arms of the UTR-2 to measure flux densities of the Sun and its angular diameter in equatorial and polar directions. The interferometers operated at two frequencies of the range, namely 20.0 and 25.0 MHz, whereas simultaneous observations with the URAN-2 were made with a digital spectrum analyzer with operating band 8–33 MHz. The latter was used to analyze dynamical spectra of the solar emission and to distinguish between thermal and sporadic radio emission.

Instruments and Methods

The present observations were performed with the Ukrainian UTR-2 and URAN-2 radio telescopes operated within 8–33 MHz. The UTR-2 radio telescope, located near Kharkiv, is the world-largest radio astronomical instrument of the decameter range with the maximum effective area about 140 000 m^2. Its T-shaped antenna system is composed of two rectangular arrays with dimensions 1860 × 54 (North-South arm) and 900 × 40 m (East-West one). Half-power width of a primary beam of the radio telescope is about 0.5º at the middle frequency of the band [10]. The URAN-2, located near Poltava, has a rectangular antenna array with an effective area 28 000 m^2. Its dimensions are 238 × 118 m and the half-power beam 3.5°×7° in East-West and North-South directions, respectively [11]. The beam of the radio telescopes is electrically controlled in both directions.

To measure an angular diameter of a radio source with a "single-dish" instrument one can scan a target source with a radio telescope beam. In this method, the source size is calculated from the width of the scan curve recorded, which is a convolution of antenna pattern and source brightness distribution. If the source size is much wider than the beam width, this curve is a profile of the source brightness distribution and the width of the profile is defined by the source angular diameter. In the opposite case, the shape of the scan represents the antenna pattern. If the source size and the beam width have comparable values, as in the case of the Sun and UTR-2, the antenna pattern must be subtracted from the scan curve recorded and the shapes of the beam and the source brightness distribution must be kept in mind when the source angular diameter is calculated. Besides, high level of side lobes characteristic of rectangular arrays used at low frequencies, distortions, and interferences that are typical for the decameter range essentially complicate such measurements based on the analysis of the scan curve shape.

An alternative way of angular size determination is interferometer observations. In this method, the shape of the source and its size are computed by analyzing the visibility dependence on interferometer baselines [12]. In the simplest case, only amplitude of visibilities measured can be used. The UTR-2 arms are composed of identical simultaneously controlled sections that have independent signal outputs. The N-S arm consists of eight such parts and the E-W one has four sections. The beam width of each section is 4º × 15º, which is much wider than the Sun diameter, so the antenna pattern side lobes do not affect the observations. Distances between the sections are equal to 225 m that allows forming out three interferometers of the sections of the E-W arm with baselines 225, 450, and 675 m. The eight sections of the N-S antenna form seven different baselines. Assuming a Gaussian shape for the solar brightness distribution at decameter wavelengths the normalized visibility γ for the interferometer with a baseline L is defined by the formula

$$\gamma = \exp\left[-\left(\frac{\pi\theta L}{2\lambda\sqrt{\ln 2}}\right)^2\right], \qquad (1)$$

where θ is the half-power diameter of the source, λ is the wavelength of observations. Dependences of the normalized visibility functions versus the interferometer baseline are shown in fig.1 to demonstrate ability of the interferometers composed of UTR-2 sections to determine a source size. The dependences are calculated according to Equation (1) at frequency 25.0 MHz for different width of Gaussian. Open squares stand for baselines of the E-W arm of the UTR-2, while triangles mark projections of the N-S baselines onto the plane of the source being at the Sun declination in the present observations. One can see that interferometers with the baselines 225 to 675 m are suitable to derive the quiet Sun diameter which is of the order of one degree according to observations in the decameter wavelength range listed above. The longer baselines of N-S antenna can be effective for measurements of the sizes of solar bursts that have smaller dimensions.

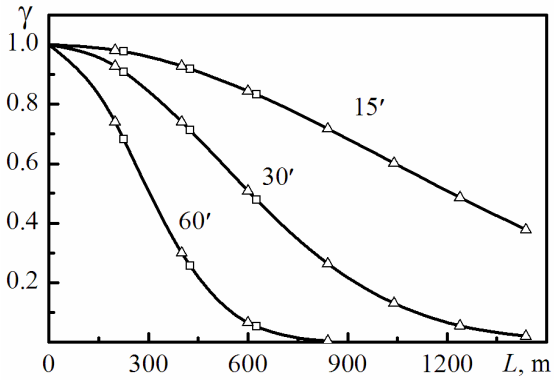

Fig.1. Dependence of visibility function for a Gaussian source with different width versus baseline of interferometer

Observations and Results

The observations of the Sun with the UTR-2 and URAN-2 radio telescopes were made since 27 May to 2 June 2014. In the observations with the UTR-2 we applied an eight-channel digital receiver used for investigations with Ukrainian interferometer network URAN. It allows recording output signals of four antenna sections with bandwidth of 250 kHz at frequencies of 20.0 and 25.0 MHz simultaneously. Synchronous observations with URAN-2 were carried out in the full frequency range of the radio telescope within 8–33 MHz using wideband digital spectrum analyzer with time-frequency resolution of 4 kHz × 100 ms and dynamic range of 90 dB.

Analysis of the wide band data of the URAN-2 showed no significant solar activity during observational session except for May 29, when CME occurred. It was accompanied by groups of type III bursts, type II burst, and type IV burst, which were observed by the UTR-2 and URAN-2 radio telescopes. On other days of the observational session the activity of the Sun was low, only weak infrequent type III bursts were recorded. This opens an opportunity to study the radio emission of the quiet Sun before and after CME.

Interferometer observations with the UTR-2 were carried out by 10-minute scans at hour angles of ±2 hours from a solar culmination. After recording of two such scans, the antenna beam was switched to the position of the radio source 3C144 (Taurus A) for the next 10 min. This powerful radio source, whose flux density is well known and equals 3000 Jy at 25 MHz [13], was used as a calibrator. In the period of the observations, the Sun was situated at the same declination as the calibrator with a distance of one hour in right ascension between them. This allows determining gains of the antenna arrays in solar direction and avoiding confusion.

The average flux of the quiet Sun was determined in the scans not corrupted by interferences and then averaged per each day of observations. Fig.2 shows that the fluxes before and after CME were practically the same.

The measured values are comparable to the fluxes obtained with the Clark Lake radio telescope [3] and significantly lower than those in observations with the Arecibo [1] and essentially higher than values recorded by the UTR-2 [4] and URAN-2 [8, 9] radio telescopes. In the last case, the observations were made at minimum of the solar activity, so it seems explainable.

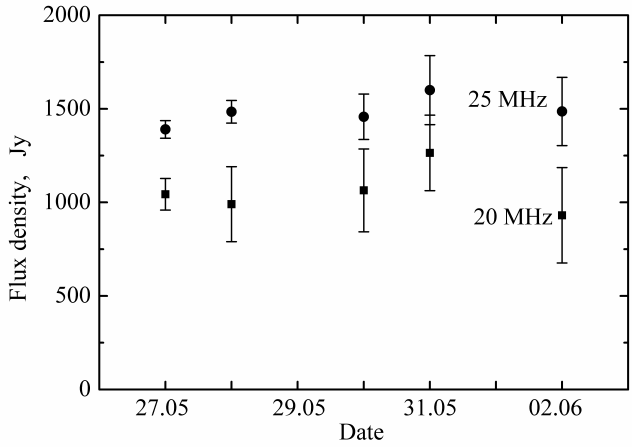

Fig.2. Flux density of the quiet Sun measured with the UTR-2 at 20 and 25 MHz since May 27 to June 2, 2014

In the period since May 27 to 30 we used interferometer composed of E-W sections while since May 31 to June 2 the observations were made with N-S antenna of the UTR-2. So the diameter of the radio quiet Sun in the equatorial and polar directions was measured at different time consecutively. Average visibilities at each baseline were derived from the scans selected in the vicinity of the solar culmination which were not corrupted noticeably by the interferences. These values did not change significantly from day to day, thus the average visibilities for May 27, 28, 30 (E-W direction) and 31 May, 2 June (N-S direction) have been determined. Assuming Gaussian distributions of the quiet Sun's corona brightness dependences calculated according to Equation (1) with varied θ were fitted to the observational data using the least squares method. An example of the experimental points jointly with the calculated curves is shown in fig.3.

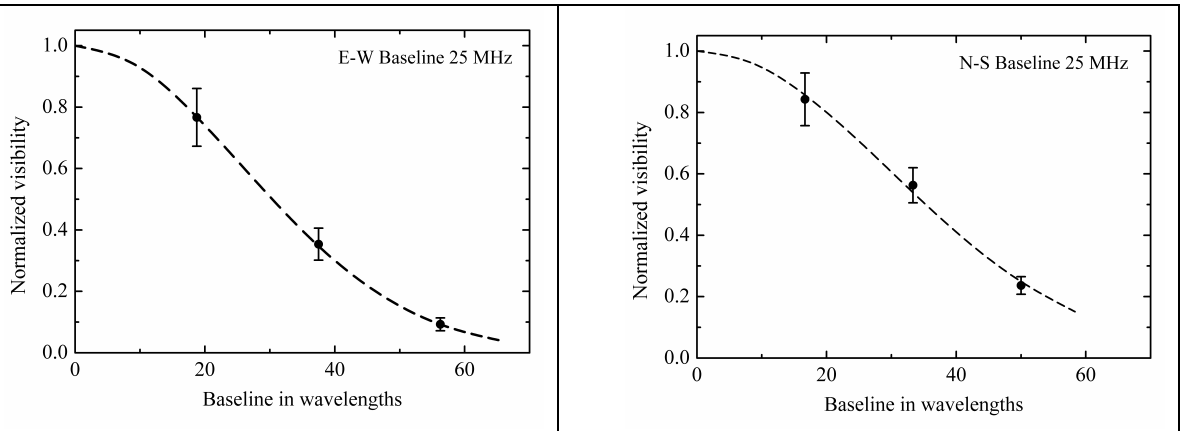

a) b)

Fig.3. Visibility functions of the quiet Sun taken at 25 MHz with the interferometers oriented in E-W (27, 28 and 30 May) (a) and N-S (31 May, 2 June) (b) directions

The angular diameters of the quiet Sun derived from the fitting procedure are summarized in tab.1 together with the flux densities measured. Under assumption that the quiet Sun shape did not change considerably during the week of our observations, the compression factor of the ellipse (polar to equatorial size ratio) was equal to 0.89 and 0.84 at 20.0 and 25.0 MHz, respectively. These values are close to those obtained by van de Hulst [14].

Tab.1. Parameters of the quiet Sun at 20.0 and 25.0 MHz according to observations on May 27 – June 2, 2014.

	E-W direction		N-S direction		
Frequency, MHz	Size, arcmin	Flux, Jy	Size, arcmin	Flux, Jy	Brightness temperature, *K*
20	55±4	1050±150	49±3	1100±230	$5.1 \cdot 10^5$
25	50±3	1480±130	42±2	1570±190	$5.7 \cdot 10^5$

Using the average fluxes and angular sizes obtained in the observations we calculated brightness temperatures of the quiet Sun according to Equation [1]

$$T_b = 5.5 \cdot 10^{29} \frac{\lambda^2 S}{\theta_E \theta_N}, \quad (2)$$

where S is the flux (in $Wm^{-2}Hz^{-1}$), θ_E, θ_N are diameters (in arcmin) in equatorial and polar directions, and λ is the wavelength (in m). The values obtained are listed in tab.1, too. These values, as well as those derived by other authors, are noticeably lower than the temperature of a coronal plasma, which usually is supposed to be equal to $T_b=10^6$K. Such difference can be explained by scattering of electromagnetic waves on inhomogeneities of the coronal plasma [1, 4, 6, 7].

Conclusions

The short baseline interferometers composed of the UTR-2 radio telescope parts have been successfully employed for measurements of the quiet Sun parameters at the decameter wavelengths. The first observations have shown that:

1. The angular diameters and flux densities of the quiet Sun before and after CME was practically the same.
2. Gaussian brightness distribution of the quiet Sun emission is a good approximation at the decameter wavelengths.
3. The shape of the solar corona in the decameter range is elliptical with the compression factor about 0.85-0.9.
4. The brightness temperatures of the quiet Sun was Tb=5.1·105K and Tb=5.7·105K at 20.0 and 25.0 MHz, respectively, and they are lower than the temperature of the coronal plasma.

It is of current interest to observe regularly the quiet Sun in the decameter range to determine in what way the shape, dimensions, and brightness temperature of the solar corona vary during the 11-years cycle and how they are affected by strong phenomena like CMEs.

Acknowledgements

The work was partially financed in the frame of FP7 project SOLSPANET (FP7-PEOPLE-2010-IRSES-269299).

References

[1] Aubier M., Leblanc Y., and Boischot A. Observations of the Quiet Sun at Decameter Wavelengths. Effects of Scattering on the Brightness Distribution // Astron. Astrophys. – 1971 – 12. – P. 435.
[2] Kundu M. R., Gergely T. E., and Erickson W. C. Observations of the Quiet Sun at Meter and Decameter Wavelengths. // Sol. Phys. – 1977. –53. – P. 489.
[3] Erickson W. C., Gergely T. E., Kundu M. R., and Mahoney M. J. Determination of the Decameter Wavelength Spectrum of the Quiet Sun. // Sol. Phys. – 1977. – 54. – P. 57.
[4] Abranin E. P., Bazelian, L. L., Goncharov, N. Iu., Zaitsev, V. V., Zinichev, V. A., Rapoport, V. O., and Tsybko, Ia. G. Positions of solar storm burst sources by observations with a heliograph based on the UTR–2 antenna at 25 MHz. // Solar Phys. – 1980. – 66. – P. 393.
[5] Sastry Ch. V. Observations of the continuum radio emission from the undisturbed Sun at a wavelength of 8.7 meters. // Solar Phys. –1994. – 150. – P. 285
[6] Subramanian K. R. Brightness temperature and size of the quiet Sun at 34.5 MHz. // A&A –2004. – 426. – P. 329.
[7] Thejappa G. and Kundu, M. R. Unusually low coronal radio emission at the solar minimum. // Solar Phys. – 1992. – 140. – P. 19.
[8] Brazhenko A.I., Koval A.A., Konovalenko A.A., Stanislavsky A.A., et al. Peculiarity of Continuum Emission from the Upper Solar Corona at Decameter Wavelengths. // Radio Physics and Radio Astronomy. – 2012, – 3. – P. 187.
[9] Stanislavsky A.A., Koval A.A., and Konovalenko A.A. Low–frequency heliographic observations of the quiet Sun corona. // Astron. Nachr. – 2013. – 334. – P. 1086.
[10] Braude S. Ia., Megn A. V., Riabov B. P., Sharykin N. K., and Zhuk I. N.:, Decametric survey of discrete sources in the Northern sky. I – The UTR–2 radio telescope: Experimental techniques and data processing. Astrophysics and Space Science. – 1978. – 54. – P. 3.
[11] Мень А.В., Шарыкин Н.К., Захаренко В.В., Булацен В.Г., Браженко А.И., Ващишин Р.В. Радиотелескоп декаметрового диапазона длин волн УРАН–2 // Радиофизика и радиоастрономия. – 2003. – Т. 8, № 4. – С. 345–357.
[12] Thompson J.M. Moran G.W. and Swenson Jr, A.R.: 2001, Interferometry and Synthesis in Radio Astronomy (Second Edition) John Wiley & Sons, Inc.
[13] Bobeiko A. L., Bovkoon V. P., Braude S. Ia., Megn A. V., and Sergienko Iu. Iu. Measurements of radio emission from the compact source in the Crab nebula with the Uran–1 interferometer at 16.7, 20 and 25 MHz. // Astrophysics and Space Science. – 1979. – 66. – P. 211.
[14] van de Hulst H. C. Zodiacal Light in the Solar Corona // Astrophysical Journal. – 1947. – 105. – P. 471.

Proceedings of
Eighth Workshop "Solar Influences on the Magnetosphere, Ionosphere and Atmosphere"
Sunny Beach, Bulgaria, *May 30 - June 3, 2016*

Interferometer observations of solar type III bursts by the radio telescope UTR-2

Melnik V. [1], Shepelev V. [1], Brazhenko A. [2], Dorovskyy V. [1], Rucker H. [3], Poedts S. [4]

[1] Institute of Radio Astronomy, Kharkiv, Ukraine
[2] Institute of Geophysics, Gravimetrical Observatory, Poltava, Ukraine
[3] Commission for Astronomy, Graz, Austria
[4] Catholic University of Leuven, Leuven, Belgium
E-mail: melnik@rian.kharkov.ua

Abstract

Results of solar radio emission observations by the radio telescopes UTR-2 (Kharkiv, Ukraine) and URAN-2 (Poltava, Ukraine) in May-June 2014 are discussed. Observations by the radio telescope UTR-2 were carried out in the interferometer mode using West-East arm of the UTR-2 with bases 225 m, 450 m and 675 m on May 29 and North-South arm with bases 208 m, 416 m, 624 m, 885 m, 1301m and 1509 m on June 2 at frequencies 20 MHz and 25 MHz. On May 29 some powerful simple type III bursts and groups of type III bursts were observed against type IV burst. There were only single weak type III bursts on June 2. Analysis of visibility functions of radio emission sources at these frequencies was allowed to find spatial sizes of bursts sources, which changed mainly from 20` to 22` at 25 MHz and from 24` to 27` at 20 MHz. Also sources distances at these frequencies were obtained. Radio emissions at frequencies 20 MHz and 25 MHz escaped at distances $2.9R_S$ and $2.6R_S$, respectively, in most cases. At these distances radio emissions at frequencies 10 MHz and 12.5 MHz are generated in the Newkirk corona so the observational radio emissions are the second harmonics. This fact is confirmed by the low polarizations of discussed type III bursts. Brightness temperatures of these bursts were in the range from $2.1\text{x}10^9 K$ to $4.4\text{x}10^{10} K$ for bursts on May 29 and only about $10^8 K$ for the burst observed on June 2.

Introduction

In 60^{th}-80^{th} observations for definition of sizes of different solar burst sources in the decameter range from 12.5 MHz to 40 MHz were conducted ([1] - [8]). Heliographic and interferometer methods were used for that. According to some authors analyzed type III bursts had core-halo structures. But others did not find such structures. Sizes of cores, if they were detected, were about 10` and sizes of halos were up to 40` at different frequencies. The least sizes, 15`, were revealed at 40 MHz and the largest ones, not more than 40`, at 12.5 MHz. At intermediate frequencies the sizes were from 15` to 30` mainly. In some of these observations the distances of radiation places were defined. They were changed in the range $1.75R_S$-$2.5R_S$ at frequency 40 MHz and in the range $1.55R_S$-$2.9R_S$ at frequencies 25 MHz, 26.3 MHz and 30 MHz. It was registered that radio emissions of discussed type III bursts occurred predominantly at the second harmonic of the local plasma frequency.

In this report the results of the observations of type III bursts on May 29 and June 2, 2014 by radio telescopes UTR-2 and URAN-2 are discussed. The radio telescope UTR-2 worked in the interferometer mode at frequencies 20 MHz and 25 MHz and the radio telescope URAN-2 observed the solar radio emission in the standard spectrographic mode in the frequency band 8-32 MHz. Sizes of type III bursts sources as well as their distances from the center of the Sun were found.

Results and Discussion

The bases 225 m, 450 m and 675 m between sections of West-East arm on May 29 and the bases 208 m, 416 m, 624 m, 885 m, 1301 m and 1509 m between sections of North-South arm on June 2 were used in the interferometer mode of observations by the radio telescope

UTR-2. The single type III bursts and their groups were observed against type IV burst this day. For analysis 8 most powerful type III bursts at 9:41, 10:07, 10:08, 10:14, 10:15, 10:16, 11:13 and 11:14 were chosen. On June 2 there was practically the quiet Sun in the frequency band 8-32 MHz with some single weak type III bursts. We obtained sizes and distances of type III burst source occurred at 6:59.

The dynamic spectrum of solar radio emission in the frequency range 8-32 MHz from 9:07 to 12:07 UT on May 29, 2014 is shown in the Figure 1. This time interval corresponds to that when the radio telescope UTR-2 worked in the interferometer mode this day.

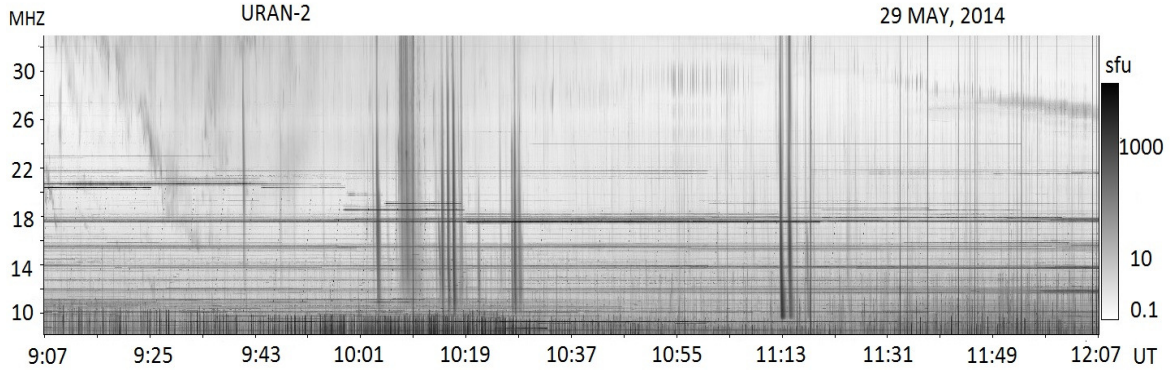

Figure 1. The dynamic spectrum of solar radio emission from 9:07 to 12:07 according to URAN-2 observations.

The main parameters of discussed type III bursts are represented in the Table. All type III bursts registered on May 29 had fluxes from $10^2 s.f.u.$ to $10^3 s.f.u.$ Observed on June 2 type III burst was essentially weaker.

The frequency drift rates of discussed bursts between 20 and 25 MHz are not so much as for standard decameter type III bursts [9], only about 1 *MHz/s*. The burst durations at frequencies 20 *MHz* and 25 *MHz* are in the range 11-17s and only the burst at 9:41 UT is shorter. The polarizations of all analyzed type III bursts are not higher than 11%. It says that these bursts are generated at the second harmonic of the local plasma frequency. Sizes of type III sources were derived by writing in the visibility function $\gamma = \exp[-(\frac{\pi\theta L}{2\sqrt{\ln 2}\lambda})^2]$ (θ is the angle size, λ is the wave length, at which observations were carried out, and L is the interferometer base) [10] in experimental data (Figure 2). Derived sizes are presented in the Table. In most cases type III source sizes are in the ranges 24`-27` and 20`-22` at frequencies 20 MHz and 25 MHz respectively. The sizes of two bursts at 10:07 and 10:08 at 25 MHz are visibly larger than for others. We connect this feature with high level of background radio emission that increases effective sizes of bursts. At the same time the level of radio emission at 20 MHz is not so high and as consequence the effective sizes of bursts at this frequency do not differ so greatly. The sizes of type III burst at 6:59 at both 20 MHz and 25 MHz are larger in comparison with those of type III bursts observed on May 29. Notice that in the last case type III electrons moved in equatorial plane and measured sizes in West-East direction are prolonged sizes of electron beams. At the same time measured sizes of type III burst source on June 2 in North-South direction are transverse sizes. So we can conclude that transverse sizes are larger of prolonged sizes of type III bursts at frequencies 20 and 25 MHz. May be it is the common property but to be sure it is necessary to increase statistics of measured type III sizes.

Table. Parameters of type III bursts observed on May 29 and June 2, 2014.

time, UT	frequency, MHz	flux, s.f.u.	duration, s	drift rate, MHz/s	polarization, %	size, `	Velocity, c	distance, `
9:41	20	170	11	-1.2	0	16	0.21	55
	25	170	7		-11	14	0.29	50
10:07	20	255	14.4	-0.9	-4	26	0.26	49
	25	230	13		-6	29	0.33	39
10:08	20	316	17.5	-1	-1	27	0.23	49
	25	270	14		-6	28	0.29	39
10:14	20	600	14.5	-2.5	-5	27	0.27	47
	25	120	12		-6	22	0.27	41.5
10:15	20	1150	12.3	-1.6	-6	25	0.3	45.5
	25	500	11.3		-9	22	0.28	43
10:16	20	2600	16.7	-2.5	-7	27	0.24	44.5
	25	1000	13		-9	22	0.25	41.5
11:13	20	2090	12.5	-0.9	-5	24	0.28	47
	25	710	10.6		0	20	0.28	42.5
11:14	20	790	16	-0.9	-5	23	0.21	46
	25	260	13.5		0	21	0.23	41.5
6:59	20	18	14	-2	0	29		---
	25	6	12		0	27		43

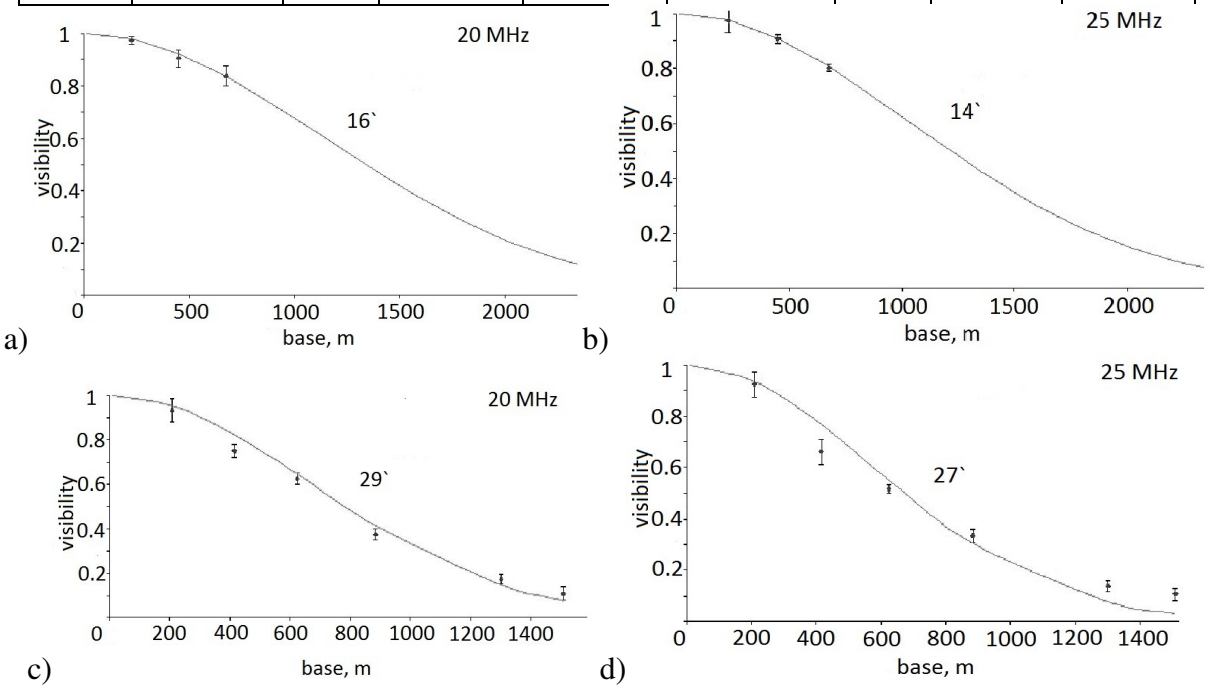

Figure 2. Visibility functions for type III bursts observed at 9:41 on May 29 (a,b) and at 6:59 on June 2 at frequencies 20 MHz and 25 MHz.

The ratio of prolonged sizes to duration of type III bursts at some frequency gives the velocity of electron beam responsible for this burst. We see that these velocities at both frequencies are in the range 0.2c-0.3c. These velocities are in good agreement of generally accepted theory of type III bursts.

Supposing that transverse sizes are not differed significantly from the prolonged sizes the brightness temperatures of type III bursts were derived. They changed from $2.1 \times 10^9 K$ to $4.4 \times 10^{10} K$ for type III bursts observed on May 29. Such brightness temperatures are characteristic for the induced processes of transformation of Langmuir waves to transverse waves [11]. Type III bursts observed on June 2 had brightness temperatures smaller than

$10^9 K$ at both frequencies 20 and 25 MHz. It means that this burst was generated in spontaneous processes [11].

Distances of type III sources was defined by the phase differences of signals coming to sections of interferometer according the equation $\sin\Delta\theta = \frac{\Delta\varphi\lambda}{2\pi L}$ (where Δθ is the angle distance, Δφ is the phase difference, λ is the wavelength and L is the interferometer base) [10]. Sources of type III bursts at 20 MHz and 25 MHz were situated from 45` to 49` and from 39` to 43` from the solar centre respectively. In supposition that electron beams propagated in the Newkirk corona we found that at these distances local plasma frequencies were two times smaller than the frequency of type III radio emissions. It says in favor of radio emission of these bursts at the second harmonic. A little higher altitudes for type III burst at 9:41 can be indicate that corresponding electrons propagated through the corona with temperature higher than $1.4 \text{x} 10^6 K$ (see, for example, [12]).

Conclusions

The first interferometer observations of the solar radio emission by the radio telescope UTR-2 showed that the sizes of the radio telescope and its construction are very good for the definition of type III sources sizes and their distances. Measured type III sources had practically Gaussian distributions, which were defined by the only size i. e. sources did not show core-halo structure. Of course this statement should be confirmed on the more statistical sampling. At both frequencies 20 MHz and 25 MHz type III sources had prolonged sizes between 20` and 30`. The velocities of electron beams responsible for type III bursts had values 0.2c-0.3c mainly that agreed with type III bursts theory. Brightness temperatures of type III bursts with fluxes $10^2 - 10^3 s.f.u.$ are in the range $10^9 K - 5 \cdot 10^{10} K$ that corresponds to the induced processes of type III bursts generation. The discussed bursts occurred in the plate plane and in this case distances from the Sun corresponded to the generation of the second harmonic of the local plasma frequency. This fact is supported by low measured polarizations of discussed type III bursts.

References

[1] Weiss A.A., Sheridan K.V. The sizes of the sources of solar radio bursts at 40 and 60 Mc/s // Journal of the Physical Society of Japan.- 1962. – 17(2). – P:223-226.
[2] Erickson W.C. High-resolution studies of type III solar radio emission at 11.4-meter wavelength // JGR, , 68(10). P: 3169-3179.
[3] Malitson H.H., Erickson W.C. Observations of type III and type IV solar radio bursts at 26.3 Mc/s // Ap.J. – 1966. – 144. – P: 337- 351.
[4] Gergely T.E., Kundu M.R. Decameter storm radiation, II. Solar Physics. – 1975. – 41. – P: 163-188.
[5] Abranin E.P., Bazelyan L.L., et.al. Angular sizes of sources of solar radio bursts in the decametre range // Soviet Astronomy. – 1976. – 19(5). – P: 993-998.
[6] Chen S.-L.H., Shawhan S.D. Structure and evolution of solar radio bursts at 26.4 MHz // Solar Physics. – 1978. – 57. – P: 205-227.
[7] Dulk G.A., Suzuki S. The Position and Polarization of Type III bursts // Astronomy & Astrophysics. – 1980. – 88. – P: 203-217.
[8] Abranin E.P., Bazelyan L.L., et.al. Positions of solar storm burst sources by observations with a heliograph based on the UTR-2 antenna at 25 MHz // Solar Physics. – 1980. – 66. – P: 393-409.
[9] Melnik V.N., Konovalenko A.A., et.al.. Solar sporadic radio emission in the decametre waveband // Astronomical and Astrophysical Transactions. – 2005. – 24(5). – P:391-401.
[10] Thompson A.R., Moran J.M., Swenson G.W. Interferometry and Synthesis in Radio Astronomy (Second Edition) Wiley, New York. - 2001. – P: 692.
[11] Melnik V.N., Kontar, E.P. Plasma Radio Emission of Beam-Plasma Structures in the Solar Corona // Solar Physics. – 2003. – 215(2). – P: 335-341.
[12] Mann G., Jansen F., MacDowall R. J., Kaiser M. L., Stone R. G. A heliospheric density model and type III radio bursts // Astronomy and Astrophysics. – 1999. – 348. – P: 614-620.

Proceedings of
Eighth Workshop "Solar Influences on the Magnetosphere, Ionosphere and Atmosphere"
Sunny Beach, Bulgaria, *May 30 - June 3, 2016*

The online catalog of Wind/EPACT proton events

Miteva R.[1], Samwel S. W.[2], Costa-Duarte M. V. [3], Danov D.[1]

[1] Space Research and Technology Institute, Bulgarian Academy of Sciences, Sofia, Bulgaria
[2] National Research Institute of Astronomy and Geophysics, Cairo, Egypt
[3] Institute of Astronomy, Geophysics and Atmospheric Sciences, U. of São Paulo, Brazil
E-mail: rmiteva@space.bas.bg

Abstract

We present the newly compiled solar energetic particle catalog based on data from the Wind/EPACT instrument. The focus of this report is the online contents of the catalog's first version. We summarize the procedure employed to identify and analyze the proton events and their solar origin, which constitute the main ingredients of the online catalog. Planned future updates and improvements are also discussed.

Introduction

A solar energetic particle (SEP) is a generic term used to describe an elevated flux of non-thermal electrons, protons and ions observed in situ [1]. The particle profiles show velocity dispersion and follow in time eruptive phenomena that occurred on the Sun thus supporting the solar origin of the phenomena. Compared to all species, the solar protons are more frequently discussed and finally considered as the SEP events. Occasionally, an additional component in the particle profile can be identified, which is the contribution of accelerated articles in the interplanetary (IP) space due to shocks, co-rotating or/and streaming interaction regions, and not due to the primary acceleration process close to the Sun.

Irrelevant on their exact acceleration driver (flares and coronal mass ejections, CMEs) and mechanism, high energy protons and electrons can be harmful for satellite equipment and can expose humans to radiation, more severely during space travel and less during aircraft flights on polar orbits. Nowadays, SEPs are recognized as one of the major space weather agents [2].

The SEP data is eventually stored in databases and occasionally organized in catalogs. One such proton catalog is based on GOES data (http://umbra.nascom.nasa.gov/SEP/) and reports only events with proton intensity above a constant threshold level. Due to the long time coverage of this catalog (since 1976 to present) it is often used for academic research.

Recently, other proton catalogs based on IMP-8, SOHO and GOES proton data were released, namely Cane et al. proton list [3], SEPServer event list (http://server.sepserver.eu/index.php) [4] and the SEPEM reference proton list (http://dev.sepem.oma.be/help/event_ref.html). In contrast to the proton lists, a comprehensive electron event catalog is still lacking, since the only available electron list [5] is compiled for events with specific intensity profiles.

A comprehensive SEP catalog should provide information for the particle event (onset time, peak time, peak particle intensity, fluence, energy range, etc.), as well as the SEP solar origin (flare and CME characteristics). Usually, SEP catalogs are compiled manually after the actual observations were made. However, automatically produced flare and CME lists are already available.

In order to complement the GOES and SOHO proton catalogs and extend the event statistics, we compiled a comprehensive proton event list based on data from the Wind satellite [6]. This proton database is explored for the first time using visual and numerical methods. All proton events above the pre-event background level (i.e., no threshold applied) were identified and organized in a list. The aim of the present report is to describe the online version of this new proton catalog.

Data and Methods

For this catalog we use proton data from the Energetic Particle Acceleration, Composition and Transport (EPACT) instrument [6] aboard the Wind satellite during the time period 1996–2015. We used omni-directional data with time resolution of 92 seconds and in two energy channels (low: 19–28 MeV and high: 28–72 MeV), provided by the CDAWeb database (http://cdaweb.gsfc.nasa.gov).

First, using the web interface, we plotted the proton intensity over time period of several days for visual identification of the proton enhancements. When such an increase was visually confirmed, we collected and then analyzed the proton data using a routine, prepared by us under Python (https://www.python.org/) for the identification of: pre-event averaged intensity level (e.g., background level); onset time (defined as the time when the proton flux reaches 3 standard deviations (sigma) above the background level); peak intensity (the maximum value of the proton intensity identified in a specific, pre-selected time interval, and reported after subtraction of the background intensity level) and peak time (defined as the time when the intensity reaches its peak). In order to identify time and intensity markers, the proton data was initially averaged over 5 data points (denoted with blue color on all overview plots). The background and peak levels are identified based on time intervals manually selected by the observer during the data analysis.

An important part of the analysis is the correct separation of the locally accelerated proton component due to shock waves close to Earth from the SEP event. We excluded the shock-component by requiring the routine to search for the peak in a time interval chosen to precede the shock signature if present. The shock-signatures, which represent an additional increase on a (declining) SEP profile, can be easily identified by a visual inspection. We also used information about the shock arrival times at Earth from the Heliospheric Shock Database (http://www.ipshocks.fi/).

Example plots of the proton intensity–time profile in the low and high energy channels are given in Figure 1. The onsets and peaks are marked by different symbols in all overview plots. There are more than 350 proton events in the low energy and more than 300 events in the high energy channel which are listed in the online catalog.

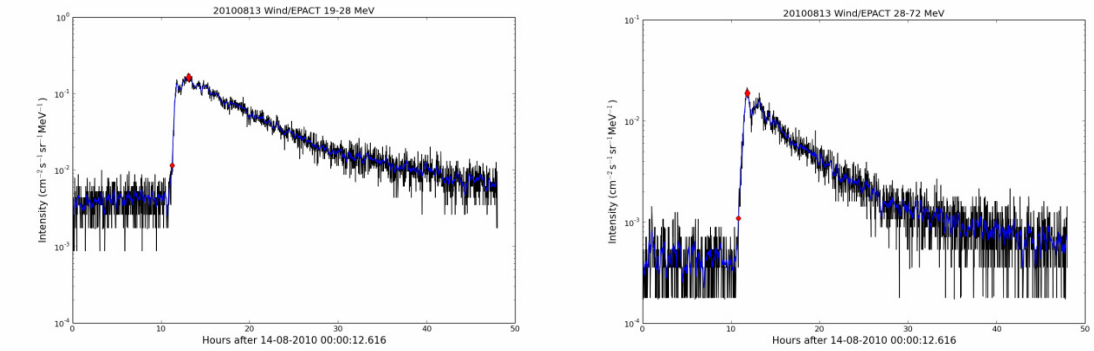

Fig.1. Example intensity–time plots in the low (19–28 MeV) and high (28–72 MeV) energy channel of Wind/EPACT instrument.

Each SEP event is related to activity phenomena observed at the Sun, regarded as the SEP origin. The well-known agents giving rise to accelerated particles are the solar flares and CMEs. We used timing and location criteria to relate each SEP event to its most probable solar driver and often we could identify a pair of flare and CME. The reason when a flare could not be identified, in the majority of cases, was that a flare has occurred behind the solar

limb, as evidenced by occulted radio emission signatures. Alternatively, no association of SEP-related CMEs was primarily due to SOHO data gaps.

The parameters of solar flares are collected from the GOES soft X-ray (SXR) instrument reports as provided online: ftp://ftp.ngdc.noaa.gov/STP/space-weather/solar-data/solar-features/solar-flares/x-rays/goes/ and from www.SolarMonitor.org.

The properties of the CMEs are taken from the SOHO/LASCO CME catalog [7]: http://cdaw.gsfc.nasa.gov/CME_list/

Online Catalog

The present structure of the catalog is shown in Figure 2. This is a snapshot of the web-based interface dedicated to the catalog: **http://newserver.stil.bas.bg/SEPcatalog/index.html**

Catalog
of
solar energetic particles

from Wind/EPACT instrument

Solar cycle 23: 1996-2008 Solar cycle 24: 2009-present

Event date	19-28 MeV			28-72 MeV	Flare	CME	Comment
yyyy-mm-dd	onset time (UT)	peak time (UT)	J_p (cm^2 s sr MeV)$^{-1}$	J_p (cm^2 s sr MeV)$^{-1}$	SXR class/ onset time (UT)/ location	time (UT)/ speed (km s^{-1})/ width (deg)	
2009	-	-	-	-	-	-	no SEP events
2010-06-12	04:04	08:39	0.0123	0.002	M2.0/00:30/N23W43	01:32/489/119	
2010-08-03	15:13	18:25	0.0478	0.0014	u	u	
2010-08-07	22:45	01:43nd	0.0111	0.0014	M1.0/17:55/N11E34	18:36/871/360	
2010-08-14	11:15	13:05	0.158	0.0184	C4.4/09:38/N17W52	10:12/1205/360	
2010-08-18	08:01	12:18	0.0486	0.0034	C4.5/04:45/N17W95	05:48/1471/184	
2010-09-09	03:02	04:25	0.0071	0.0007	C3.3/23:05/N19W91	23:27/818/147	

Fig.2. Snapshot of the first online version of the proton catalog.

The catalog consists of two identical in contents web-pages, dedicated to events in solar cycle (SC) 23 and 24, respectively. The default page gives the recent proton event list, namely in SC24. The catalog is organized as an electron table, where each row is designed for a specific proton event and its solar origin. Links to the overview plots (as in Figure 1) in both energy channels are available. The details are given in separate columns with overhead titles, as described below.

Column 1: yyyy-mm-dd

The first column gives the event date, abbreviated as year (yyyy), month (mm) and day (dd).

Column 2: onset time (UT)

The time of 3-sigma increase of the proton profile in the low energy channel (19-28 MeV) is reported here in universal time (UT) units, in standard format (hh:mm).

Column 3: peak time (UT)

The peak time of the proton event in the low energy channel is given in UT.

Column 4: J_p (cm^2 s sr MeV)$^{-1}$

This column presents the peak proton intensity in the low energy channel.

Column 5: J_p (cm^2 s sr MeV)$^{-1}$

Peak proton intensity in the high energy channel (28–72 MeV) is shown here.

Column 6: Flare

This column lists the flare soft X-ray (SXR) class, onset time in UT and location on the solar surface.

Column 7: CME

Here, we provide the time of first appearance of the CME in UT, its projected speed (in km/s) and angular width (in degrees).

Column 8: Comment

This column is dedicated for additional information about the proton event or related phenomena.

Below the table, we provide links to the Wind/EPACT data and instrument, a concise summary on the proton data analysis, a list of the abbreviations used in the catalog, the reference paper(s), and contact information.

Summary

At present the proton data analysis and solar origin are completed by the end of 2015. A dedicated publication (under completion) will present the statistical results based on SEP observations over nearly two solar cycles. Several planned improvements in the online catalog are considered, such as search and sort options in order to improve the visibility of the catalog contents. Yearly updates of the catalog are scheduled and will be completed in the beginning of the following year in order to account for delays in the proton/flare/CME data release. This online catalog will be further supported by the Space Climate group in the Space Research and Technology Institute, Bulgarian Academy of Sciences.

Acknowledgements

We appreciate the open data policy of the Wind/EPACT instrument. The CME catalog is generated and maintained at the CDAW Data Center by NASA and The Catholic University of America in cooperation with the Naval Research Laboratory. SOHO is a project of international cooperation between ESA and NASA. Heliospheric Shock Database is generated and maintained at the University of Helsinki.

References

[1] Gloeckler, G. In situ detection of energetic particles. // Heliophysics: Space Storms and Radiation: Causes and Effects, eds. C. J. Schrijver and G. L. Siscoe, Cambridge University Press – 2010 – P:43-77.

[2] Schwenn, R. Space Weather: The Solar Perspective. // Living Reviews in Solar Physics. – 2006. – 3(2).

[3] Cane, H. V., Richardson, I. G., von Rosenvinge, T. T. A study of solar energetic particle events of 1997-2006: Their composition and associations. // Journal of Geophysical Research. – 2010. – 115(A8). – CiteID A08101.

[4] Vainio, R., Valtonen, E., Heber, B. et al. The first SEPServer event catalogue ~68-MeV solar proton events observed at 1 AU in 1996-2010. // Journal of Space Weather and Space Climate. – 2013. – 3. – id.A12.

[5] Haggerty, D. K.; Roelof, E. C. Impulsive Near-relativistic Solar Electron Events: Delayed Injection with Respect to Solar Electromagnetic Emission. // The Astrophysical Journal. – 2002. – 579(2). – P:841-853.

[6] von Rosenvinge, T. T, Barbier, L. M., Karsch, J. et al. The Energetic Particles: Acceleration, Composition, and Transport (EPACT) investigation on the WIND spacecraft. // Space Science Reviews. – 71(1-4). – P:155-206.

[7] Gopalswamy, N, Yashiro, S., Michalek, G., Stenborg, G., Vourlidas, A., Freeland, S., Howard, R. The SOHO/LASCO CME Catalog. // Earth, Moon, and Planets. – 2009. – 104(1-4). – P:295-313.

Proceedings of
Eighth Workshop "Solar Influences on the Magnetosphere, Ionosphere and Atmosphere"
Sunny Beach, Bulgaria, May 30 - June 3, 2016

Relationships in the System Disk - Corona

Krasimira Yankova

Space Research and Technology Institute – Bulgarian Academy of Sciences
e-mail: *f7@space.bas.bg*

Abstract

Modern astronomy is allowed to register quasars at the core of all known spiral galaxies, including our own: From some time there is a good trend to seek a unified model of AGN. Group of a one hundred and forty authors A. A. Abdo et al. (2009), started an observation program whose main conclusions are that no matter the host galaxy, a core is quasar and shows similar structure and the same mechanism of development. Differences in the observations are the result only of different levels of accretion, mass and direction monitoring.

In this paper will consider the structuring of the flow on the system disk – corona around the central black hole. We discuss the behaviour on the border between components. We analyze mechanism of development of the advective hypothesis in case of falling away some restrictions from the model.

Introduction

Accretion disks (AD) are among most widespread objects in the universe, not only in temporal and spatial, but in evolutionary regard. For example Quasars are objects with large redshifts; most of them belong to the early universe. On the other hand ADs are present in almost all stages of the evolution of stars and their subsystems. Accretion on the compact object is particularly effective, and the presence of a magnetic field makes it possible to observe very attractive phenomena, like as disc's corona, jets and more. They are a manifestation of the high energy efficiency of the object.

We have developed a new model of the accretion disc's magneto-hydrodynamics, based on deformationless advective hypothesis, presented in Yankova (2013, 2015a).

Advection Mechanism

We constructed geometrically thin, optically thick, one-temperature Keplerian disc in a normal magnetic field, around a black hole. In this case more authors have considered advective-dominated sub-and super-Eddington flows. More popular models suggest a flow deformation, such as: rotation of the velocity vector for radial advection, see Beloborodov (1998), Bisnovatyi-Kogan (1998, 1999, 2002), Chen et al. (1997), Narayan et al. (1997), Narayan and Yi (1995); or orbital advection for low- magnetic discs, where orbital speed vector is added to the Keplerian velocity see Fabian et al. (2012). At these types of advection action of $\partial v_i / \partial t$ is ignored.

In our research, in contrast to these models, we provide the advection in the form of the complete advective term (1.1), which is naturally produced in the equations describing the flow dynamics:

$$\frac{\partial(\rho \boldsymbol{v}_i)}{\partial t} + \frac{\partial}{\partial x_j}\left(\rho \boldsymbol{v}_i \boldsymbol{v}_j\right) = \rho\left(\frac{\partial \boldsymbol{v}_i}{\partial t} + \boldsymbol{v}_j \frac{\partial \boldsymbol{v}_i}{\partial x_j}\right) = \rho \frac{\boldsymbol{D}\boldsymbol{v}_i}{\boldsymbol{D}t} \qquad (1.1)$$

In the presented new interpretation of physics at the left side of the equation for the motion: complete advective term is a complete differential: This means that arises a shifting of the average flow with velocity $\boldsymbol{v_i}$ in any direction.

When the advection is non-dominant mechanism, there is not a condition of flow deformations - does not indicate the individual modification of one or other of the velocity components. The full advective term transfers the solution as a whole into smaller radii, retaining his nature. Does not ignored the action of $\partial v_i / \partial t$.

Contribution of the magnetic field

Determine the direction of the middle flow displacement in the disc uniquely [Campbell et al. (1998).

It gives additional dissipative mechanism which directly affects the development of the gradient of entropy in the disc.

Sign of the entropy

Negative gradient of entropy $\partial_t S$ determined the basic criterion for development and the self-induction on the advection.

Entropy

In the theory the seeked a unified model of AGN starts earlier. Based on the similarity of the morphology of the object (BH + disc + crown + jets) and the spectrum of jets at different masses (CBS and AGNs) (Machida et al. 1999) express hypothesized that in both cases they result from general physical mechanism. Their idea is mathematically justified by the relationship between the emission of jets with the mass of BH and accretion activity. The hypothesis was tested in a standard classification $1M_o$ to 10^6M_o ($1M_o$ – solar masses). The measurements show a linear correlation (L_X, L_R) that may be predicted theoretically, which practically proves the hypothesis.

We applied us unified model in the real highly energy efficient sources: Cyg X-1(CBS) and SgrA * - the core of our galaxy. In such active discs dissipation is faster than diffusion. The disc cannot re-radiate fully the deliverances energy. It is converted into heat and remains therein. Produced power influence the sign of entropy.

Presented results for the two concrete objects showed that functions of distributions of the gradient of entropy in both cases are qualitatively similar and gradients has negative sign in the inner regions.

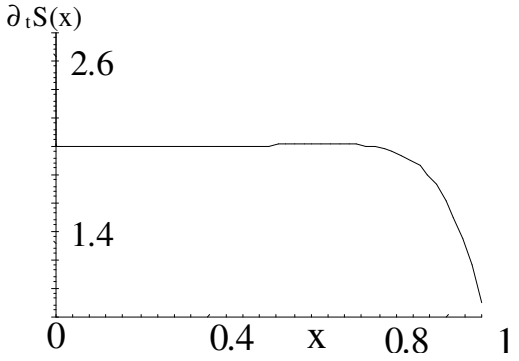

Fig.1a: Development of the gradient of entropy ∂tS(x) over dimensionless radius of the disk x = r/rout, (rout=103Rg)in Cyg X-1.

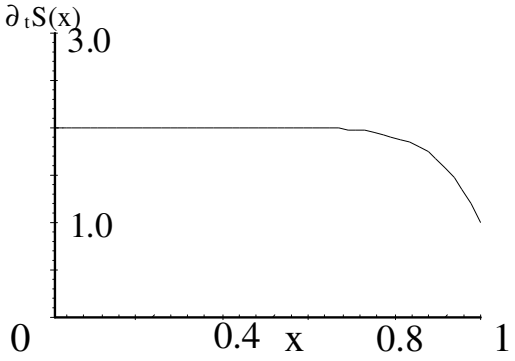

*Fig.1b: Development of the gradient of entropy ∂tS(x) over dimensionless radius of the disk x = r/rout , (rout=100Rg)in SgrA**

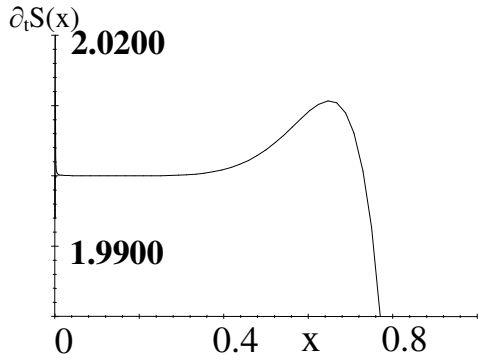

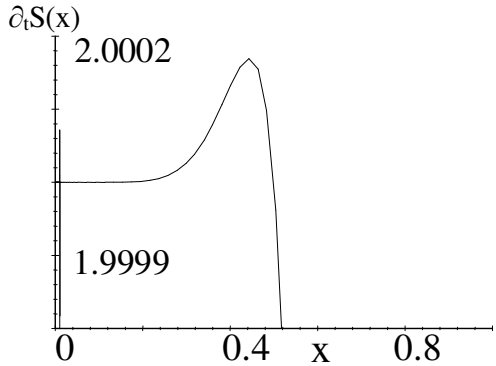

At Cyg X-1 gradient of entropy increases from unit to 2.0000 in the range (0.7, 1) x, we have a maximum a value of 2.0100 at $650R_g$ and weak negative entropy gradient in the interval x ~ 0.16 ÷ 0.65, from which it follows that a significant part of energy remains in the disk and powered instabilities. After x ~ 0.15 again have a positive gradient of entropy and it remains so to the inner edge of the disk $r_{in}=100R_g$ – Schwarzschild radii.

At SgrA * gradient of entropy increases from unit to 2.0000 in the range (0.5, 1) x, we have a maximum a value of 2.0002 at $45R_g$ and more weak, but well expressed negative entropy gradient in inner regions x < 0.45 ($45R_g$). There is no minimum. $r_{in}=3R_g$

By the development of the components of the magnetic field provides information about the microstructures present in the stream, and their behaviour. They control the physical parameters of flow and redistribution of energy in the real objects: and shows that in the inner regions of the disc not only the entropy gradient is negative, but maintained tendency to remain negative, so even to oust the outside radius of the reversal of its sign.

As already shown in Yankova (2015 b) In Cyg X-1 has asymmetry in $\boldsymbol{B}$, which maintains continuous cascade plurality of different sized loops - both positive and negative relative to the direction of flow. The behaviour of the magnetic field In Sgr A * shows the existence of different groups MPH (discrete cascade); with the exchange of energy between the low and high harmonics in the size-spectrum and between components field respectively. In both cases the existing microstructures in the flow absorbing energy from the environment, keep it to disk and then maintains the negative gradient of entropy (fig.1). Negative entropy keeps advection able of the self-induction.

The advection with this type self-induction can work for the relatively lower temperatures and can start in the outer regions of the disc. The earlier advection appearances, guarantee that the flow will remain optically thick at the temperatures of orders (1, 2) which are higher than the normally accepted one.

Behaviour on the border

Vertical distributions of sound and magnito-sonic velocity is especially sensitive to the exchange and distribution of energy in the disk and accordingly to the type of advection. Namely those distributions play a major role to the type of boundary between components in the system corona - disk. They controlled interaction between parameters and the impact of nonlinear effects i.e. feedback in the flow over the boundary.

Analyze

The model is built on the concept to action of the complete advective term and behaviour of the arising as corollaries of this mechanism direct and feedbacks in the stream. Flow is considered non-relativistic because $(v^2/c^2) \sim 4.10^{-2} << 1$, but relativistic effects that compact object exercise are included in the examination of pure Newtonian flow (Abramowicz et al., 1988; Yankova 2015a) in an appropriate manner. However idealizations hypothesis is workable and adequate.

Model opens up opportunities for the naturally upgrade and we should note that restriction the Newtonian approximation for more of the real objects is not applicable.

With the transition to numerical investigation can to drop some restrictions, but most important consequence advantage of the conception: equations remain nonlinear is applicable in new conditions.

In Post-Newtonian development of formula (1.1) in the GR, $\frac{\partial \boldsymbol{v}_i}{\partial}$ is equal rights component.

$$\frac{\partial(\rho \boldsymbol{v}_i)}{\partial} + \frac{\partial}{\partial \chi_j}(\rho \boldsymbol{v}_i \boldsymbol{v}_j) = \rho\left(\frac{\partial \boldsymbol{v}_i}{\partial} + \boldsymbol{v}_j \frac{\partial \boldsymbol{v}_i}{\partial \chi_j}\right) = \rho \frac{\boldsymbol{D}\boldsymbol{v}_i}{\boldsymbol{D}} \tag{2.1}$$

We are expecting in new non-stationary nonlinear relativistic environment all the more stronger expression of advective mechanism. It will show to what extent is global at dropping the Newtonian approximation. Independently from analogical the general appearance of advective term, in this environment, it will show the full potency of the mechanism.

Arises the question is there a causality of the metrics of space-time, regardless of the thermal excitation?

Conclusion

In this paper, we determine the direction of for creating full model of the system disk-corona. Dropping the Newtonian approximation determining degree to which the main component influenced the development of coronary component. At the same time in the disk's corona the density can falling sharply and we can no more ignored quantum effects in radiative processes.

References

Abdo, A. A. et al. 2009, Radio-Loud Narrow-Line Seyfert 1 as a New Class of Gamma-Ray Active Galactic Nuclei, Ap J Letters, Volume 707, Issue 2, pp. L142-L147.

Abramowicz M. A., Czerny, B., Lasota, J. P., Szuszkiewicz, E.,1988 Slim accretion disks, ApJ, 332 646-658.

Beloborodov, A. M.: 1999, Accretion Disk Models, arXiv: astro-ph/9901108.

Bisnovatyi-Kogan, G.S.: 1998, Accretion Disc Theory: From the Standard Model Until Advection, arXiv: astro-ph/9810112.

Bisnovatyi-Kogan, G.S.: 1999, Accretion Discs Around Black Holes: Developement of Theory, arxiv astro-ph/9911212.

Bisnovatyi-Kogan, G.S., Lovelace, R.V.E.: 2002, Advective Accretion Disks and Related Problems Including Magnetic Fields, arXiv:astro-ph/0207625v1.

Campbell C. G., Papaloizou J. C. B., Agapitiu V.: 1998, Magnetic field bending in accretion discs with dynamos, MNRAS 300, 315-320.

Chen, X., Abramowicz, M. A., Lasota, J.P.: 1997, Advection-dominated Accretion: Global Transonic Solutions, ApJ 476, 61-69.

Fabian, A.C., Wilkins, D.R., Miller, J.M., Reis, R.C., Reynolds, C.S., Cackett, E.M., Nowak, M.A., Pooley, G.G., Pottschmidt, K., Sanders, J.S., Ross, R.R., Wilms, J.: 2012, On the determination of the spin of the black hole in Cyg X-1 from X-ray reflection spectra, http://www.astro.umd.edu//symbol%7126%7d%25chris/publications/papers/fabian12a.pdf

Igumenshchev, I.V., Abramovich, M.A.: 2000, Two-dimensional Models of Hydrodynamical Accretion Flows into Black Holes, ApJ 130, 463-484.

Machida M., Hayashi M. R., Matsumoto R., Global Simulations of Differentially Rotating Magnetized Disks : Formation of Low-Beta Filaments and Structured Corona, arXiv: astro-ph/9911291, 16 Nov 1999.

Narayan, R., Kato, S., Homn, F.: 1997, Global Structure and Dynamics of Advection-dominated Accretion Flows around Black Holes, AJ 476, p. 49.

Narayan, R., & Yi: 1995, Advection-Dominated Accretion around Black Holes, ApJ 452, 71.

Yankova Kr.D.: 2013, Generation and development of the disk corona, Proceedings of the VIII Serbian-Bulgarian Astronomical Conference (VIII SBAC), Publ. Astron. Soc. "Rudjer Bošković" vol. 12, 375-381. http://wfpdb.org/ftp/8_SBAC_D1/pdfs/34.pdf

Yankova Kr.: 2015a, MHD of accretion-disk flows, BlgAJ, Vol. 22, p. 83. http://adsabs.harvard.edu/abs/2015BlgAJ..22...83Y

Yankova Kr.: 2015b, Analysis of the Nonlinear Behavior of the Accretion Flows, (2015) Proceedings of Seventh Workshop "Solar Influences on the Magnetosphere, Ionosphere and Atmosphere", pp.25-28, ISSN 2367-7570,

Proceedings of
Eighth Workshop "Solar Influences on the Magnetosphere, Ionosphere and Atmosphere"
Sunny Beach, Bulgaria, May 30 - June 3, 2016

Magnetic substorms of different types during the 23 and 24 solar cycles

I.V. Despirak [1], *A.A. Lubchich* [1], *N.G. Kleimenova* [2, 3]

[1] Polar Geophysical Institute RAS, Apatity, Russia
[2] Schmidt Institute of the Earth Physics RAS, Moscow, Russia;
[3] Space Research Institute RAS, Moscow, Russia
E-mail: despirak@gmail.com

Abstract.

On the base of the IMAGE magnetometers data, and the OMNI solar wind and interplanetary magnetic field (IMF) data, we have analyzed the occurrence of the magnetic substorms during the 23-th and 24-th solar cycles. All considered substorms were divided into 3 types according to their location in relation to the auroral oval dynamics. The first type – the substorms which are observed only at the auroral latitudes (called "usual" substorms); the second type – the substorms which propagate from the auroral geomagnetic latitudes to the polar ones (called "expanded" substorms, according to an expanded oval dynamics); and the third type – the substorms which are observed only at the geomagnetic latitudes above ~70 degrees in the absence of simultaneous magnetic disturbances below 70 degrees (called "polar" substorms, according to a contracted oval dynamics). We have analyzed the space weather conditions before the onset of these three types of substorms. Namely, we have considered the influence of the different types of the solar wind streams, of the magnetic storm intensity (or the non-storm conditions), of the geomagnetic indexes values etc. The substorm seasonal variations have been studied as well. It was found that although "polar" and "expanded" substorms observed at almost identical high geomagnetic latitudes, they appear under different space weather conditions. We argue that the space weather conditions differ for different types of the considered substorms and could be a useful tool for the investigation of the various magnetospheric plasma processes (or their location) caused these substorms.

Introduction

It is known that under normal conditions (moderate disturbance) the auroral oval is located at the geomagnetic latitudes (GLAT) of about 65-67° ("normal oval"), under the quiet conditions (at $B_Z>0$), the auroral oval shrinks and moves to higher latitudes (>70° GLAT, "contracted oval"), and in the disturbed conditions (increased magnitude of the negative IMF B_Z component), the equatorward boundary of the oval is shifted down to 50° geomagnetic latitude, while its poleward boundary extends to higher latitudes ("expanded oval") (Feldstein and Starkov, 1967). A search for difference between substorms occurring on the "normal", "contracted" and "extended" oval for a long time attracted the attention of the researchers (Akasofu 1973). In different studies, substorms were divided into "confined" and "widerspead" (Lui et al., 1975), "localized" and "normal" (McPherron, 1973),"those on a contracted oval" and "normal" (Kamide et al. 1975), "small" and "normal-size" (Petrukovich et al., 2000). It should be noted that many studies provided details of the spatial and temporal behavior of both substorm, the westward electrojet and auroras at extremely high latitudes of an expanded oval (Gussenhofen, 1982; Yahnin et al. 2004). The substorms which propagate to very high latitudes were often considered as a separate type of substorms and called "high-latitude" substorms (Sergeev et al. 1979; Despirak et al. 2008) or "substorms with large poleward expansion" (Kuznetsov et al., 2001)

In our work we divided all observed substorms into 3 groups according to auroral dynamics. In our terminology, we call the first type of substorms as "usual" substorms, i.e. substorms which are observed only at auroral latitudes. Similarly to the auroral oval which is called an

"expanded" oval, meaning its extension in the disturbed conditions, we will call "expanded" substorms those which start at the auroral zone and then propagate to very high latitudes. We point out that in the maximum phase of "expanded" substorms, the westward electrojet can be observed at very high geomagnetic latitudes (> 75º) (Despirak et al., 2008). The third type of substorms, termed as "polar" substorms, correspond to the contracted oval. They represent isolated bay-like magnetic disturbances, observed at the geomagnetic latitudes higher than the location of the typical polarward boundary of the auroral oval (> 70° GLAT) and are not accompanied or preceded by substorm activity at the auroral latitudes.

The aim of this work is the comparison of the space weather conditions before the onset of these three types of substorms observed during the 23 and 24 solar cycles. Namely, occurrences of magnetic substorms during periods close to the solar cycles maximums (1999-2000, with the Wp> 100) and (2012-2013 with Wp ~ 60) and during two solar cycles minimums (1995-1996) and (2008-2009) were analyzed.

Data

We used the magnetic data of the IMAGE meridional chain Nurmijarvi - Ny Alesund, from 57º to 75º of geomagnetic latitudes. The solar wind and Interplanetary Magnetic Field (IMF) parameters measured by Wind spacecraft were taken from OMNI database. The 1995-1996, 1999-2000, 2008-2009 and 2012-2013 time intervals, close to two different maximums and minimums of the solar activity are used. There were analyzed above 3500 events of "expanded", "polar" and "usual" substorms in the listed above years.

Results

a) Seasonal variations of substorm number

We calculated the seasonal variations of substorms, observed in 4 different periods – in 1995-96, 1999-2000, 2008-2009 and 2012-2013 years. Figure 1 presents the results for 4 different types of substorms: A- all substorms; U- classical (usual) substorms; P- "polar" substorms; E- "expanded' substorms.

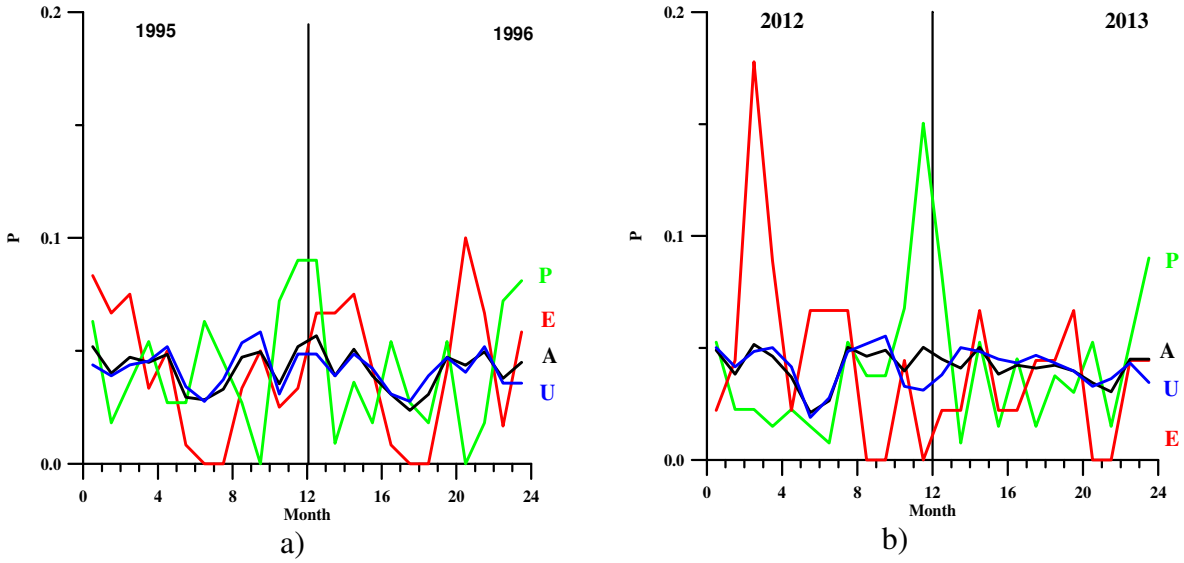

Fig. 1 The normalized to the total substorms number distribution of substorm number by month for different types of substorms: a)- in 1995-1996 years ; b) – in 2012-2013 years

It is seen that number of substorms is higher in 1999-2000 (1995-96) than in 2012-2013 (2008-09); the summer minimums of substorms number and spring and autumn maxima are common to both periods; polar substorms behavior was in opposition to "expanded" substorms behavior.

b) The values of the PC index before substorm onsets for 4 types of substorms

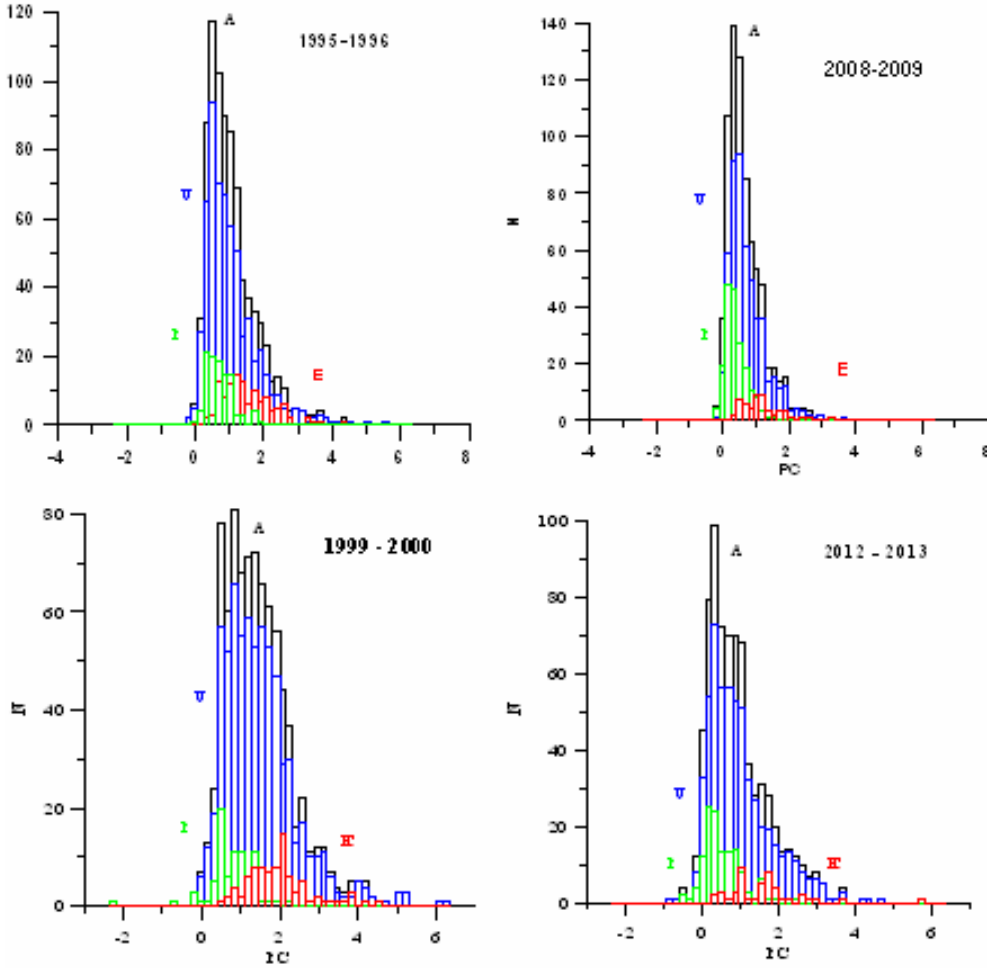

Fig. 2 PC index before substorm onsets for 1995-9996, 1999-2000 (left columns) and for 2008-2009, 2012-2013 (right columns)

It can be seen that the highest PC-index values are observed before the occurrence of the "expanded" substorms, the lowest value of the PC-index before the occurrence of the "polar" substorms, while the "usual" substorms occur at intermediate values of the PC-index. Thus, the PC-index values were 2.57-3.06 times less for the "polar" substorms than for the "expanded" substorms. It should be also noted that the PC-index values for substorms during solar cycle minimums (1995-96 and 2008-09) are ~ 1.3 times lower than for substorms during the solar cycle maximums (1999-2000 and 2012-2013).

c) Solar wind parameters before the onset of substorms

We considered the solar wind and IMF parameters observed before the onset of the three types of substorms. We downloaded the values of the following solar wind parameters: the B_X, B_Y, B_Z components of IMF, V_X component of the solar wind velocity, E_Y component of the interplanetary electric field, temperature (T), density (N) and dynamic pressure (P) of the solar wind (not presented here). It is shown that significant differences in the distributions of these solar wind parameters between substorms during 23 and 24 solar cycle, namely between substorms observed in 1995-1996, 1999-2000, 2008-2009 and 2012-2013 have been not found. However, there is a significant difference between "polar" and "expanded" substorms: the first occur at low solar wind velocity and the second at values of solar wind velocity higher than 500 km/s. "Polar" substorms are observed after the passage of a HSS of the solar wind (when the velocity is reduced from high to low values). "Expanded" substorms, on the contrary, are observed during the passage of a HSS of the solar wind, increased temperature and pressure of the solar wind.

Conclusions

1. Number of substorms is higher in 1999-2000 (1995-96) than in 2012-2013 (2008-09); the "polar" substorms behavior was opposite to the "expanded" substorms behavior.
2. There were no significant differences of the solar wind parameters before the substorms in the different solar cycle periods. "Polar" substorms are observed after the passage of a HSS of the solar wind (when the velocity is reduced from high to low values). "Expanded" substorms, on the contrary, are observed during the passage of a HSS of the solar wind, increased temperature and pressure of the solar wind.
3. For all three types of substorms which observed during 24 solar cycle, the PC-index values are lower than for substorms during the 23 solar cycle; the PC-index values for substorms during solar cycle minimums (1995-96 and 2008-09) are ~ 1.3 times lower than for substorms during the solar cycle maximums (1999-2000 and 2012-2013); the PC-index values are 2.6 - 3.0 times lower for the "polar" substorms than for the "expanded" substorms.

Acknowledgment

This study was supported by Program No 7 of the Presidium of the RAS. The study is part of a joint Russian - Bulgarian Project 1.2.10 of PGI RAS and IKIT-BAS under the Fundamental Space Research Program between RAS and BAS.

References

Akasofu S-I, P.D. Perreault, F. Yasuhara, C.-I. Meng (1973). Auroral substorms and the interplanetary magnetic field. J Geophys Res, 78, 7490–7508.

Despirak, I.V., A.A. Lyubchich, Kh.K. Birnat, A.G. Yakhnin (2008), Poleward expansion of the westward electrojet depending on the solar wind and IMF parameters. Geomagn. Aeron., 48, no. 3, 284-292.

Feldstein, Y.L. and G.V. Starkov (1967), Dynamics of auroral belt and geomagnetic disturbances. Planet. Space Sci., 15, 209-229.

Gussenhoven M.S. (1982) Extremely high latitude auroras. J Geophys Res., 87, 2401-2412.

Kamide Y, S.-I.Akasofu, S.E. DeForest, J.L. Kisabeth (1975) Weak and intense substorms, Planet Space Sci., 23, 579-587.

Kuznetsov S., L.L. Lazutin, T. Rosenberg, L. Borovkov, Yu. Gotselyuk, A. Weatherwax (2000) Energetic electron and ion dynamics and polar aurora during magnetospheric substorm of March 10, 1994. In: Wilson A (ed) Proceedings of the 5th International Conference on Substorms, Conference on Substorms, St. Petersburg, Russia, 16–20 May 2000 (ESA SP-443, July 2000), 511–514.

Lui ATY, C.D. Anger, S.-I. Akasofu (1975) The equatorward boundary of the diffuse aurora and auroral substorms as seen by the Isis 2 auroral scanning photometer. J. Geophys Res, 80, 3603–3614.

McPherron R.L, C.T. Russell, M.G. Kivelson, P.J. Jr Coleman (1973) Substorms in space: The correlation between ground and satellite observations of the magnetic field. Radio Science, 8, 1059-1076.

Petrukovich AA, Baumjohann W, Nakamura R, Mukai T, Troshichev OA (2000) Small substorms: Solar wind input and magnetotail dynamics. J Geophys Res, 105, 21109-21118..

Sergeev V.A., A.G. Yakhnin, N.P. Dmitrieva (1979) Substorms in the polar cap – the effect of high-velocity streams of the solar wind. Geomag Aeron (in Russian), 19, 1121–1122.

Yahnin AG, Despirak IV, Lubchich AA, Kozelov BV (2004) Solar wind control of the auroral bulge expansion. In: Ganushkina N and Pulkkinen T (eds) Proceedings of the 7th International Conference on Substorms, Conference on Substorms, Levi, Finland, 21–27 March 2004 (Reports No. 2004:5, Finnish Meteorological Institute, Helsinki 2004), 31–33.

Proceedings of
Eighth Workshop "Solar Influences on the Magnetosphere, Ionosphere and Atmosphere"
Sunny Beach, Bulgaria, *May 30 - June 3, 2016*

Temporal behaviour of daytime VLF emissions caused by the solar wind and IMF disturbances: a case study

J. Manninen [1], N.G. Kleimenova [2,4], T. Turunen [1], L.I. Gromova [3]

[1] Sodankyla Geophysical Observatory, Sodankyla, Finland
[2] Schmidt Institute of the Physics of the Earth RAS, Moscow, Russia
[3] Pushkov Institute of Terrestrial Magnetism, Ionosphere, and Radio wave Propagation RAS, Troitsk
[4] Space Research Institute RAS, Moscow, Russia

Abstract

The analysis of the temporal variations of the daytime 1-6 kHz VLF emissions was made during moderate magnetic storm (Kp=6) occurred on 8 December 2013. The storm was associated with the Coronal Mass Ejection (CME). The VLF emissions were recorded in the frequency band of 0.2–39 kHz during the dark winter at Kannuslehto (KAN, L~ 5.5) in Northern Finland. The analysis results were compared with simultaneous variations in the solar wind and Interplanetary Magnetic Field (IMF). It was found that intense VLF hiss emissions started after the solar wind dynamic pressure jump (from 7 to 12 nPa) under the positive IMF Bz. The VLF emissions occurred in two separate frequency bands. The lower frequency (below ~2 kHz) band represents the strong long lasting hiss with right-hand polarization, and in the upper frequency band (above ~2 kHz) the left-hand polarized hiss bursts occurred during about 1 hour. The plasmasphere was strongly compressed, and due to that KAN was mapped outside of the plasmapause. We suppose that VLF hiss emissions exited in the magnetosphere by the cyclotron instability of the radiation belt electrons. The low frequency hiss was generated outside of the plasmapause and arrived to KAN along the meridional direction. The high-frequency band was generated inside of the plasmasphere arrived to KAN almost along the meridian. The opposite VLF emission dynamics, namely, the wave suppression, was revealed in association with sudden drop of the solar wind dynamic pressure.

Introduction

Natural electromagnetic plasma waves at the audio frequencies from 30 Hz to 30 kHz, known as extremely low (ELF) and very low frequency (VLF) emissions, are common phenomena in the magnetospheric plasma [Helliwell, 1965]. Typical VLF emissions known as chorus and hiss have been observed both on the ground and in the space by satellites. These VLF waves are generated in the magnetosphere via resonant interaction between the waves and energetic particles in the inner magnetosphere [e.g., Trakhtengerts, 1963; Kennel and Petshek, 1966; Trakhtengerts and Rycroft, 2008] and believed to play a controlling role in the dynamics of Earth radiation belts. Here we study the ground-based daytime VLF emissions caused by variations in the solar wind and Interplanetary Magnetic Field (IMF) during the moderate magnetic storm (Kp = 6, Dst ~ -70 nT) on 8 December 2013.

Observations

The ELF-VLF emissions in the frequency range of 0.2-39 kHz were recorded at Kannuslehto site (KAN, geographic coordinates 67.74°N, 26.27°E, L~ 5.5) in auroral latitudes of Northern Finland (Fig. 1a). Several wintertime VLF campaigns have been carried out in 2006-2016. It was found that even at the auroral latitudes, at frequencies higher than about 3 kHz, there was a very strong level of atmospherics or sferics, i.e. electromagnetic signals originated in lightning discharges. These waves can propagate to the long distance in the atmospheric waveguide between the Earth surface and ionospheric D region [e.g., Ohya et al., 2015]. The sferics are so strong that they hide all other natural emissions at same

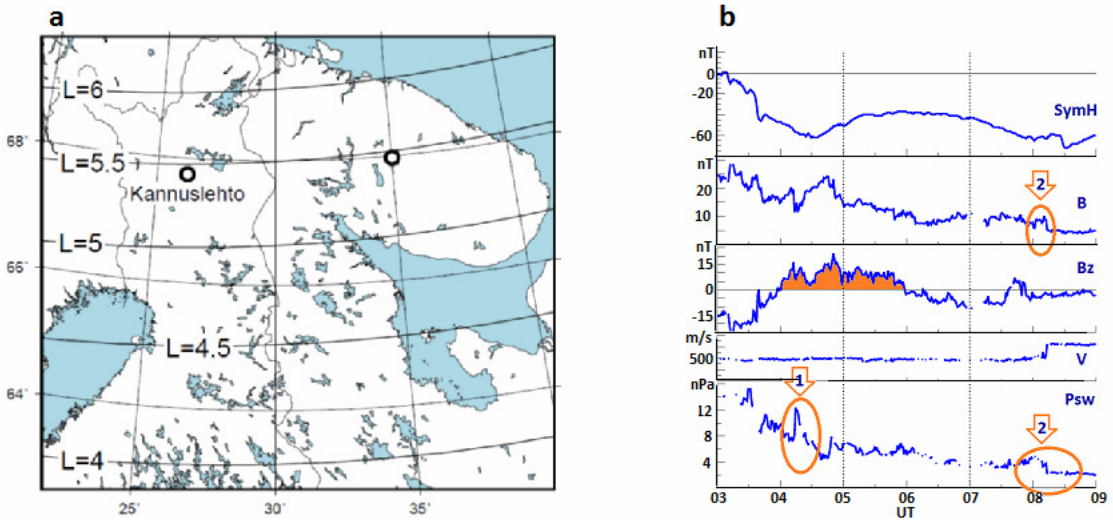

Fig.1. (a) - the map of KAN location, (b) - the geomagnetic data: SymH index, IMF (B, Bz) values, solar wind speed (V) and solar wind dynamic pressure (Psw).

frequency band. A specially designed digital program to filter out strong impulsive sferics has been developed and applied.

Here we present the analysis of the VLF observations during two time intervals of the magnetic storm on 8 December 2013 (Fig. 1b). The first interval (04-05 UT) was associated with the strong jump of dynamic pressure of the solar wind (Psw) observed under positive IMF Bz. During the second interval (08-09 UT), the solar wind dynamic pressure and IMF B dropped suddenly. According to Van Allen Probes satellite (http://enarc.space.swri.edu/PTP) KAN was mapped outside of the plasmapause during both intervals (Fig. 2).

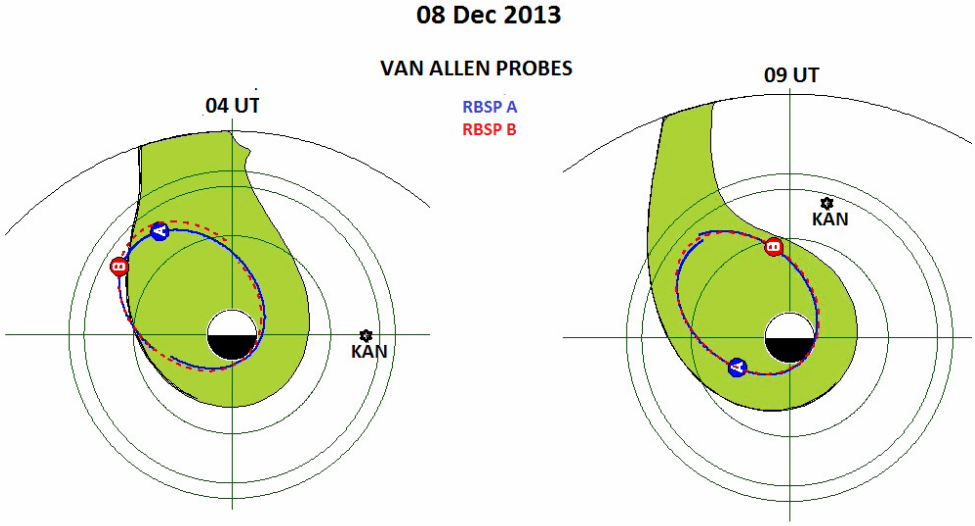

Fig.2. The plasmapause location.

The VLF spectrograms (the total, left-hand and right-hand polarized wave power) are presented in Fig. 3. The bottom panel (Az) shows the angle direction of the wave arrival, but not the vector of the wave arrival. The red color indicates the wave arrival roughly along the latitude (i.e., N-S direction), and green – along the longitude (i.e., E-W direction).

It is seen, that the VLF emissions at the frequencies above 2 kHz showed the left-hand polarization supported their long travelling in the Earth-ionosphere wave guide [Yearby and Smith, 1994] and arrived mostly along E-W direction. The VLF emissions at the frequencies below 2 kHz were right-hand polarized indicating that the ionospheric exit point of the wave was located not far from KAN. These emissions arrived almost along the N-S direction.

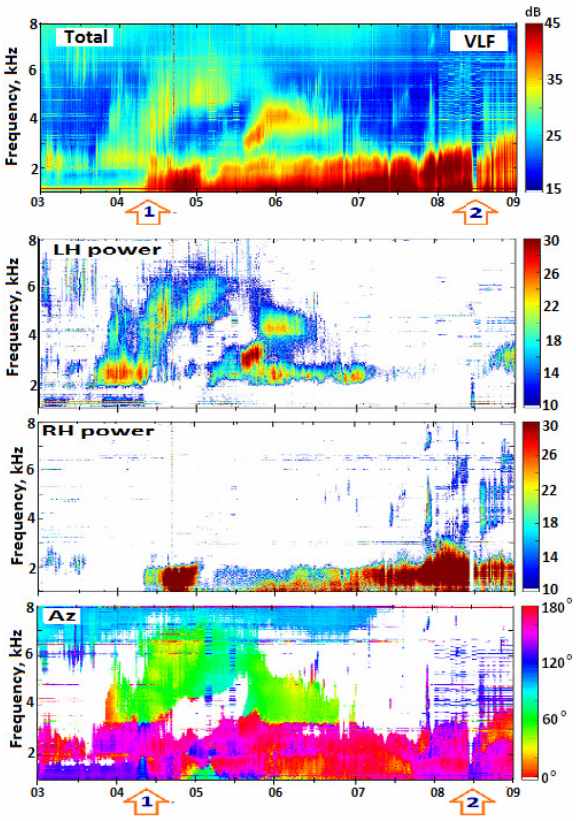

Fig.3. The VLF spectrograms (the total power, pure left-hand and pure right-hand circularly polarized wave power), bottom panel (Az) - the azimuthal angles of the wave arrival.

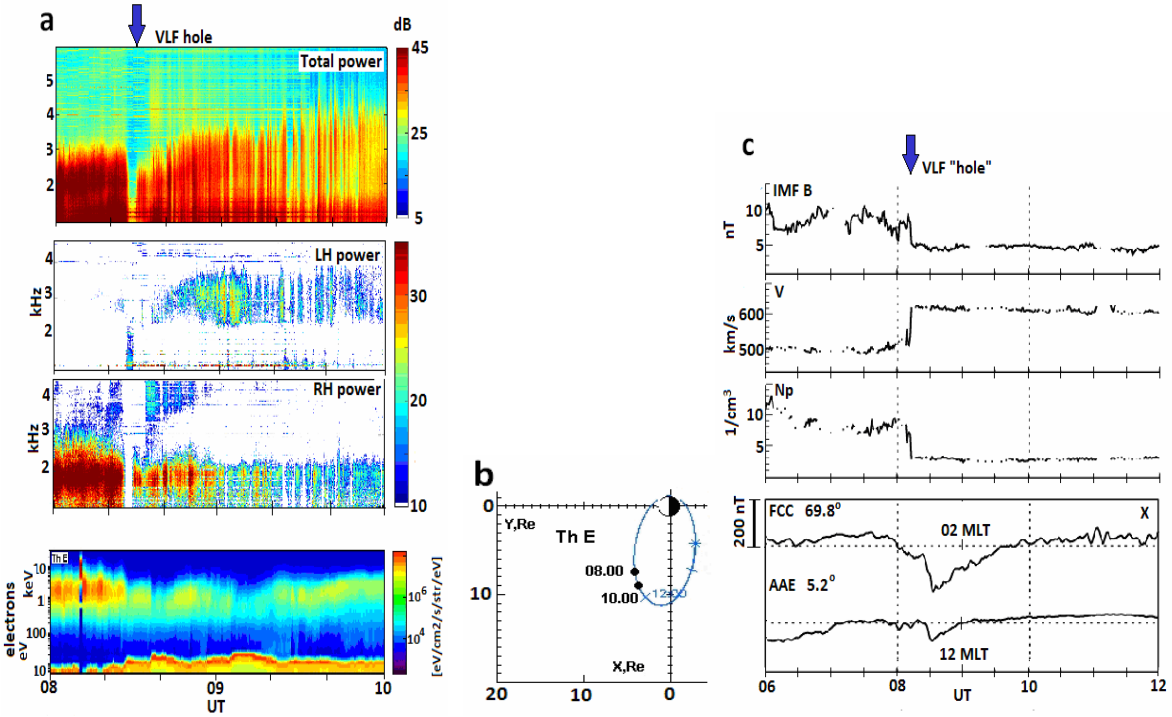

Fig. 4. The VLF total, left- and right-handed powers (a), bottom - THEMIS-E electron data and its location (b), (c) the IMF B, solar wind velocity (V) and density (Np) and substorm at Fort Churchill (FCC) accompanied by negative bay near equator Addis Abeba (AAE) at noon.

During the second interval (08-09 UT) a short suppression of VLF emissions ("hole") was observed (Fig. 4) simultaneously with a sharp drop of energetic electrons recorded at THEMIS-E in the magnetosphere. It is seen that after the "hole", the spectral structure of VLF

emissions changed. Strong continuous hiss at the frequencies below 2.5 kHz was replaced by structured hiss bursts in the broader frequency band, up to ~4.5 kHz, having the left-hand polarization at frequencies above ~2.5 kHz

Discussion

It is known that the solar wind is coupled to the magnetosphere via dynamic pressure and electric field. Pressure establishes the size and shape of the system. There are a variety of modes of response of the magnetosphere to the solar wind. One of them can be VLF whistler-mode wave generation by cyclotron instability of radiation energetic particles in the inner magnetosphere. The frequency of exited waves is controlled by the equatorial electron gyrofrequency f_{ce}, which is proportional to the local magnetic field strength. As a result of cyclotron instability, the energetic electrons change the pitch-angle and become precipitated.

The waves, generating near the magnetospheric equator, are guided to the ionosphere by the magnetic field with an upper cut-off frequency at $f_{ce}/2$. The f_{ce} value at magnetic field line of L~ 5.5 (KAN) is ~5 kHz. Thus, the wave propagated roughly along the KAN magnetic field line, can be detected on the ground only at $f \leq 2.5$ with right-hand polarization. Such waves are here seen as strong hiss in the bottom part of spectrograms in Fig. 3 and Fig. 4.

Summary

1. We found that the intense VLF hiss appeared after a jump in the solar wind dynamic pressure. It compressed the magnetosphere and plasmasphere. We suppose that the VLF hiss (below ~2 kHz) was generated outside of the plasmapause.
2. The high-frequency VLF band (above ~2 kHz) was, probably, generated inside the plasmasphere and arrived to KAN from lower L-shells along the Earth-ionosphere wave-guide becoming left-hand polarized.
3. The opposite VLF emission dynamics, namely, the wave suppression, was revealed in association with sudden drop of the solar wind dynamic pressure. That decreased the number and anisotropy of resonant particles and changed the VLF generation condition**.**

Acknowledgements.

The paper was supported by the Program No 7 of the Presidium of the Russian Academy of Sciences (RAS).

References

Helliwell, R.A. Whistler and related ionospheric phenomena. Stanford. Stanford Univ. Press. 1965.

Kennel, C. F., and Petschek, H. E. Limit of stably trapped particle fluxes, J. Geophys. Res. 71, 1-28, 1966.

Ohya, H., Shiokawa, K., and Miyoshi, Y. Daytime tweek atmospheric, J. Geophys. Res. Space Physics., 120, doi:10.1002/2014JA020375, 2015.

Trakhtengerts, V. Y. On the mechanism of VLF emissions generation on the external radiation belt of the Earth, Geomagn. Aeron. 3, 442-451, 1963.

Trakhtengerts, V.Y., and Rycroft, M.J. Whistler and Alfven Mode Cyclotron Masers in Space. Cambridge Univ. Press. Cambridge. U.K. 2008.

Yearby, K.H., and Smith, A.J: The polarization of whistlers received on the ground near L = 4, J. Atmos. Terr. Phys., 56, 1499-1512, 1994.

Proceedings of
Eighth Workshop "Solar Influences on the Magnetosphere, Ionosphere and Atmosphere"
Sunny Beach, Bulgaria, *May 30 - June 3, 2016*

High-latitude geomagnetic effects of strong positive IMF Bz: Case study

Gromova L.I. [1], *Kleimenova N.G.* [2,3], *Levitin A.E.* [1], *Dremukhina L.A.* [1], *Antonova E.E.* [3,4], *Gromov S.V.* [1]

[1] Pushkov Institute of Terrestrial Magnetism, Ionosphere, and Radio wave Propagation, RAS, Moscow
[2] Schmidt Institute of the Physics of the Earth RAS, Moscow, Russia
[3] Space Research Institute RAS, Moscow, Russia
[4] Skobeltsyn Institute of Nuclear Physics Lomonosov Moscow State University, Russia

Abstract

We present unusual negative magnetic bay-like disturbances occurred in the dayside sector of the Earth at the polar geomagnetic latitudes under positive IMF Bz during main phase of the storm on Nov 24, 2001 and recovery phase of the storm of May 30, 2003.

It is supposed that development of these dayside polar substorms could be a response of the magnetosphere to high positive values of the IMF *Bz* occurrence. The dayside polar magnetic substorms were observed in the polar region where the specific system (NBZ) of field-aligned currents, caused by the positive IMF *Bz,* may be enhanced. Our vector construction of geomagnetic data (Scandinavian magnetometer chain IMAGE) showed the clockwise vortex in the first event. In the second event, we detected two opposing vortices, which could be a proxy of an intensification of upward and downward field-aligned currents. Our IZMIRAN model estimations as well as the simultaneous DMSP and CHAMP satellites data support this assumption. According to OVATION model and the electron images from IMAGE satellite, the Scandinavian polar ground-based stations where these dayside polar magnetic substorms were observed, map into the dayside auroral oval, i.e. inside the closed magnetosphere.

Introduction

It is generally accepted that the solar wind energy input into in the magnetosphere under negative *Bz* component of the Interplanetary Magnetic field (IMF) and causes the nigh-side magnetic substorm developing. There is no IMF new energy input under the positive IMF *Bz*.

However, we found [Kleimenova et al., 2015] that during the main phase of the strong magnetic storm on Nov 24, 2001 (Dst *min* –220 nT), under a high solar wind dynamic pressure (up to 50–770 nPa) and nonordinary IMF conditions, namely, sudden occurrence of extremely high (up to ~60 nT) positive IMF *Bz* values, unusual dayside negative magnetic bay at polar latitudes developed with the amplitude of about 2000 nT. A rather similar event was observed in the recovery phase of the magnetic storm of May 30, 2003(Dst *min* -144 nT) [Levitin et al., 2015].

The aim of this paper is to study these events more detailed by applying the IZMIRAN model of the field-aligned currents distribution, the OVATION model of the auroral oval location and the electron image of IMAGE satellite.

Observations

Figure 1 presents IMF *Bz* and *By* components (high resolution OMNI database http://omniweb.gsfc.nasa.gov) and magnetograms of high-latitude of stations of Scandinavian magnetometer chain IMAGE (http://www.ava.fmi.fi/MIRACLE/) for storms 24 Nov 2001(a), and 30 May 2003(b). The strong dayside magnetic bays at polar latitudes are seen in both events.

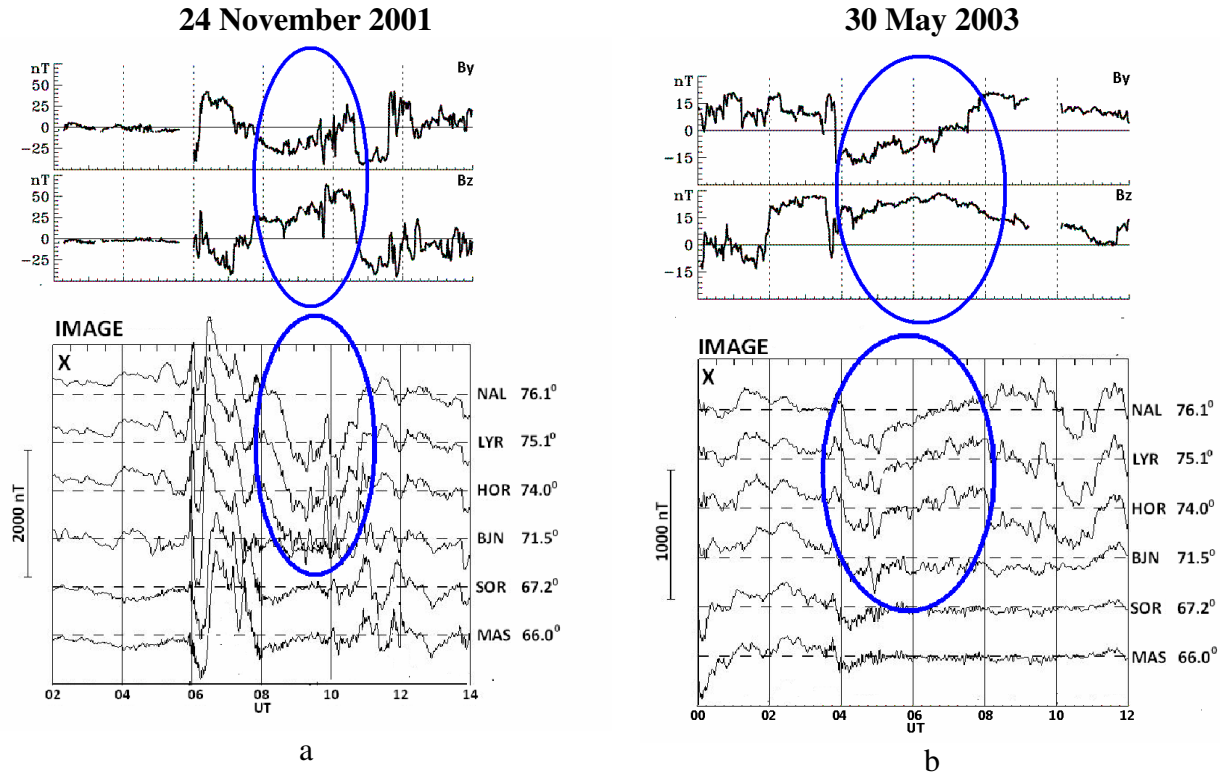

Fig.1. The IMF By, Bz components and IMAGE magnetograms for storms (a) 24 Nov 2001, and (b) 30 May 2003.

Discussion

The magnetic variation vectors of high-latitude IMAGE stations (NAL – LUR) were constructed using difference magnetograms based on magneto-quiet 2009 level [Levitin et al., 2014]. They are shown in Fig. 2a (left) for 02-14 UT on 24 Nov 2001 and Fig2. b (left) for 00 – 12 UT on 30 May 2003. It is well known, that the ionospheric currents, observed on the Earth's surface as geomagnetic variations and substorms, are closely related to the field-aligned electric currents (FAC) in the magnetosphere. The right panels of Fig.2a,b present the FAC distribution during these dayside polar substorms, calculated by the IZMIRAN model [Feldstain and Levitin, 1986] in the coordinates: geomagnetic latitude – MLT: red color indicates downward currents, blue – upward ones. The vortex with clockwise rotation direction corresponds to downward FAC.

The FAC intensification is seen in the dayside polar region where the Scandinavian polar latitude stations were mapped. We interpret this FAC as the NBZ system [Iijima and Shibaji, 1987]. For event of 30 May 2003, the vortices with opposite rotation direction could be a results of the upward and downward FAC.

Figure 3 shows the electron image from the IMAGE satellite (http://cdaweb.gsfc.nasa.gov/cgi-bin/eval3.cgi) 24 November 2001 (a); the CHAMP magnetic field data (http://op.gfz-potsdam.de/champ), and the auroral oval location according to OVATION model (http://sd_www.jhuapl.edu/Aurora/ovation/ovation_display.html)) for 30 May 2003 (b). It is seen that Scandinavian high-latitude stations are located into the dayside auroral oval, i.e. into the closed magnetosphere. During the CHAMP satellite passage (at~06.50 UT, and ~ 08.30 UT) demonstrated the FAC enhancement, the precipitating ions and electron with typical magnetospheric spectra were seen by DMSP satellite under these Scandinavian high-latitude stations (do not show here) supporting their mapping into the closed magnetosphere.

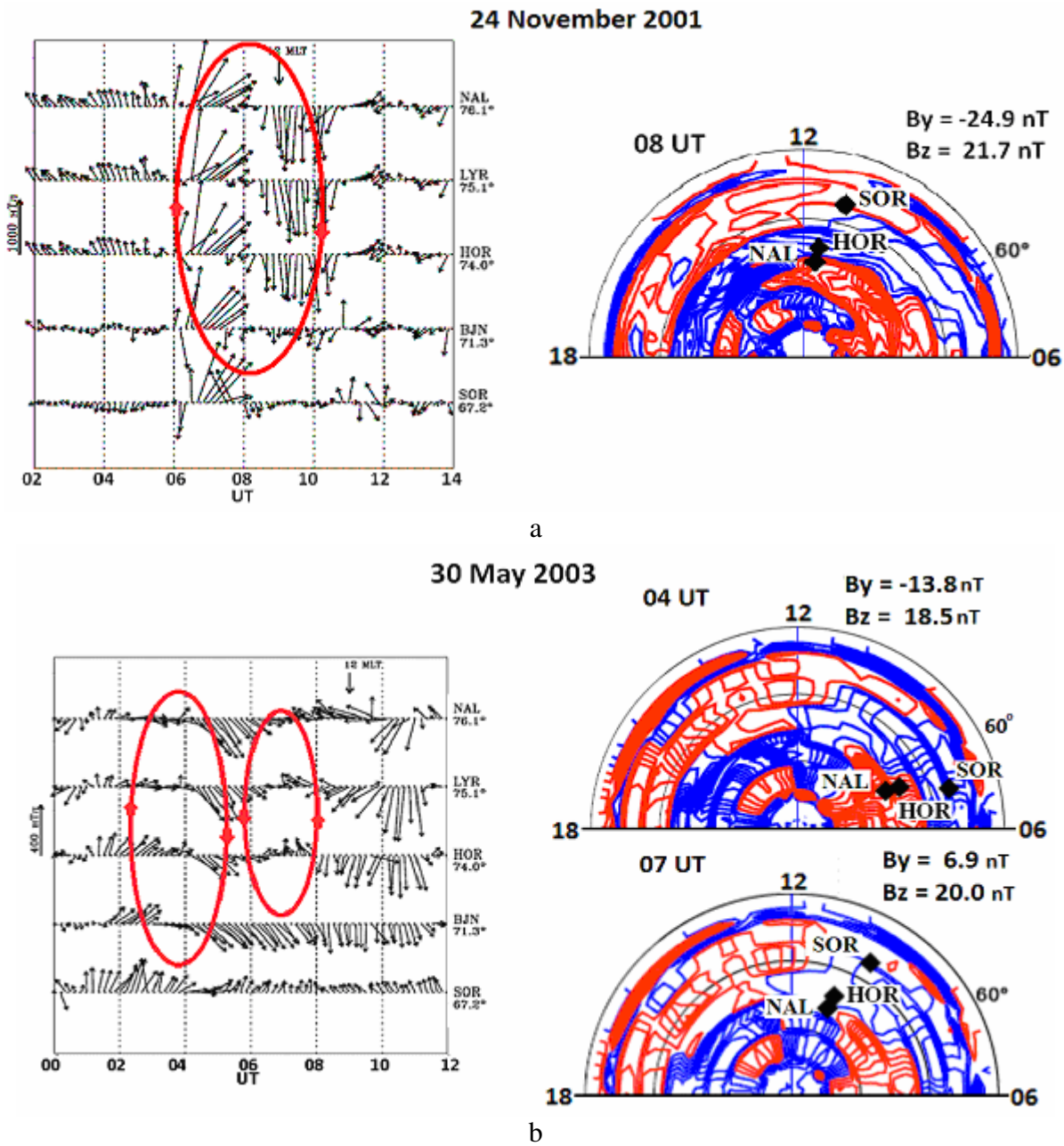

Fig. 2. The magnetic variation vectors (left) and the field aligned currents (FAC) distribution according IZMIRAN model in coordinates geomagnetic latitude – MLT: red - downward currents, blow – upward ones(right) for storms (a) 24 Nov 2001, and (b) 30 May 2003.

Summary

1. We found that the daytime polar substorms development is the magnetosphere respond to the high positive values of the IMF Bz occurrence during the magnetic storms.
2. We suppose that the daytime polar substorms under consideration could be mapped inside the closed magnetosphere at poleward part of the plasma ring surrounding the Earth.
3. The daytime polar substorms were observed at the latitude region where the NBZ system of the field aligned currents (FAC) are enhanced. However, that is a paradox, because now it is generally accepted that the NBZ current system is located into the polar cap, not into the closed magnetosphere. The question arises: how the considered dayside polar substorms are related to the NBZ currents?

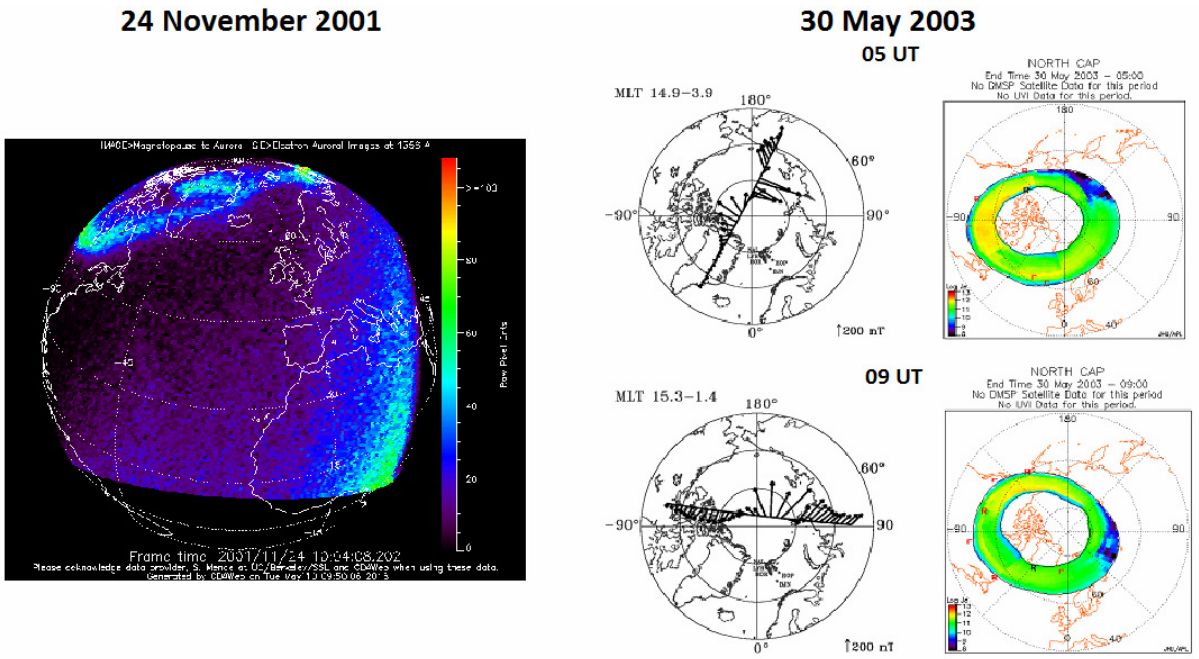

a b

Fig. 3. (a) Electron image of IMAGE satellite for 24 Nov 2001, 10 UT, and (b) the CHAMP magnetic field data and auroral oval location for 05UT and 09UT, 30 May 2003.

Acknowledgements.

The paper was supported by the Program No 7 and No 18 of the Presidium of the Russian Academy of Sciences (RAS).

References

Feldstein Ya.I., and Levitin A.E. Solar wind control of electric fields and currents in the ionosphere J. Geomag.Geoelectr., 38, 1143–1182, 1986.

Iijima T.,and Shibaji T. Global characteristics of northward IMF-associated (NBZ) field-aligned currents // J. Geophys. Res., 92(A3), 2408-2424, 1987.

Kleimenova, N.G., Gromova, L.I., Dremukhina, L.A., Levitin, A.E., Zelinskii, N.R., and Gromov, S.V. High_latitude geomagnetic effects of the main phase of the geomagnetic storm of November 24, 2001 with the northern direction of IMF, Geomagn. Aeron. (Engl. Transl.), 55, (2), 174–184, 2015.

Levitin, A.E., Gromova, L.I., Gromov, S.V., and Dremukhina, L.A., Quantitative estimation of local geomagnetic activity relative to the level of the magnetically quiet period in 2009, Geomagn. Aeron. (Engl.Transl.), 54(3), 292–299, 2014

Levitin, A.E., N.G. Kleimenova, L.I. Gromova, E.E. Antonova, L.A. Dremukhina, N.R. Zelinsky, S.V. Gromov, and L.M. Malysheva, Geomagnetic disturbances and pulsations as a high_latitude response to considerable alternating IMF variations during the magnetic storm recovery phase(Case Study: May 30, 2003), Geomagn. Aeron. (Engl. Transl), 55(6), 755–768, 2015.

Proceedings of
Eighth Workshop "Solar Influences on the Magnetosphere, Ionosphere and Atmosphere"
Sunny Beach, Bulgaria, May 30 - June 3, 2016

Fluctuations of GPS Signals and Auroral Activity During 17 March 2015 Geomagnetic Storm

Shagimuratov I. I. [1], *Chernouss S. A.* [2], *Filatov M. V.* [2], *Efishov I. I.* [1], *Despirak I. V.* [2] *Kopytenko Yu.A.* [3]

[1] WD IZMIRAN, Kaliningrad, Russia;
[2] Polar Geophysical Institute, Apatity, Russia;
[3] St.-Petersburg Department of IZMIRAN, St.-Petersburg, Russia.
E-mail: shagimuratov@mail.ru

Abstract

In this report we analysed space whether conditions during strong of 17 Mach 2015 geomagnetic storm. Dual-frequency GPS measurements for individual satellite passes served as raw data. The rate of TEC (ROT) was used as a measure of fluctuation activity, the data of GPS stations spaced in latitudinal range 67-50°N over longitude of 20°E were involved in this investigation. The magnetograms of the IMAGE networks were used as indicator of auroral activity. Strong geomagnetic field variations took place after noon at auroral IMAGE network during 17 March 2015. The network includes the stations located in auroral, subauroral and mid-latitude area. Maximal intensity of the substorm activity took place at auroral zone. It was found a good similarity between temporary development of substorm activity and intensity of TEC fluctuations of GPS signals. The intensity of the magnetic bay and TEC fluctuations decreased from north to south. Averaged images of spatial distribution of TEC fluctuations (index ROTI) based on the daily GPS measurements from 130-150 selected stations, were constructed in CGL (Corrected Geomagnetic Latitude) and Magnetic Local Time (MLT) coordinates. These images demonstrate the irregularities oval which is similar to the auroral oval. Auroral and irregularity ovals moved to equator and reached latitudes of 50-55°N during this storm. High latitude phase fluctuations of GPS signals are very sensitive to change of auroral activity and can be used as indicator of space weather conditions.

Introduction

The fluctuations of GPS signals are appeared due to irregularities with different scales which present in the polar ionosphere. Ionospheric irregularities can be structured with latitude and their intensity differ in the high-latitude ionosphere at subauroral, auroral, polar and cusp regions. In accordance with this, the fluctuation activity varies considerably with latitude and space weather's conditions.

The world wide and numerous network of GPS stations are very opportunely to monitor the spatial distribution of ionospheric irregularities in planetary scale [1, 2].

During auroral activity intensity of fluctuations GPS signals essentially increase. The experimental evidence of positioning errors connected with spatial and temporal variations in the intensity of auroral arcs was demonstrated in [3, 4, 5].

Strong total electron content fluctuations can complicate phase ambiguity resolution, increase the number of undetected and uncorrected cycle slips and loss of signal lock in GPS navigation and positioning errors [6].

The low frequency GPS phase fluctuations may be directly due to electron density changes along the radio ray path, or the total electron content (TEC) changes.

In this report GPS measurements of global IGS network were used to study the storm time occurrence of phase fluctuations (TEC changes) in the high latitude ionosphere during 17 March 2015 storm and data about loss of GPS signal lock during this event.

Data and Geomagnetic Condition

The TEC measurements for individual satellite passes served as raw data. As a measure of fluctuations activity the rate of TEC (ROT), in the unit of TECU/min (1 TECU=10^{16} electron/m^2) at 1 min interval was used. As a measure intensity fluctuations index ROTI was used. During active phase of storm we used magnetometer data of chain of the Scandinavian network.

The strong storm started after 03 UT of 17 March 2015. On the Figure 1 the geomagnetic conditions for this event presented.

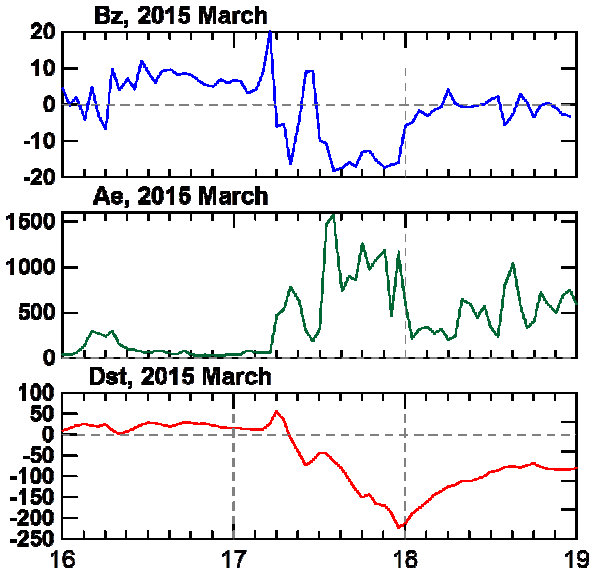

Fig.1. BZ, Ae and Dst variations for 16-19 March 2015.

Observations

The temporal occurrence of the TEC fluctuations is clearly observed in time variations of the dual frequency carrier phase along satellite passes. For example, the TEC variations observed at auroral KIR0 (67.5°N, 21.0°E) and midlatitude BOGO (53.2°N, 21.0°E) stations for quiet and disturbed conditions are presented at Figure 2. It will be noted that the BOGO was the lowest latitudinal station at which was found out evident the occurrence TEC fluctuations during the discussed event.

The picture demonstrates the rate of TEC changes (ROT) along all satellite passes over 24-hour interval. At KIR0 stations for quiet day the fluctuations were very weak and registered near local midnight. During geomagnetic disturbed day the moderate intensity of fluctuations was detected on interval 07-09 UT while AE rapid increase to about 750 nT, at the same time B_Z was short duration negative.

After 12 UT B_Z long time persisted negative. During this time strong TEC fluctuations were observed at all satellite passes. It is evidence that KIR0 station all the time was within auroral oval. The lowest latitudes station on which was detected weak fluctuations is midlatitude BOGO station.

In Figure 3 the variations of ROT at stations located different latitudes from north to south are presented.

The detected TEC fluctuations at BOGO during storm day was localized at latitudes 52-53°N when strong magnetic bays were registered on magnetogram of the Scandinavian network near 17 UT (Fig.4.).

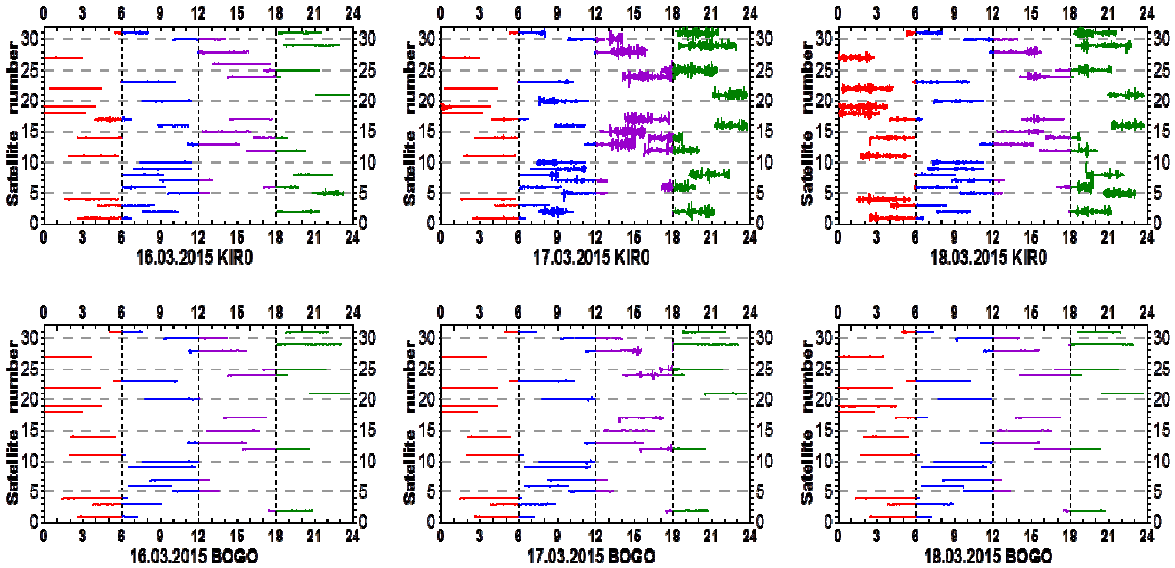

Fig.2. Development of TEC fluctuations at midlatitude BOGO and KIR0 stations for quiet (16 March), storm (17 March) and recovery phase (18 March) days.

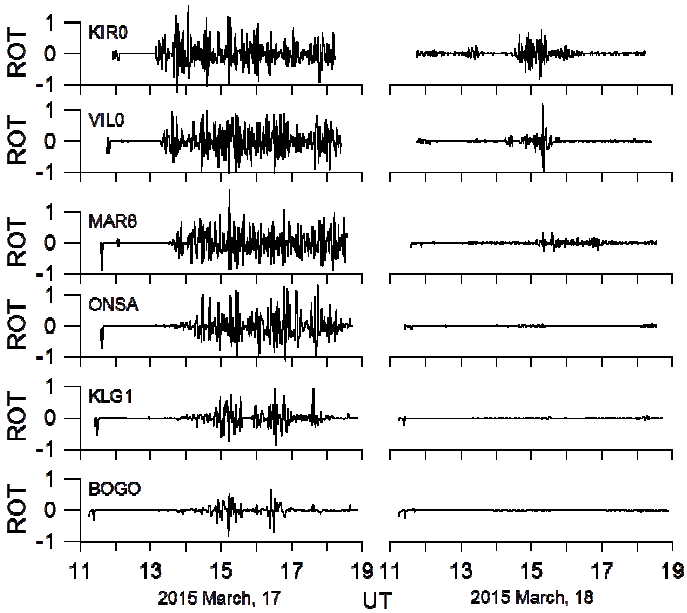

Fig.3. Latitudinal occurrence of TEC fluctuations.

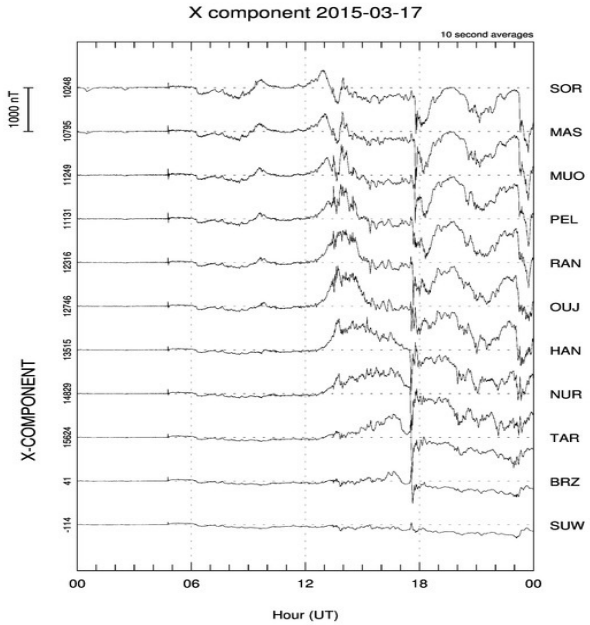

Fig.4. The variations of the geomagnetic field X-component at different stations.

The network includes the stations located in auroral, subauroral and mid-latitude area.

The magnetic activity developed after 12 UT. The intensity of the magnetic bay decrease from north to south. The strongest magnetic variations were registered at 17-19 UT, when a weak bay was observed even at a latitude of 55 N. Obviously that time course of ROT coincides with the variations of the X-component of the geomagnetic field. According to evidence of the maximum TEC variations as well as the pulsations of the geomagnetic field we can determine the source which cause a disruptions of the navigation signal in the ionosphere during auroral disturbances. This is particularly noticeable in the intervals of the substorm intensification.

Latidudinal and Temporal Occurrence Intensity of TEC

As a measure of the intensity of fluctuation activity the Rate of TEC Index (ROTI) based on standard deviation of ROT was used. Index ROTI was estimated in 10-minute interval. For spatial and temporal distribution TEC fluctuations to obtain it was formed images ROTI in Corrected Geomagnetic Latitude (CGL) and UT time coordinates (Fig. 5). Stations were chosen in according their location relative to auroral oval. As seen in Figure 5 intensity fluctuations decrease with latitude. The time span intensity fluctuations also decrease with latitudes. The maximal TEC fluctuations developed during auroral activity.

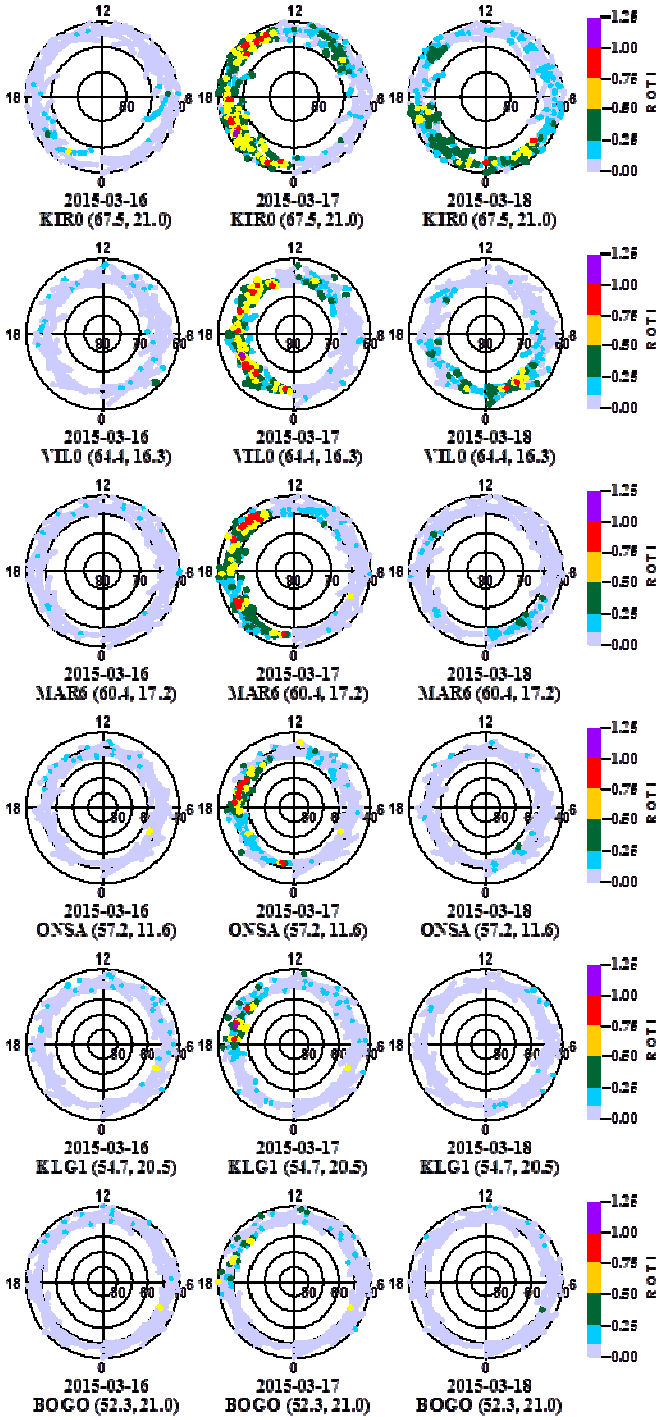

Fig.5. Intensity TEC fluctuations at different stations (coordinates: geomagnetic latitude-UT time).

Influence Auroral Activity on Disturbances of Navigation Signals

Severe fluctuation of GPS signals increase the number of undetected and uncorrected cycle slips and loss of signal lock in GPS navigation [7]. We analyzed occurrence disturbance navigation signals for the discussed storm in the auroral ionosphere. In Tab. 1 are presented number cycle sleeps and loss lock L_1 or L_2 signals at several GPS stations located in auroral zone. The cycle sleeps we evaluated using LL indicator in RINEX files. The number loss lock is calculated as lack of L_1 or L_2 indication in the observation files for quiet day of 16 March (green) and disturbed of 17 and 18 March days (red).

Table 1.

Latitude range	*Date of March-2015*	*Numbers of slips*			*%*		
		LL Indic.	loss lock L_1 or L_2	sum	LL Indic.	loss lock L1 or L2	sum
60°-65° N	16	36	66	102	0.124	0.226	0.35
	17	108	178	286	0.371	0.609	0.981
	18	87	140	227	0.297	0.482	0.779
65°-70° N	16	71	50	121	0.239	0.17	0.409
	17	124	109	233	0.42	0.368	0.788
	18	126	114	240	0.429	0.386	0.815

Table is demonstrated that during geomagnetic storm the disturbances navigation signals essentially increase against quiet day.

Conclusions

During 17 March 2015 geomagnetic storm the intensive TEC fluctuations were observed at auroral and subauroral ionosphere. Joint analysis of observed phase fluctuations of GPS signals, and fluctuations of the geomagnetic field showed good agreement of both events during auroral activity. In time the maximal activity aurora the intensive phase fluctuations were registered even at midlatitude. This fact confirms the expansion of the auroral oval towards the equator.

Acknowlegments

We thank the Institutes who maintain the IMAGE Magnetometer Array. This study was supported by Grant of RFBR 14-05-98820 r-sever-a and partly Program No 7 of the Presidium of the RAS.

References

[1] I. I. Shagimuratov, A. Krankowski, I. I. Efishov, et al. High latitude TEC fluctuations and irregularity oval during geomagnetic storms. Earth Planets Space, vol. 64(6), 2012, pp. 521-529.

[2] P. Prikryl, P. T. Jayachandran, R. Cyadwic, and T. D. Kelly. Climatalogy of GPS phase scintillation at northern high latitudes for the period from 2008 to 2013. Ann. Geophys., vol. 33, 2015, pp. 531-545.

[3] A. M. Smith, C. N. Mitchell, R. J. Watson, R. W. Meggs, P. M. Kintner, K. Kauristie, and F. Honary. GPS scintillation in the high arctic associated with an auroral arc. Space Weather, vol. 6, 2008, S03D016.

[4] S. A. Chernouss, N. V. Kalitenkov. The dependence of GPS positioning deviation on auroral activity. International Journal of Remote Sensing, vol. 32(1), 2011, pp. 3005-3017.

[5] S. A. Chernous, M. V. Shvets, M. V. Filatov, I. I. Shagimuratov, and N. V. Kalitenkov. Studying Navigation Signal Singularities during Auroral Disturbances. Russian Journal of Physical Chemistry B, vol. 9(5), 2015, pp. 778–784.

[6] K. Oksavik, C. van der Meeren, D. A. Lorentzen, L. J. Baddeley, and J. Moen. Scintillationand loss of signal lock from poleward moving forms in the cusp ionosphere. JGR: Space Physics, vol. 120, 2015, pp. 9161-9175. doi:10.1002/2015JA021528.

[7] P. Prikryl, P. T. Jayachandran, S. C. Mushini, D. Pokhotelov, J. W. MacDougall, E. Donovan, E. Spanswick, and J.-P. St.-Maurice. GPS TEC scintillation and cycle slips observed at high latitudes during solar minimum. Ann. Geophys., 2010, 28, pp. 1307-1316.

Proceedings of
Eighth Workshop "Solar Influences on the Magnetosphere, Ionosphere and Atmosphere"
Sunny Beach, Bulgaria, May 30 - June 3, 2016

Auroral, Geomagnetic and Ionospheric Disturbances during St. Patrick's Day Geomagnetic Storms in 2013 and 2015

Klimenko M.[1,2], Klimenko V.[1], Despirak I. [3], Ratovsky K.[4], Zakharenkova I.[1], Korenkova N.[1], Kozelov B. [3], Gomonov A. [3], Vasiliev E. [3], Chernyakov S. [3],

[1] West Department of Pushkov IZMIRAN, RAS, Kaliningrad, Russia;
[2] Immanuel Kant Baltic Federal University, Kaliningrad, Russia;
[3] Polar Geophysical Institute, Apatity, Russia;
[4] Institute of Solar-Terrestrial Physics, SB RAS, Irkutsk, Russia
E-mail: maksim.klimenko@mail.ru

Abstract

This study presents an analysis of the satellite-borne and ground-based observations of the geomagnetic disturbances and ionospheric electron density distribution during two St. Patrick's Day geomagnetic storms on March 17, 2013 and 2015. The first event on March 17, 2015 is the principal event covering the interval from 15 to 18 March 2015, in which solar eruptive phenomena (a long-enduring C9-class solar flare and associated CME(s) on 15 March) and a strong geomagnetic storm on 16–18 March (max. Dst was –228 nT) were reported. This magnetic storm was the largest one observed in the current solar cycle. The second event is the period on 17–18 March 2013 which was strong geomagnetic storm (the Dst index ~ –140 nT) developed. This storm was caused by magnetic cloud in the solar wind. Solar wind and interplanetary magnetic field parameters were taken from OMNI data base. The magnetograms of the IMAGE network and Observations of the Multiscale Aurora Imaging Network (MAIN) in Apatity were used as indicator of auroral activity. Both of these storms characterized by the same moment of storm sudden commencement (SSC), but 2015 geomagnetic storm had much greater magnetospheric input into thermosphere-ionosphere system. We paid the particular attention to the ionospheric disturbances during the main and recovery phase of geomagnetic storms. The Global Self-consistent Model of the Thermosphere, Ionosphere and Protonosphere (GSM TIP) allows us to reveal the main processes that influence on the behavior of the total electron content and the F2 layer peak electron density during these storm events.

Introduction

Geomagnetic storms launch several physical processes in magnetosphere-ionosphere system resulting in positive and negative ionospheric storms, which are related to plasma transport, recombination and direct ionization by magnetospheric energetic electrons. Negative ionospheric storm effects have mostly been related to neutral composition changes [1], the equatorward migration of the mid latitude electron density trough from high to low latitudes [2]. The generally accepted mechanisms of positive ionospheric storm are based on plasma transport by electric fields, neutral winds and the plasmasphere source. Numerical simulations of ionospheric storms showed dominance of electrodynamic mechanisms and neutral winds in positive effects at low latitudes and neutral winds over chemical composition changes at middle latitudes e.g., [3–5]. The negative and positive ionospheric storms would be briefly discussed in this paper.

Ionosphere's *F* region disturbances during a storm recovery phase are one of the most unexamined issues on the topic of the ionosphere's response to a geomagnetic storm. This issue is broadly discussed only in recent years [6–8]. The problem is very important in terms of understanding of the interrelated processes in the upper atmosphere and the key in the background values selection to study the ionospheric disturbances effects of different origin. Therefore it is necessary to carry out a research on the formation mechanisms of the ionospheric disturbances and to clarify the effects of the neutral composition changes and

ionosphere-plasmasphere connections on the formation of the ionospheric effects during the recovery phase of a geomagnetic storm. This study presents the general features and interpretations of the observed ionospheric disturbances during main and recovery phase of the geomagnetic storms on March 17–23, 2013 and 2015. In Figure 1 some solar wind and IMF parameters, the AE, SYMN/H and Kp indicies for the period 15–23 March 2015 and 2013 are presented.

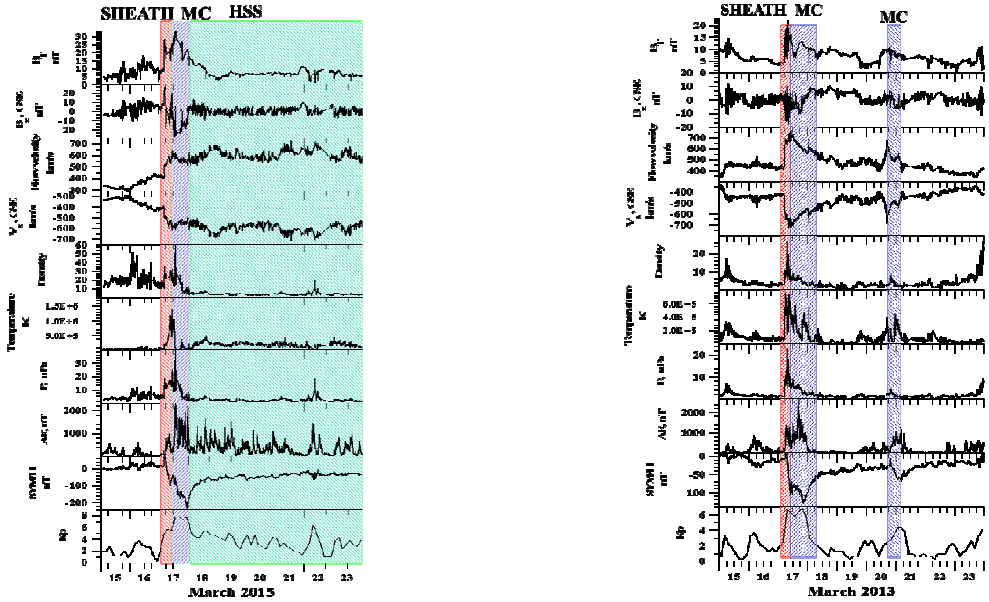

Figure. 1. The solar wind conditions taken from the OMNI database for the period 15–23 March 2015 (left panel) and 2013 (right panel). There some solar wind and IMF parameters, the AE, SYMN/H and Kp indicies are presented. The solar wind magnetic cloud (MC), SHEATH and the high speed stream (HSS) regions are shown by shaded blue, red and green rectangles.

ObservationS AND brief GSM TIP model description

When studying the processes occurring in the ionosphere, a combination of the multiinstrumental data set and physical theoretical model is the most effective approach, which gives the opportunity to identify the mechanisms of changes in the ionospheric parameters during geomagnetic storms. We calculated the ionospheric parameters during two St. Patrick's storm events using the first principles Global Self-consistent Model of the Thermosphere, Ionosphere, and Protonosphere (GSM TIP) developed in West Department of Pushkov Institute of Terrestrial Magnetism, Ionosphere, and Radio Wave Propagation, Russian Academy of Sciences (WD IZMIRAN) [9, 10]. The model calculates time-dependent global three-dimensional distributions of temperature, composition and velocity vectors of neutral gas; the density, temperature, and velocity vectors of atomic and molecular ions and electrons; and two-dimensional distribution of electric potential, both of a dynamo and magnetospheric origin. Klimenko et al. [10] have modified the calculation of electric fields of dynamo and magnetospheric origin. Previous studies have shown the importance of taking into account the variations in the R2 FACs at the model description of ionospheric effects of geomagnetic storms and their role in the formation of the main ionospheric trough, auroral and equatorial electrojets. Modified in the last few years GSM TIP model uses the most modern empirical models of the auroral electron precipitations. It has already been used to study the ionospheric dynamics during geomagnetic storms from 2000 up to 2011, and the following most important results were obtained: (1) it was explained the *F3* layer formation mechanism and multi-layer structure in the equatorial *F* region during geomagnetic storms [5, 8], (2) it was correctly revealed the ionospheric effects of the disturbance dynamo electric field, the prompt penetration magnetospheric convection electric field to the middle and low

latitudes and overshielding effects [11], (3) for the first time it was found that the positive electron density disturbances in the mid-latitude *F* region are formed in the daytime during the geomagnetic storm recovery phase due to an increase in O/N_2 ratio [8]. In the present paper we used the same statement of the problem as in [5] for interpretation of the observed ionospheric disturbances during main and recovery phase of the geomagnetic storms on March 17–23 2015 and 2013. The description quality of the ionospheric effects in GSM TIP model will be tested by comparison of the obtained calculation results with observations.

The DPS-4 Digisondes over Irkutsk, Russia (52.2°N, 104.2°E; geomagnetic coordinates 40.9°, 175.1°) were used as a data source for *F*2 layer peak electron density. All Digisonde ionogram data has been manually scaled using an interactive ionogram scaling software, SAO Explorer [12]. In the case of the ionosonde data we use the monthly median diurnal variation as a quiet-time reference (quiet day).

For an estimation of spatial scales and temporal dynamics of ionospheric response to St. Patrick geomagnetic storm events the global *GPS TEC* maps have been created. As a source of vertical *TEC* data we used IGS (the International GNSS (Global Navigation System Service) Service) Global Ionospheric Maps (GIMs) of *TEC* in the IONEX (IONosphere map EXchange) format. These data are accessible at the ftp server: ftp://cddis.gsfc.nasa.gov/pub/gps/products/ionex. The GIMs are generated routinely by the IGS community with resolution of 5° longitude and 2.5° latitude and temporal interval of 2 hours; one *TEC* unit (TECU) is equal to 10^{16} electrons/m^2. Detailed description of IGS GIMs computation and validation can be found in [13]. In this study, the final product of IGS combined GIMs produced by GRL/UWM were used to calculate the global maps of monthly median of GPS *TEC* values.

In this study we also use electron concentrations measured in the D- and E- region by ground-based method of the partial reflection technique, using the 2.60–2.72 MHz radar in Tumanny, near Murmansk in Russia, at 69.0° N, 35.7° E. Recording of scattered signals was conducted in the daytime in the altitude range of 60-130 km, nearly permanently. The amplitudes of the ordinary and extraordinary components of the signal were averaged on a minute time scale at all the heights considered. From these data N(h)-profile was calculated by using radiowave differential absorption technique. We use 1-min time-averages from radar, with height resolution of 1.5 km.

Results and Discussion

The geomagnetic storm occurred on 17–19 March 2015 was the record in strength over the past ten years. It was the strongest storm in the 24^{th} solar cycle. It was the result of a pair of CME's which left the Sun on 15 March 2015, may be unexpectedly combined spreading towards Earth and formed a large shock front crossing the Earth orbit. In 4:45 UT a geomagnetic sudden impulse was registered at all stations of the IMAGE magnetometers network which indicated that the shock wave formed by the CME swept past our planet. It coincides with the storm sudden commencement when SYM/H index jumped from 16 to 66 nT. A magnetic cloud passed the Earth and just after it a HSS superposed and contributed to the storm duration. Dst index reached the value –228 nT in 22:47 UT on 17 March 2015. On 17.03.2013 a geomagnetic storm developed during this time. The Dst index reached ~ –140 nT. On 20.03.2013 a second magnetic cloud passed by the Earth, and a second geomagnetic storm with Dst ~ –65 nT developed.

In the first event, 17–20 March 2015, 8 substorms were identified by the all-sky camera in Apatity: two of them occurred during the main storm phase, one – in the vicinity of the SYM/H peak, on 17 March 2015, five – in the recovery phase and in the late recovery phase of the storm, on 18 and 20 March 2015. Below was presented one example of substorm observations – substorm event during the storm main phase, in 17: 36 UT on 17 March 2015.

In Figure 2 the substorm in 17:36 on 17 March 2015 by measurements from MAIN in Apatity is presented. The top panel shows selected images of the all-sky camera, and the bottom panel – the keograms by the all-sky camera (to the left) and by the Guppy (GC) camera (to the right). The substorm was observed during the main phase of the severe geomagnetic storm on 17 March 2015. The SYM/H value at the moment of substorm onset was ~ –163 nT. As seen in Figure 2 substorm auroras appeared in the South part of the field of view in 17:36:40 UT. For some minutes auroras stayed in the South part of the field of view. In 17:42 UT a fast motion towards North was observed and in 17:45:30 UT the auroras occupied the whole field of view. In the GC keogram, the substorm auroras are seen from 17:42:30 UT at the South part of the field of view, at 35° from zenith, due to the fast movement to North. Then a maximal intensity of 200 rel. units was observed about 17:46:25 UT.

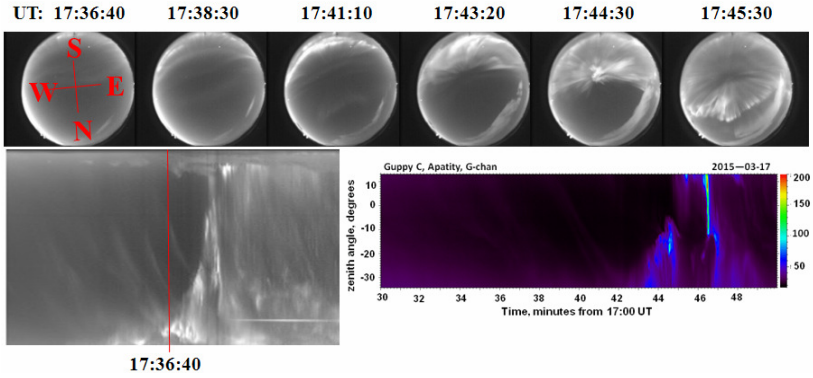

Figure. 2. Development of the substorm on 17 March 2015 in 17:36:40 by chosen all-sky images (top panel), by all-sky keogram (left bottom panel) and Guppy (GC) camera keograms (right bottom panels). The world directions are marked in the first image, the universal time is written above each image.

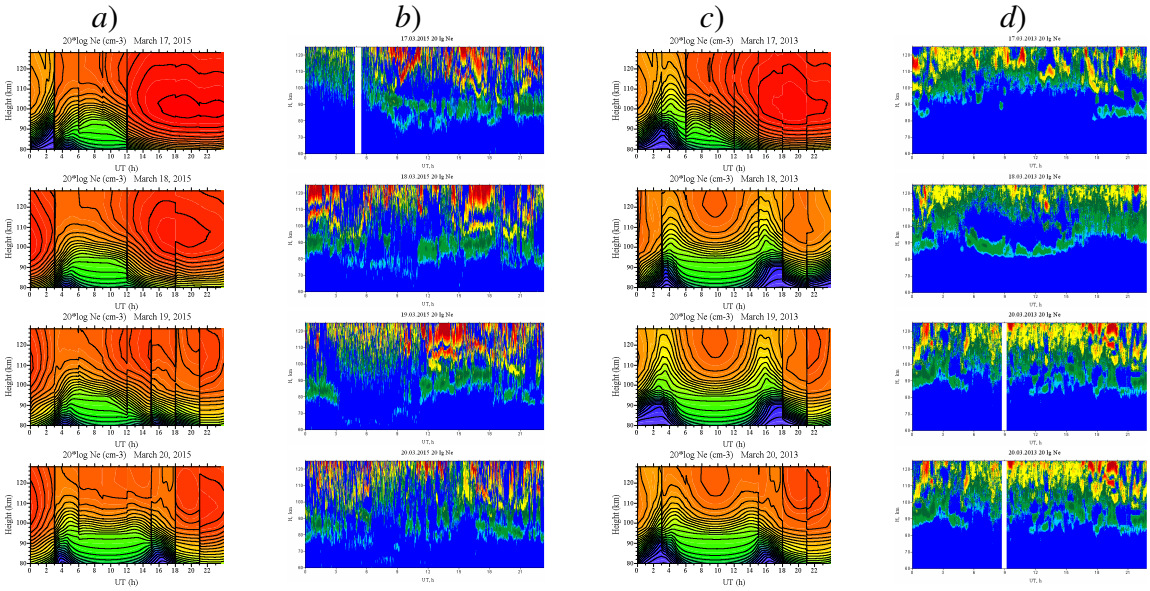

Figure 3. Diurnal variation in vertical profile of 20lg(N_e) in Tumanny in March 17, 18, 19, and 20 (from the top to bottom). Panel a) shows the GSM TIP model results for March, 2015; panel b) shows the radar observations for March, 2015; panel c) shows the GSM TIP model results for March, 2013, and panel d) shows the radar observations for March, 2013.

Figure 3 shows the model and the observed temporal development of the electron density vertical profiles (from 60 up to 120 km) above the Tumanny during the period 17–20 March

2015 and 2013. One can see the qualitative and quantitative agreement between the calculation results and observations. This confirms the correctness not only the GSM TIP model, but also the used models and empirical relationships of the potential difference and R2 FACs, which adequately describe the changes in these parameters during geomagnetic storms. It is evident that during the main phase of a geomagnetic storm the greatest increase in the electron density in the ionosphere E region at heights of 110 km occurs that is the cause of auroral precipitation strengthening by increasing substorm activity in this period.

Figure 4 shows the behavior of the critical frequency of the ionosphere *F*2 layer peak, *foF*2, above the ionospheric stations Irkutsk and Kaliningrad during March 17–23, 2015 and 2013, according to the GSM TIP model calculation results and digital ionosonde data. As a reference values of the ionospheric parameters we chose the daily variations for March 15, 2015 and 2013, when the geomagnetic activity was low. The first storm on 2015, which began at 03:00 UT on March 17, caused a negative *foF*2 disturbances in Irkutsk in the morning and did not lead to the noticeable effects in Kaliningrad at night. The second phase of the storm was stronger and long-lasting one, it began at 12:00 UT. At the initial stage of its development it led to the formation of the positive ionospheric disturbances over Kaliningrad in the afternoon and in the evening over Irkutsk. The same positive ionospheric storm appears for 2013 St. Patrick storm event. An important feature of the ionosphere behavior above stations Irkutsk and Kaliningrad in the recovery phase of a geomagnetic storm on March 21–23, 2015 is the appearance of the positive daily disturbances in *foF*2. At night, on the same days over Kaliningrad the negative disturbances are observed that practically are absent over Irkutsk. On the recovery storm phase for 2013 storm event it is evident the occurrence of negative *foF*2 disturbances. Such differences between two storm events associated with the intensity of two storms and with different scenario of storm recovery phase. The comparison of storm-time ionospheric disturbances obtained in model results with GPS TEC globally shows a good agreement. Fig.5 presents one example of this model/data comparison.

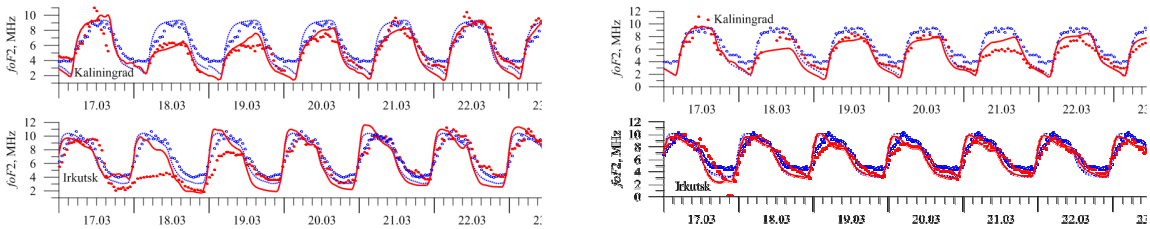

Figure 4. foF2 variations over Kaliningrad and Irkutsk according to the ionosonde data (circles) and model-derived results (lines) on March 17–23 (red color) comparing with the quiet geomagnetic conditions (blue color). Results for 2015 are presented at the left panel and for 2013 storm at the right panel.

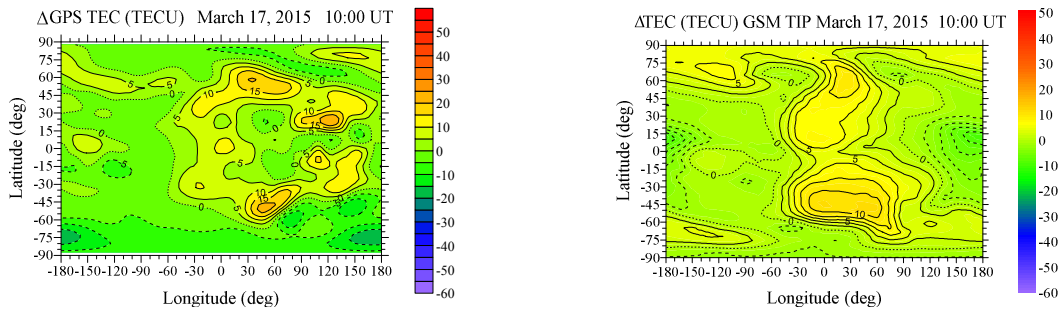

Figure 5. Global maps of TEC disturbances during geomagnetic storm on March 17, 2015 at 10:00 UT, obtained according to the GPS data (left) and model calculation results (right).

Conclusions

We reveal the following features of the *foF*2 ionospheric disturbances during geomagnetic storms on March 17–23, 2013 and 2015: (1) on the recovery phase of the strong geomagnetic storm on March 17–23, 2015 over Irkutsk and Kaliningrad geomagnetic storms leads to the daytime positive and nighttime negative *foF*2 disturbances; (2) GSM TIP model results agree with electron density disturbances at lower ionosphere during two storm events. Formation of the positive *foF*2 disturbances during the 17–23 March, 2015 storm recovery phase in the daytime *F* region of the mid-latitude ionosphere is due to the increase in $n(O)/n(N_2)$ [8]. At night, in spite of the decrease in $n(N_2)$, the negative effects in *foF*2 are formed due to under-filling of the plasma tubes as a result of their depletion during the main phase of the geomagnetic storm.

Acknowledgments. These investigations were performed with financial support of the Russian Foundation for Basic Research Grant No. 15-35-20364. The paper was partly supported by the Program No. 7 of the Presidium of the Russian Academy of Sciences (RAS).

References

[1] Mayer H.G., Harris I., and Spencer N.W. Some properties of upper atmosphere dynamics // Rev. Geophys. – 1978. – V. 16. – P. 539–565. – doi:10.1029/ RG016i004p00539.

[2] Mendillo M., Klobuchar J.A., and Hajeb-Hosseinieh H. Ionosphere disturbances: Evidence for the contraction of the plasmasphere during severe geomagnetic storms // Planet. Space Sci. – 1974. – V. 22. – 223–-236. – doi: 10.1016/0032-0633(74)90026-9.

[3] Bauske R., and Prolss G.W. Modeling the ionospheric response totraveling atmospheric disturbances // J. Geophys. Res. – 1997. – V. 102. – P. 14,555

[4] Balan N., Shiokawa K., Otsuka Y., et al. A physical mechanism of positive ionospheric storms at low latitudes and midlatitudes // J. Geophys. Res. – 2010. – V. 115. – A02304. – doi:10.1029/2009JA014515.

[5] Klimenko M.V., Klimenko V.V., Ratovsky K.G., et al. Numerical modeling of ionospheric effects in the middle- and low-latitude F region during geomagnetic storm sequence of 9–14 September 2005 // Radio Sci. – 2011. – V. 46. – No. 3. – RS0D03. – doi:10.1029/2010RS004590.

[6] Balan N., Otsuka Y., Nishioka M., et al. Physical mechanisms of the ionospheric storms at equatorial and higher latitudes during the recovery phase of geomagnetic storms // J. Geophys. Res. – 2013. – V. 118. – P. 2660–2669. – doi:10.1002/jgra.50275.

[7] Suvorova A.V., Dmitriev A.V., Tsai L.-C., et al. TEC evidence for near-equatorial energy deposition by 30 keV electrons in the topside ionosphere // J. Geophys. Res. – 2013. – V. 118. – P. 4672–4695. – doi: 10.1002/jgra.50439.

[8] Klimenko M.V., Klimenko V.V., Bessarab F.S., et al. Influence of geomagnetic storms of September 26–30, 2011, on the ionosphere and HF radiowave propagation. I. Ionospheric effects // Geomagn. Aeron. – 2015. – V. 55. – No. 6. – P. 744–762.

[9] Korenkov Yu.N., Klimenko V.V., Förster M., et al. Calculated and observed ionospheric parameters for a Magion-2 passage and EISCAT data on July 31, 1990 // J. Geophys. Res. – 1998. – V. 103. – No. A7. – P. 14697–14710.

[10] Klimenko M.V., Klimenko V.V., Bryukhanov V.V. Numerical simulation of the electric field and zonal current in the Earth's ionosphere: The dynamo field and equatorial electrojet // Geomagn. Aeron. – 2006. – V. 46. – No. 4. – P. 457–466. – doi:10.1134/S0016793206040074.

[11] Klimenko M.V., Klimenko V.V. Disturbance dynamo, prompt penetration electric field and overshielding in the Earth's ionosphere during geomagnetic storm // J. Atmos. Solar-Terr. Phys. – 2012. – V. 90–91. – P. 146–155. – doi:10.1016/j.jastp.2012.02.018.

[12] Reinisch B.W., Galkin I.A., Khmyrov G.M., et al. Automated collection and dissemination of ionospheric data from the digisonde network // Adv. Radio Sci.. – 2004. – V. 2. – P. 241–247.

[13] Hernandez-Pajares M., Juan J.M., Sanz J. New approaches in global ionospheric determination using ground GPS data // J. Atmos. Solar Terr. Phys. – 1999. – V. 61. – P. 1237–1247.

Proceedings of
Eighth Workshop "Solar Influences on the Magnetosphere, Ionosphere and Atmosphere"
Sunny Beach, Bulgaria, May 30 - June 3, 2016

Substorms over Apatity during 2014/2015 Observational Season

Guineva V. [1], *Despirak I.* [2], *Kozelov B.* [2]

[1] Space Research and Technology Institute, Stara Zagora Department, BAS, Bulgaria;
[2] Polar Geophysical Institute, Apatity, Russia
E-mail: v_guineva@yahoo.com

Abstract

In this work we reviewed substorms, originated during the 2014/2015 season. Observations of the Multiscale Aurora Imaging Network (MAIN) in Apatity have been used. Solar wind and interplanetary magnetic field parameters were estimated by the 1-min sampled OMNI data base. Substorm onset and further development were verified by the 10-s sampled data of IMAGE magnetometers and by data of the all-sky camera at Apatity. Subject of the review were the peculiarities in the development of substorms occurred during different geomagnetic conditions. The behavior of the substorms developed in non-storm time and during different phases of geomagnetic storms was discussed.

Introduction

Substorms are a specific phenomenon, related to a number of processes in the magnetosphere and ionosphere, summarized by Akasofu [1]. The auroral substorm development was described in detail by Akasofu [2] and filled out by Starkov and Feldshtein [3] and Isaev and Pudovkin [4]. The substorm onset and development depend on the conditions in the solar wind [e.g., 5, 6, 7] and the interplanetary magnetic field (IMF). The solar wind conditions include the solar wind parameters values, as well as the presence of different solar wind streams and their structure [8] – high speed recurrent streams (HSS), magnetic clouds (MC) and the zones in front of them Corotating Interaction Regions (CIR) and Sheaths. These solar wind structures are usually the source of geomagnetic storms that differ by their main characteristics depending on the generating structure. Therefore, substorms could be observed under different interplanetary conditions: during the passage of different solar wind streams and structures by the Earth, during development of geomagnetic storms, as well as in quiet conditions.

The goal of this work is to review substorm developments during different geomagnetic conditions: in non-storm time and during different phases of geomagnetic storms using measurements of the camera system MAIN in Apatity during 2014/2015 observational season.

Data Used

Measurements from the Multiscale Aurora Imaging Network (MAIN) in Apatity during 2014/2015 observational season have been used. The cameras observational system has being built in Apatity since 2008. The cameras characteristics, their mutual situation and the measurement process are described in detail in [9].

Solar wind and interplanetary magnetic field parameters were taken from the 1-min sampled OMNI data base (spacecraft-interspersed, near Earth data) of the Coordinated Data Analysis Website (http://cdaweb.gsfc.nasa.gov/cgi-bin/eval2.cgi). Kp indices were taken from NOAA National centers for environmental information: http://www.ngdc.noaa.gov/stp/GEOMAG/kp_ap.html via ftp.

Substorm presence was verified by the 10-sec sampled ground-based data of IMAGE magnetometers network (using the meridional TAR-NAL and MEK-NOR chains) and by data of Loparskaya and Lovozero magnetometers.

To study the substorm development data from the Apatity all-sky camera (images and keograms) and the Guppy F-044C (GC) camera with field of view ~67° (keograms) were used.

Results

From September 2014 to April 2015, during the 2014/2015 observational season 49 substorms were identified during which measurements have been performed. For the study the substorms were divided into two groups: substorms observed during geomagnetic storms and substorms in non-storm conditions. Our classification of the substorms and their number in the different groups are presented in Table 1. Every group included several sub-groups. The substorms during geomagnetic storms can occur during the main storm phase or during the recovery phase. The recovery phase was divided in near recovery phase and late recovery phase. Another sub-group of the first group was also introduced, namely "structured recovery phase", when the SYM/H index course was highly structured.

Table 1. Classification of the substorms during 2014/2015 observations.

Substorms during geomagnetic storms (22)		**Substorms during non-storm conditions (27)**	
Main phase	**8**	**Quiet conditions**	**7**
Near recovery phase	**7**	**Structures in the solar wind:**	
Late recovery phase	**3**	CIR	**1**
Structured recovery phase	**4**	Just before HSS	**2**
		HSS	**5**
		Just after HSS	**8**
		MC and HSS	**4**

The substorms during non-storm conditions were classified as substorms under quiet conditions, when no structures in the solar wind were observed, and as substorms happened when structures in the solar wind near Earth were detected, but these structures didn't provoke geomagnetic storms (see Table 1).

Further two substorms during the geomagnetic storm on 23 December 2014 and a substorm under quiet conditions on 23 March 2015 are presented as examples.

Interplanetary conditions in the time interval 23-30 December 2014

An overview of the interplanetary conditions during 23-30 December 2014 is given in Fig.1. In this time a magnetic cloud passed by the Earth followed by a HSS. The Sheath lasted from 11:10 UT to 18:45 UT on 23.12.2014, the MC continued to 21:00 UT on 23.12.2014, when a HSS overlapped. A moderate geomagnetic storm in terms of SYM/H minimal value was generated by the Sheath. The SYM/H index gained a minimum of -52 nT at 01:38 UT on 24.12.2014. This minimum consisted of 3 consecutive minima. The combination of two consecutive structures in the solar wind contributed to a long lasting recovery phase (for several days) which appears typical development in such cases (e.g. [10]). Another characteristic of the recovery phase of this storm was that it was highly structured or irregular. The SYM/H index variations reached about 50% of its range and the minima were close to the deepest one (-52 nT) (Fig.1).

Five substorms were registered during this storm:

1) 00:29:30 UT, 24.12.2014, during the structured minimum, SYM/H=-45 nT;

2)16:31:30 UT, 24.12.2014, recovery phase, SYM/H=-28 nT;

3)19:22:50 UT, 24.12.2014, SYM/H=-38 nT, recovery phase;
4) 00:40 UT, 26.12.2014, SYM/H=-33 nT, recovery phase;
5) 19:33 UT, 26.12.2014, SYM/H=-33 nT, recovery phase.
Here substorms number 2 and 3 will be presented.

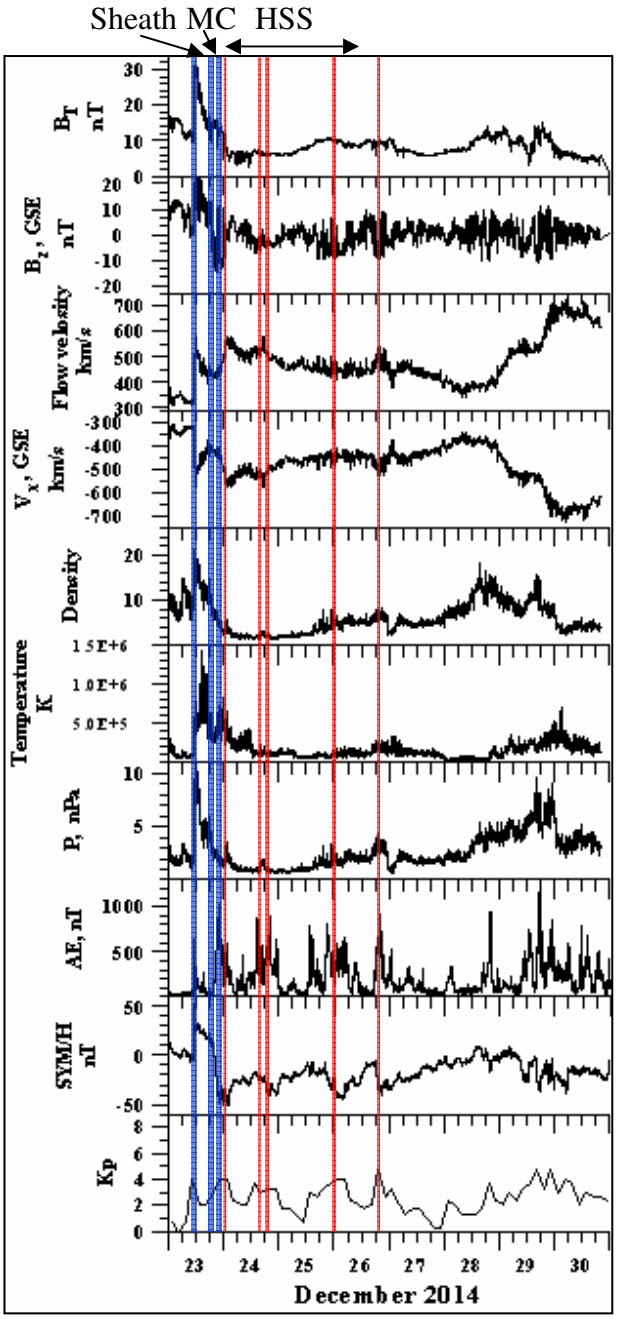

Fig.1. IMF and solar wind parameters, AE, SYM/H and Kp indices from 23 to 30 December 2014. From up to down: IMF magnitude, IMF Bz component, the flow velocity, the X component of the solar wind velocity Vx, the density, the temperature, the solar wind dynamic pressure P, the geomagnetic index AE, the SYM/H and the Kp indices. The boundaries of the structures in the solar wind are marked by blue vertical lines. The times of the 5 observed substorms during the geomagnetic storm generated on 23 December 2014 are indicated by red vertical lines.

Substorm on 24 December 2014, 16:31:30 UT

The development of the second substorm on 24 December 2014 is presented in Fig.2. The substorm was observed during the recovery phase of the storm. The value of SYM/H index at the moment of substorm onset was ~ -28 nT. According to the observations of the chain of

magnetic stations IMAGE, the magnetic disturbance spread from Oulujärvi station (OUJ) at CGM Lat.= 60.99°N to Bear Island station (BJN) at CGM Lat.= 71.45°N (the picture of the magnetic disturbances by IMAGE magnetometers is not presented here).The substorm was seen first in the all-sky images at 16:31:30 UT to the North from the station zenith. The movement of substorm auroras to South was observed till the occupation of the whole field of view by auroras after 16:59:00 UT. The bright substorm auroras reached the GC camera field of view (15°N) at 16:48 UT. The maximal relative intensity in the field of view was 160 rel. units.

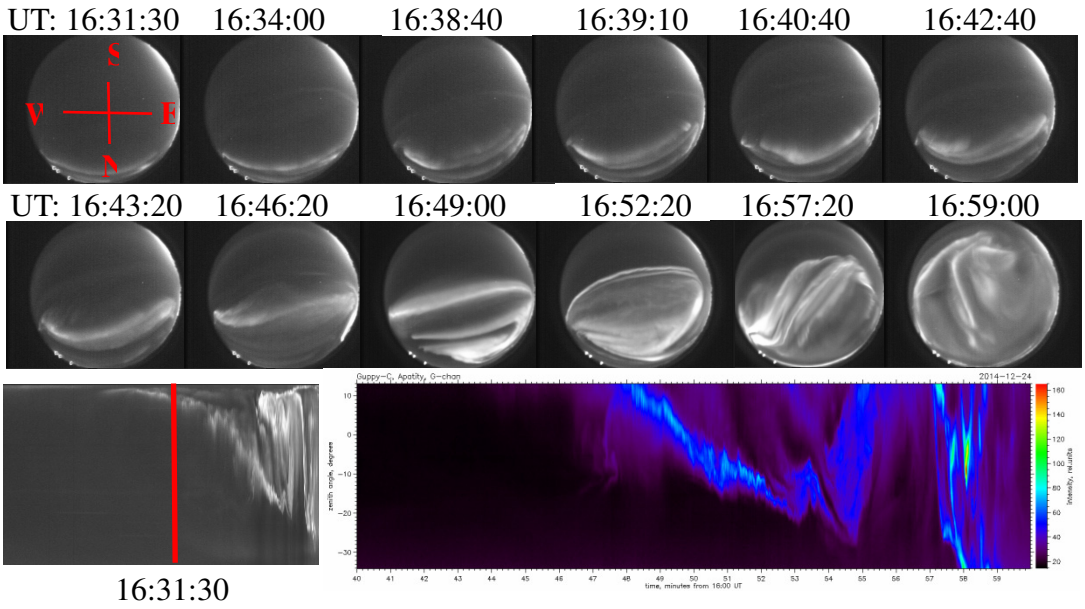

Fig.2. Development of the substorm at 16:31:30 UT on 24 December 2014 by chosen all-sky images (2 top panels), by all-sky keogram from 16:00 to 17:00 UT (left bottom panel) and Guppy (GC) camera keogram from 16:40 to 17:00 UT (right bottom panel). The world directions are marked in the first image of the top panel, the universal time is written above each image. The substorm onset is indicated in the all-sky keogram by red vertical line.

Substorm on 24 December 2014, 19:22:50 UT

The development of the third substorm registered during the geomagnetic storm is given in Fig.3. The substorm was observed also during the recovery phase of the storm. But in the interval 16:30 – 19:30 UT the SYM/H index diminished showing an increase of the geomagnetic disturbance. The value of SYM/H index at the moment of substorm onset was ~ -38 nT. By the magnetic stations IMAGE, the magnetic disturbance began at Nurmijärvi station (NUR) at CGM Lat.= 56.89°N and moved to Hornsund station (HOR) at CGM Lat.= 74.13°N, so it covered a larger latitudinal region than the disturbance in the first presented case. In this case the substorm onset at 19:22:50 UT was to the South from Apatity, nevertheless that this substorm occurred later in the recovery phase than the previous one. The auroras travelled Northward, surpassed the station zenith and covered the whole field of view. In the GC keograms the substorm auroras were seen first at 19:24:40 UT. The maximal relative intensity in the GC camera field of view was 160 rel. units.

Interplanetary conditions in the time interval 26-27March 2015

During 26-27 March 2015 the interplanetary conditions were comparatively quiet. There were not registered any flows in the solar wind. The interplanetary magnetic field magnitude was 5-7 nT, the IMF Bz component varied in a narrow range near 0, the solar wind speed decreased gradually, the proton density, the temperature and pressure in the solar wind were low. On 27 March 2015 when a substorm was observed, no sizable disturbances in the interplanetary and geomagnetic medium were registered.

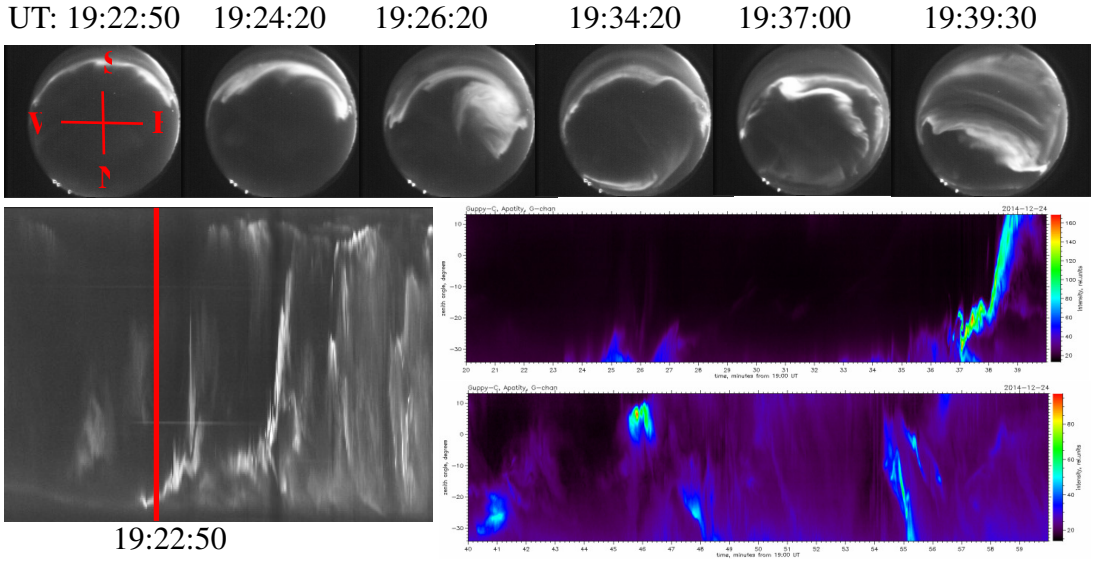

Fig.3. Development of the substorm at 19:22:50 UT on 24 December 2014 by chosen all-sky images (top panel), by all-sky keogram from 19:00 to 20:00 UT (left bottom panel) and Guppy (GC) camera keograms from 19:20 to 19:40 UT(up) and from 19:40 to 20:00 UT (down) (right bottom panels). The format of Figure 3 is the same as the one of Figure 2.

Substorm on 27 March 2015, 21:31:30 UT

The substorm on 27 March was generated under quiet interplanetary and geomagnetic conditions. The substorm development is shown in Fig.4.

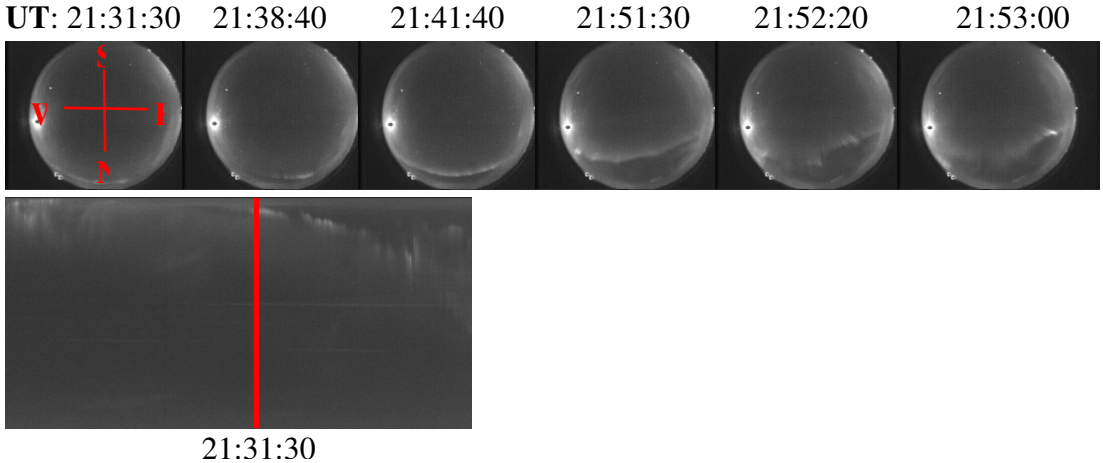

Fig.4. Development of the substorm at 21:31:30 UT on 27March 2015 by chosen all-sky images (top panel) and by all-sky keogram from 21:00 to 22:00 UT (bottom panel). The world directions are marked in the first image of the top panel, the universal time is written above each image. The substorm onset is indicated in the all-sky keogram by red vertical line.

The value of SYM/H index at the moment of substorm onset was ~ -12 nT. The IMF Bz component was -2 nT and at that moment it turned from positive to negative value. According to the observations of the chain of magnetic stations IMAGE, the magnetic disturbance spread from Pello station (OUJ) at CGM Lat.= 63.55°N to Bear Island station (BJN) at CGM Lat.= 71.45°N (the picture of the magnetic disturbances by IMAGE magnetometers is not presented here). The substorm onset occurred at 21:31:30 UT on 27 March 2015 to the North from Apatity. The auroras stayed in the Northern part of the field of view.

Conclusions

The substorms observed under quiet interplanetary and geomagnetic conditions, occurred to the North from Apatity (64.27°N CGM Lat. by 2014). The substorm expansion was seen, but substorm auroras stayed in the Northern part of the field of view. Substorms, connected to structures in the solar wind as CIR, HSS, Sheath or MC, which provoked some disturbances, but a geomagnetic storm was not generated, may be observed to the North from Apatity, over the station zenith or to the South from Apatity.

Substorms, originated during the main storm phase or near the SYM/H minimum in the recovery phase, occurred to the South of Apatity, and substorm auroras expansion to North was observed. For substorms during the recovery phase or the late recovery phase, auroras were observed near the station zenith or to the North of the Apatity station, and their motion from North to South was registered. Substorms, generated during a structured or irregular recovery phase may occur to the South or to the North from the station zenith depending mainly on the stage of the geomagnetic disturbance (the SYM/H value).

The boundary between the substorms originated to the South of Apatity and the ones occured to the North from the station in terms of SYM/H index is in the range 35-50 nT.

The maximal relative intensity of the substorm features in the GC camera field of view is considerably larger during the substorms, arising to the South from Apatity.

Acknowledgements.

We are grateful to J. N. King and N. Papatashvili, NASA GSFC and CDAWeb for the data from the OMNI data base. The paper was partly supported by the Program No 7 of the Presidium of the Russian Academy of Sciences (RAS). The study is also a part of a joint Russian - Bulgarian Project 2-14 of PGI RAS and IKIT-BAS under the Fundamental Space Research Program between RAS and BAS.

References

[1] Akasofu S.-I. Several 'controversial' issues on substorms// Space Sci. Rev.- 2004.-113.- P:1-40.
[2] Akasofu S.-I. The development of the auroral substorm// Planet. Space Sci.- 1964.-12.-P.273-282.
[3] Starkov G. V., Feldshtein Ya. I. Substorms in the polar auroras// Geomagnetism and aeronomy.- 1971.-11.-P.560-562.
[4] Isaev S. I., P u d o v k i n M. I. Polar aurora and processes in Earth magnetosphere//Ed. OL, A.I.-Moskow: Nauka.- 1972.
[5] Sergeev V. A., Yakhnin A. G., Dmitrieva N. P. Substorm in the polar cap – the effect of high-velocity streams of the solar wind// Geomagn. Aeron.- 1979.-19.-P.1121-1122.
[6] Yakhnin A. G., Despirak I. V., Lyubchich A. A. and Kozelov B. V. Solar wind control of the auroral bulge expansion// In Proceedings of the 7h International Conference on Substorms, Levi, Finland, 2004, Ganushkina N. and T. Pulkkinen (Ed.)- 2004. -Helsinki: Finnish Meteorological Institute.-P.31-34.
[7] Despirak I. V., Lubchich A. A., Biernat H. K., Yakhnin A. G. Poleward expansion of the westward electrojet depending on the solar wind and IMF parameters// Geomagn. Aeron.- 2008.-48 (3).-P.284-292.
[8] Despirak I. V., Lubchich A. A., Yakhnin A. G., Kozelov B. V., Biernat H. K. Development of substorm bulges during different solar wind structures// Ann. Geophys.- 2009.-27.-P.1951-1960.
[9] Kozelov, B.V., Pilgaev S.V., Borovkov L.P., Yurov V.E. Multi-scale auroral observations in Apatity: winter 2010-2011// Geosci. Insrum. Method. Data Syst.-2012.-1.-P.1-6.
[10] Guineva V., Despirak I., Kozelov B. Substorms observations during two geomagnetically active periods in March 2012 and March 2015// Sun Geosph.-2016.-11(2).-P.101-105.

Proceedings of
Eighth Workshop "Solar Influences on the Magnetosphere, Ionosphere and Atmosphere"
Sunny Beach, Bulgaria, May 30 - June 3, 2016

Basic Results from the Scanning Spectrophotometer "EMO-5" onboard "IC Bulgaria-1300"

Guineva V., Stoeva P.

Space Research and Technology Institute (SRTI), Stara Zagora Department, BAS, Bulgaria
E-mail: v_guineva@yahoo.com

Abstract

The basic results from EMO-5 on board Bulgaria-1300 are summarized. EMO-5 consists of two photometric systems: filter system (SF) measuring the intensities of 5577Å, 6300 Å, 4278 Å, 4861Å and 7320 Å emissions in the foot point every 16 s., and spatial scanning system (SS) registering the 6300 Å intensity. The auroral oval and polar cap boundaries and their locations under different geomagnetic conditions have been defined by optical and energetic particles data. The average ratios of the optical emissions in the auroral oval zones and in the polar cap at different conditions have been analyzed. The conditions of appearance of SAR arcs, their structure and their geographical distribution have been studied. The seasonal and daily variations of I6300 emission in the equatorial F-region have been examined.

Introduction

One of the most impressive Bulgarian space projects in the 80-ies of the 20th century was named Bulgaria-1300 in honour of the 1300th anniversary of the Bulgarian state. All scientific instruments on board Intercosmos 22, called IC Bulgaria-1300 were designed and manufactured in Bulgaria. Three of these instruments were result of the work of the Stara Zagora Department scientific team. One of them was the scanning spectrophotometer EMO-5. It worked successfully during the whole period of satellite operation from August 1981 to May 1982.

The satellite orbit was almost polar and covered all geographic latitudes which enabled the study of a variety of phenomena. Processes occuring in the equatorial region, at mid-latitudes, as well as at auroral and polar latitudes in the Earth upper atmosphere were investigated. Data from the whole period of measurements have been examined. The purpose of this paper is to introduce some basic results of the studies of EMO-5 measurements to commemorate the 35th anniversary of the launch of Bulgaria-1300 satellite.

Instrumentation

EMO-5 is a multi-filter optical scanning spectrophotometer manufactured in Stara Zagora. Its appearance is shown in Fig.1. The instrument was described in detail in [1].

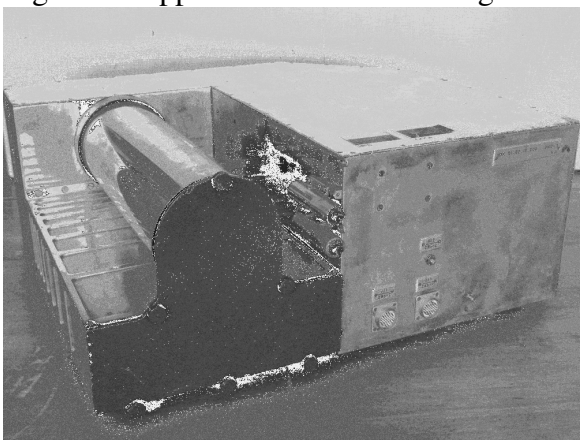

Fig.1. The spectrophotometer EMO-5.

It was designed for the investigation of the temporal and spatial characteristics of the optical emissions. It consists of two photometric systems: filter system (SF) measuring in nadir the intensities of 5577Å, 6300 Å, 4278 Å, 4861Å and 7320 Å emissions every 16 s., and spatial scanning system (SS) registering the 6300 Å intensity in a band of about 270 km width along the satellite orbit projection. A processing method of the spatial scanning system data based on spline interpolation was worked out, described in [2, 3].

Results

The measurement séances of EMO-5 were selected and a collection of 111 spectra including the intensities of all registered emissions each was published [4]. By the emissions intensities processes at different latitudes were examined.

Auroral oval investigations

The boundaries of the nightside auroral region zones including the auroral oval were determined and located by simultaneous measurements of optical emissions and precipitating particles during the period of high solar activity 1981-1982 [5]. The zones boundaries were determined for 43 orbits by optical data. The zones are shown in Fig.2 for one case (orbit 1547). From North to South they are as follows: 1) soft zone poleward of the oval; 2) discrete component of the auroral oval; 3) diffuse component of the auroral oval; 4) diffuse luminescence equatorward of the oval. For 25 of the orbits the zone boundaries were determined from 1keV electrons flux down, as well. The boundaries defined by both ways coincided very well (Fig.3). The locations of the boundaries and the auroral oval width depending on the geomagnetic conditions have been studied.

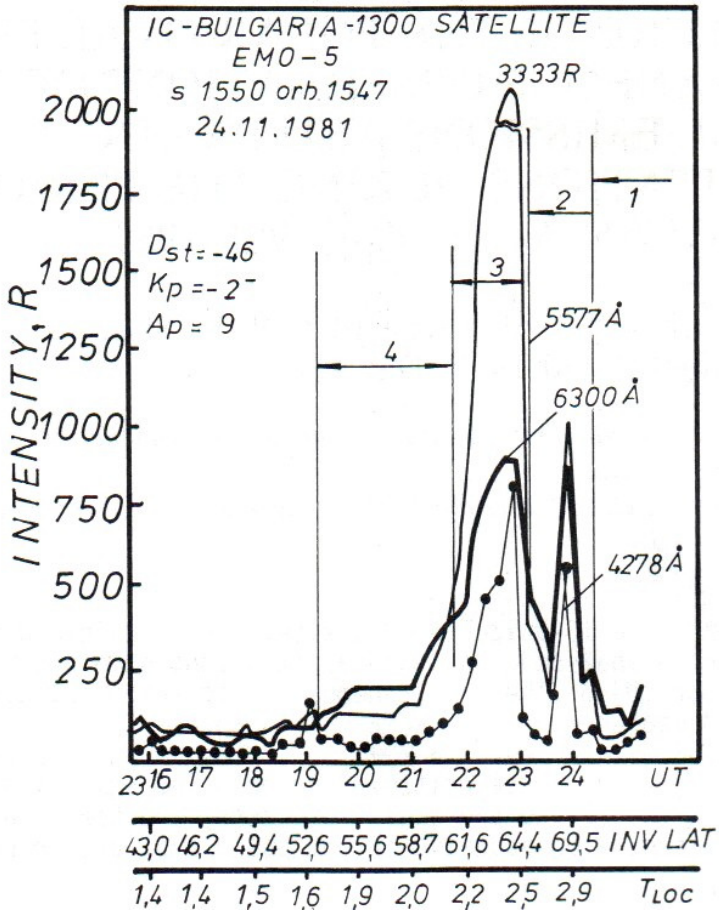

Fig.2. Zones of the nightside auroral region: 1) soft zone poleward of the oval; 2) discrete component of the auroral oval; 3) diffuse component of the auroral oval; 4) diffuse luminescence equatorward of the oval.

Polar cap studies

The polar cap was examined by data from 39 orbits crossing it. Optical data were present for 21 of them. The polar cap boundary was determined by optical data and by the 0.2 keV electron flux. The boundaries found in both ways, coincided completely. An example of the boundaries of the auroral oval and the polar cap by data of the luminosity and the particle and energy fluxes (orbit 2044) is given in Fig.4.

The dependence of the polar cap boundary on the Bz component of the Interplanetary Magnetic Field, the average intensity ratios and the relation of the average emissions intensities in the polar cap to the average particle flux with energies 0.2-15 keV were studied. It was confirmed that the precipitating electrons energy flux was in closest relation to the polar cap luminosity from all other examined quantities [6].

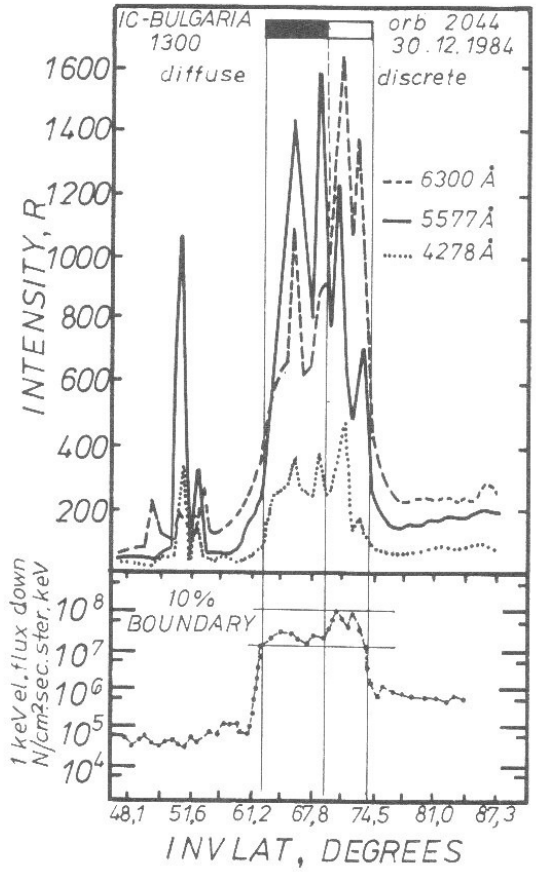

Fig.3. Polar oval boundaries (the vertical lines) defined from optical and 1 keV electron flux data, for one case.

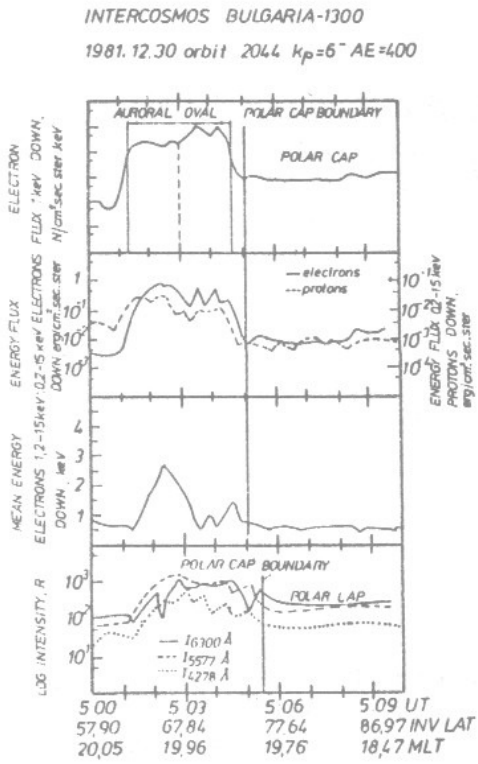

Fig.4. An example of the boundaries of the auroral oval and the polar cap by data of the luminosity and the particle and energy fluxes (orbit 2044).

SAR arcs results

The conditions for SAR-arcs appearance, their locations and the dependence of their intensity and form on the geomagnetic conditions were studied by IC Bulgaria-1300 and DE-2 (Dynamics Explorer-2) data. 19 SAR arcs have been observed in 74 orbits by EMO-5 optical measurements from 21 August 1981 to 27 May 1982 [7]. Data from DE-2 have been used in the studies, too. In Fig.5 the red line intensity registered during orbit 203 (upper panel) and the electron temperature Te and ion density measured in the same time (bottom panel) are presented. The detected SAR arc is marked by vertical lines. The SAR arcs region coincided with the one of suprathermal electron precipitation and of significant Te increase.

At considerable geomagnetic activity discrete arcs appeared in the main trough of the electron concentration. The geographical distribution of the detected SAR arcs is shown in Fig.6.

The spatial structure of the SAR arcs was examined by data of the EMO-5 spatial scanning system [3]. In Fig.7 the detailed spatial distribution of the SAR arc detected in orbit 203 by FS channel data (see Fig.5) is presented. The arc boundaries are marked by continuous line. The central dotted line indicates the moments of FS channel measurements. The SAR arc structure is complex: a main part with inhomogeneuos increased glow is observed, on both sides of which the intensity decreases irregularly.

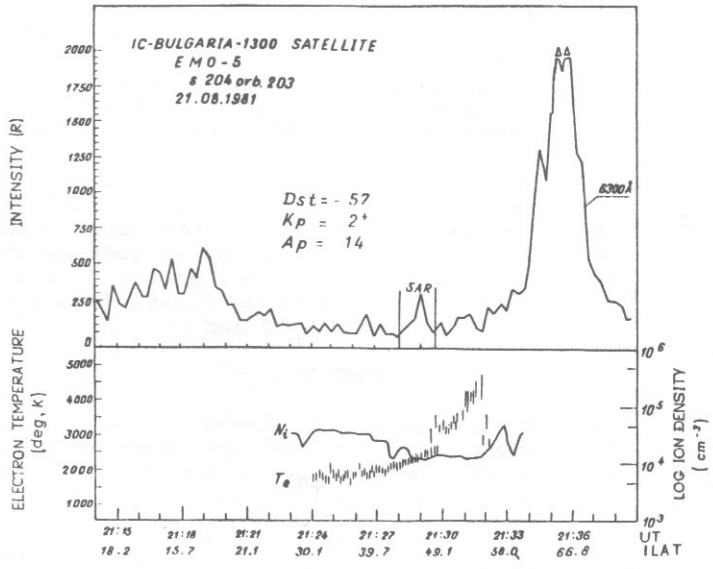

Fig.5. Red line intensity, electron temperature and ion density depending on UT for orbit 203 of IC Bulgaria-1300. The boundaries of the detected SAR arc are marked by vertical lines.

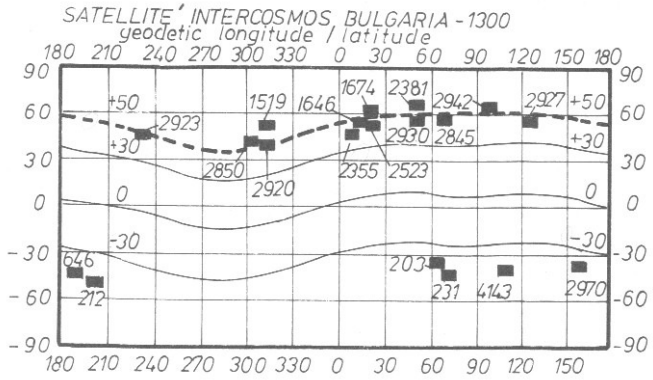

Fig.6. Geographical distribution of 19 SAR arcs detected in the measurements of EMO-5 and studied.

6300 Å emission in the equatorial ionosphere

The seasonal and diurnal variations of the OI 6300 Å emission intensity in the equatorial F region are studied [8]. 27 orbits over the equator are used. The presence of transequatorial transport from summer to winter hemisphere expressed by the asymmetry in the equatorial red arc brightness was confirmed. It was established that the transequatorial transport wasn't a continuous process. The diurnal variation of I_{6300} is maybe influenced not only by the ExB drift, but also by other dynamic factors.

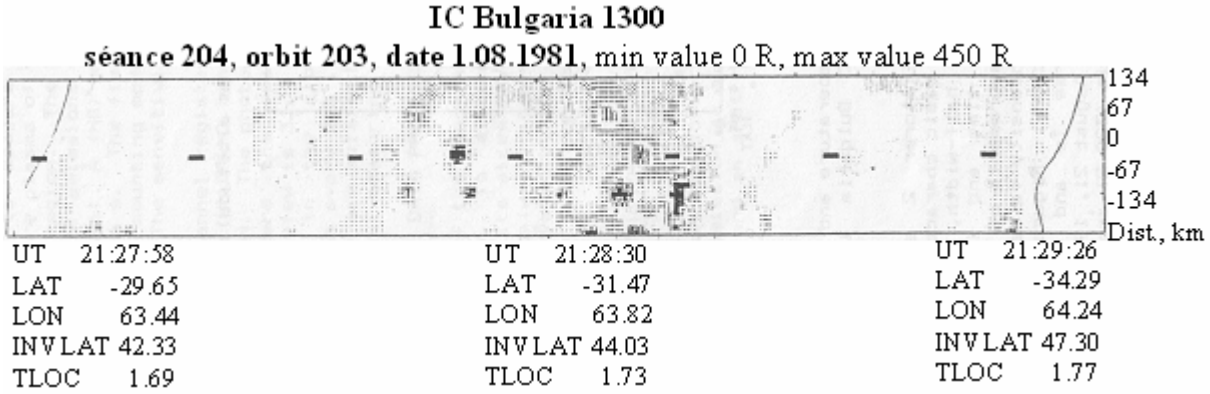

Fig.7. Detailed two-dimensional distribution of the same SAR arc as in Fig.5, derived from the data of the spatial scanning system of EMO-5 (7 measurements per scan). The distance from nadir in km is marked on the Y-axe. The intensity scale is from 0 (white colour) to 450 R (black colour).

Summary

By the intensities of the registered by EMO-5 optical emissions the processes in the upper atmosphere at different latitudes: from the equator through mid-latitudes up to the auroral and polar zones have been investigated.

The zones of the nightside auroral region have been defined. The polar oval boundaries have been determined by simultaneous optical and particle precipitation observations. The intensity ratio I5577/I6300 and the course of the electron flux in the polar oval zones, as well the positions and sizes of the zones under different geomagnetic conditions have been studied.

The polar cap boundary is defined by optical data and by the 0.2 keV EEF.

The average ratios I6300/I5577 and I6300/I4278 in the auroral oval zones and in the polar cap at different conditions have been analyzed.

The conditions of appearance of SAR arcs, their situations, the dependences of their intensity, form and dimensions under different geomagnetic conditions have been studied.

The seasonal and daily variations of I6300 emission in the equatorial F-region have been examined.

References:

[1] Gogoshev, M.M., N. Petkov, Ts. Gogosheva, St. Spasov, Iv. Kostadinov, A. Kuzmin, Airglow Atmospheric Imager on board the IC-Bulgaria-1300 satellite, Adv. Space Res., vol.2, No7, pp.115-120, 1983

[2] Nikolov, B.A., R. Werner, S. H. Spasov, Image Formation by Generalized Spline-Functions, Comptes rendus de l'Academie Bulgare des Sciences, vol.42, No8, pp.27-30, 1989

[3] Stoeva, P., V. Guineva, St. Spasov, Characteristics of a SAR Arc Registered by the EMO-5 Filter and Spatial Scanning Photometric System Aboard the IC Bulgaria-1300 Satellite on August 21st 1981, Adv. Space Res., vol.13, No4, pp.(4)131 - (4)134, 1993

[4] Gogoshev, M., P.Maglova, V.Guineva, Airglow Optical Data from IC Bulgaria - 1300 Satellite, Preprint CLSR N 85-01, 1985

[5] Gogoshev, M.M., G.G.Shepherd, P.V.Maglova, V.Chr.Guineva and Ts.P.Datchev, Structure of the Polar Oval from Simultaneous Observations of the Optical Emissions and Particle Precipitations During the Period of High Solar Activity 1981 - 1982, Adv. in Space Res., vol.7, No8, pp.(8)7 - (8)10, 1987

[6] Guineva, V., P. Stoeva, Investigation of the Polar Cap Using Data from the IC Bulgaria - 1300 Satellite, Adv. in Space Res., vol.13, No4, pp.(4)29-(4)32, 1993

[7] Gogoshev, M.M., V.Chr.Guineva, P.V.Maglova and T.Markova, Sar-Arcs and Emissions in the Main Trough of the Electron Concentration, Adv. in Space Res., vol.7, No8, pp.(8)15-(8)19, 1987

[8] Kostadinov, Iv., P.Stoeva, V.Guineva, OI 630 nm Emission in the Equatorial Ionosphere from 'Intercosmos-Bulgaria-1300' Data, Adv. in Space Res. (ISSN 0273-1177), vol.10, No11, pp. 93-96, 1990

Proceedings of
Eighth Workshop "Solar Influences on the Magnetosphere, Ionosphere and Atmosphere"
Sunny Beach, Bulgaria, *May 30 - June 3, 2016*

Heliospheric Current Sheet as a Factor of Geomagnetic Activity Floor

Asenovski S.

Space Research and Technology Institute, Bulgarian Academy of Sciences, Sofia, Bulgaria
E-mail: asenovski@gmail.com

Abstract

Observable significant depressions of the Earth`s magnetic field, which are an indicator for changes in the near-Earth space plasma parameters, are caused mainly by transient Interplanetary coronal mass ejections (ICME) and High speed solar wind streams (HSS). However, even in the absence of these two manifestations of the solar activity, when our planet "floats" in the relatively "quiet" space, there are still geomagnetic disturbances. Considering the ICME and HSS free periods for the last four solar cycles, in this work it is shown that the role of the heliospheric current sheet (HCS) in the geomagnetic activity "floor" is significant.

Introduction

According to the NOAA Space Weather Scales (http://www.swpc.noaa.gov/noaa-scales-explanation) a geomagnetic storm can be defined when the geomagnetic planetary index Kp is at least 5 or greater. Considering the global picture of the geomagnetic disturbances most of the time (up to 60 %) during any 11-years solar cycle (SC), Kp is less than 5 (fig. 1). There are two phenomena causing relatively strong geomagnetic storms: high speed streams (HSS) ejected by solar coronal holes and the interplanetary regions identified with the coronal mass ejections (CMEs) [1-2]. However, even in the absence of these two manifestations of the solar activity, when our planet "floats" in the relatively "quiet" space, there are still geomagnetic disturbances. For example each two years around any solar minimum up to 50 % of the time the Earth's is not influenced by HSS nor CME [3] and at the same time Kp is different from zero.

Feynman [4] linked geomagnetic activity and sunspots, in a way to show that the annual average *aa* index can be decomposed into two functions – the first one caused by short lived solar wind sources (CME, short lived coronal holes) and the second one related predominantly to the polar coronal holes (HSS). Further research [5] supplies additional component which expresses the geomagnetic activity in the absence of sunspots, i.e. the geomagnetic activity "floor". All these three components represent how the long-term averages of the solar wind drivers influence the Earth's magnetosphere.

Recognizing the geomagnetic "floor" as an averaged state of the disturbed geomagnetic field when there are no sunspots actually neglects the fact that even in the spotless Sun there can be a HSS reaching the Earth [6]. If we assume an average Kp index (or any other geomagnetic index) in a relatively long time interval with no HSS and ICME (quiet periods), we can define the geomagnetic activity "floor" as a minimal value of the index under which the geomagnetic activity cannot fall. In the specific case when the averaged time interval is short (few hours or days) the geomagnetic "floor" cannot be defined or it will be zero. One of the first questions which arise here is what determines the geomagnetic floor variation? The answer probably includes factors such as properties of the slow solar wind (which originate from regions near the equatorial coronal streamers), properties of the fast solar wind (coming from the polar coronal holes) and conditions inside the magnetosphere.

In this work it is argued that an additional influence on the geomagnetic "floor" can be caused by the heliospheric current sheet (HCS) in sense of its crossing.

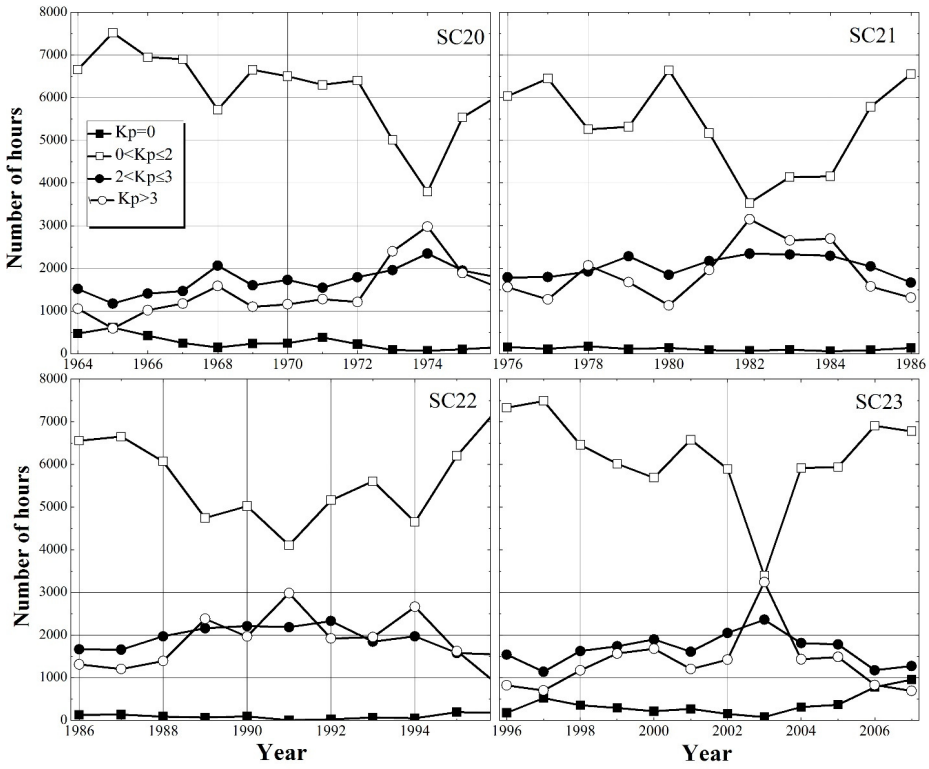

Fig.1. Kp index during the last four solar cycle (SC).

The heliospheric current sheet (HCS), a dynamic object which can be described as a plane separating the heliosphere into two regions with opposite magnetic polarity, is roughly ~10000 km thick at 1 AU [7]. HCS inclination is modulated by the solar activity (variation of the solar magnetic field), as during the solar minimum it nearly matches with the solar equatorial plane and it is almost perpendicular during solar maximum [8]. A highly variable and high-beta (beta is the ratio of the gas to field pressure) region covers HCS named heliospheric plasma sheet (HPS) [9]. Its thickness range is from 220000 to 400000 km [7].

DATA and METHODS

In the purpose of the current investigation several data sets are used – data for geomagnetic Dst index obtained from the World Data Center for Geomagnetism, operated by the Data Analysis Center for Geomagnetism and Space Magnetism at Kyoto University, Japan (http://swdcwww.kugi.kyoto-u.ac.jp/dstae/index.html.), L. Svalgaard's list of the sector boundaries in the solar wind (http://wso.stanford.edu/SB/SB.Svalgaard.html) and catalogues for the high speed solar wind streams covering the last four solar cycles [10-12]. To determine the period of ICME passage the hourly values of the plasma parameters from OMNI data base (http://omniweb.gsfc.nasa.gov/) are used [13] and the categorization is described in [14]. Considering the CME and HSS free periods for ten crossings of the Heliospheric current sheet (five crossings from positive to negative polarities and five vice versa) a superposed epoch analysis of Dst index has been performed.

RESULTS and DISCUSION

The main result of this research is shown on Fig. 2, where it can be seen that the Dst index, which determines the ring current and the geomagnetic disturbances, decreases after both cases of HCS crossings – from positive to negative polarity and vice versa. It can be concluded that the configuration of the interplanetary magnetic field does not contribute to the observed small variations of the Dst index since the behavior of the index is identical for both reversals. One possible reason for this decrement is the highly variable regions (heliospheric plasma sheet) which are close to the HCS. As it has been shown [15-17] the HCS crossings

cause significant changes in the different solar wind parameters – decrease the proton temperature (with more than 5000 K) and flow speed (with more than 100 km/s) and increase the proton density (more than 10 cm^{-3}). All these changes match with the day zero (the day of crossing). Here the minimum value of the Dst index does not match with day zero but with the first day after the crossing which corresponds to the heliospheric plasma sheet.

Each year (since 1926) the Earth crosses the HCS from 10 to 45 times (according L. Svalgaard's list of the sector boundaries), or several times per month and the number of the crossings seems not to depend on the solar activity (fig. 3). The contribution of all these crossings through any solar cycle to the geomagnetic activity floor can be reasonable.

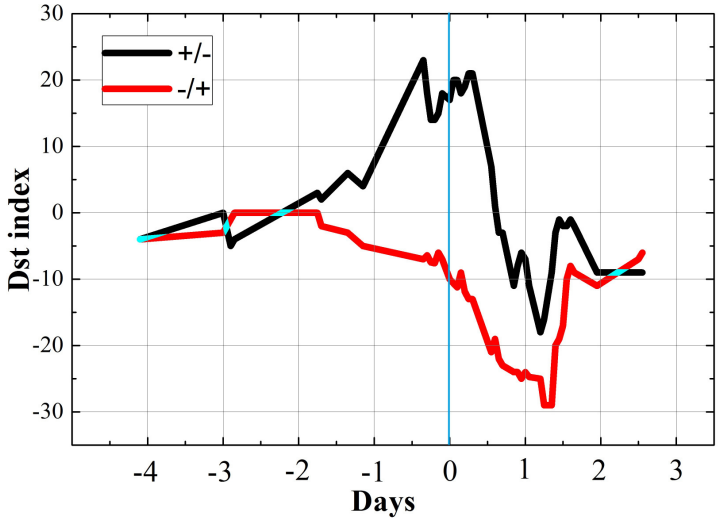

Fig.2. Superposed epoch plot of Dst index during ten HCS crossings.

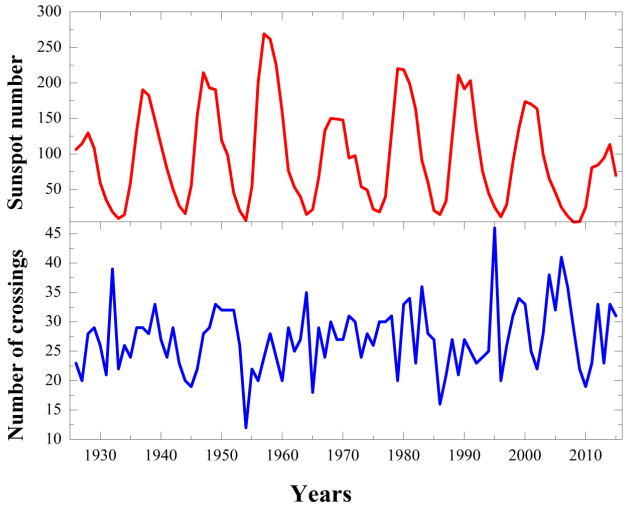

Fig.3. Number of the HCS crossing (bottom panel) in comparison of the solar activity

Conclusions

The study of the possible HCS/HPS influences on the geomagnetic disturbances opens a new chapter in the investigation of the geomagnetic processes. The results presented here can be summarized as 1) HCS crossing causes decreasing of the Dst index; 2) the interplanetary magnetic field configuration does not contribute to the small variations of the geomagnetic field during HCS crossings; 3) the possible reason for the Dst decreasing is the highly variable and high-beta heliospheric plasma sheet.

In the future the author plans to expand the research including more HCS crossings and their influence on the Polar Regions.

Acknowledgments.

This work was supported by the Young Scientists Support Program of the Bulgarian Academy of Sciences under grant №243 "Variation of the background solar wind using space and ground base experimental data".

References

[1] Gonzalez W.D., Tsurutani B.T., Clúa De Gonzalez A.L., Interplanetary origin of geomagnetic storms, Space Science Reviews, 1999, Volume 88, Issue 3, pp 529-562.
[2] Richardson I.G., Cane H.V., Solar wind drivers of geomagnetic storms during more than four solar cycles, J. Space Weather Space Clim., 2012, Volume 2. A01.
[3] Kirov B., Asenovski S., Georgieva K., Obridko V. N., What causes geomagnetic activity during sunspot minimum?, Geomagnetism and Aeronomy, 2015, Vol. 55, No. 8, pp. 1033–1038.
[4] Feynman J., Geomagnetic and solar wind cycles, 1900–1975, J. Geophys. Res., 1982, vol. 87, pp. 6153-6162.
[5] Kirov B., Obridko V. N., Georgieva K., Nepomnyashtaya E. V., Shelting B. D., Long-term variations of geomagnetic activity and their solar sources, Geomagnetism and Aeronomy, 2013, Vol. 53, No. 7, pp. 813-817.
[6] Echer E., Tsurutani B.T., Gonzalez W.D., Kozyra J.U., High speed stream properties and related geomagnetic activity during the whole heliosphere interval (WHI): 20 March to 16 April 2008, Solar Phys, 2011, 274, pp. 303–320.
[7] Winterhalter D., Smith E. J., Burton M. E., Murphy N., McComas D. J., The heliospheric plasma sheet, J. Geophys. Res., 1994, vol. 99, pp. 6667–6680.
[8] Smith E. J., The heliospheric current sheet, J. Geophys. Res., 2001, vol. 106, pp. 15819–15831.
[9] Crooker N. U., Huang C.-L., Lamassa S. M., Larson D. E., Kahler S. W., Spence H. E., (2004), Heliospheric plasma sheets, J. Geophys. Res., 2004, vol. 109, A03107.
[10] Lindblad, B.A., Lundstedt, H., A catalogue of high-speed plasma streams in the solar wind, Solar physics, 1981, 74, pp. 197-206.
[11] Mavromichalaki, H., Vassilaki, A., Fast plasma streams recorded near the Earth during 1985-1996, Solar physics, 1998, 183, 181-200.
[12] Xystouris G., Sigala E., Mavromichalaki H., A Complete Catalogue of High-Speed Solar Wind Streams during Solar Cycle 23, Solar Phys., 2014, 289, pp. 995–1012, DOI 10.1007/s11207-013-0355-z.
[13] King J.H., Papitashvili N.E., Solar wind spatial scales in and comparisons of hourly wind and ACE plasma and field data, J. Geophys. Res., 2005, 110, 2104.
[14] Richardson I.G., Cane H.V., Regions of abnormally low proton temperature in the solar wind (1965-1991) and their association with ejecta, J. Geophys. Res., 1995, 100, A12, 23397-23412.
[15] Gosling J.T., Borrini G., Asbridge J.R., Bame S.J., Feldman W.C., Hansen R.T., Coronal streamers in the solar wind at 1 AU, J. Geophys. Res., 1981, 86, 5438.
[16] Borrini G., Gosling J.T., Bame S.J., Feldman W.C., Wilcox J.M., Solar wind helium and hydrogen structure near the heliospheric current sheet: A signal of coronal streamers at 1 AU, J. Geophys. Res., 1981, 86, 4565.
[17] Suess S.T., Ko Y.-K., R. von Steiger, Moore R.L., Quiescent current sheets in the solar wind and origins of slow wind, J. Geophys. Res., 2009, 114, A04103, doi:10.1029/2008JA013704.

Proceedings of
Eighth Workshop "Solar Influences on the Magnetosphere, Ionosphere and Atmosphere"
Sunny Beach, Bulgaria, May 30 - June 3, 2016

Monitoring of Space Weather Electromagnetic Parameters in the Ionosphere. Projects: "Chibis-M", "Obstanovka (1 stage)", "Vernov".

Klimov S.[1], Grushin V.[1], Novikov D.[1], Pilipenko V.[1], Belyakova L.[1], Rodin V.[1], Georgieva K.[2],Kirov B.[2], Ferencz Cs.[3], Szegedi P.[3], Korepanov V.[4], Belyayev S.[4], Marusenkov A.[4], Dudkin F.4, Pronenko V.[4]

[1] Space Research Institute of the RAS, Russia
[2] Space Research and Technology Institute of the BAS, Bulgaria
[3] Eötvös University, Hungary
[4] Lviv Centre of Institute for Space Research of NANU/SSAU, Ukraine
E-mail: sklimov@iki.rssi.ru

Abstract

The investigation and monitoring of the electromagnetic environment of the Earth and of the Earth-like planets (e.g. Moon, Venus, Mars and Mercury) is of great importance, because this opens the door for the comparative study of these planets, their evolutions and actual states. One of recent results of the long-time trend investigation in some important areas of the Earth ionospheric electrical parameters [1], VLF natural signal intensity [2], Schumann resonance intensity [3] revealed significant decreasing of the total lightning activity.

Actually we have no final answer to this important question what confirms that the satellite monitoring of electromagnetic environment of the Earth is a very actual task. Large amount of archived satellite data gathered during earlier missions are successfully integrated in various models of the upper atmosphere and ionosphere. New data mining techniques form the base of the idea of the Ionosphere Waves Service (IWS) [4]. The aim of the IWS is not including some new kind or set of measured data, but processing the available derived parameters of described wave-like phenomena by specific algorithms.

Now in the IWS configuration the new data are included from projects: "Chibis-M" – 2012-2014, "Obstanovka (1 stage)"– 2013-2014, "Vernov"– 2014. In these projects Magnetic Wave Complex (MWC) [5] was used which operated in the frequency range of 0.1 Hz – 40 kHz (sensors developed by Lviv Centre of Institute for Space Research of NASU-SSAU, the SAS3 instrument – by Space Research Group of Eötvös University and BL Electronics Ltd.).

Introduction.

The MWC data on the electromagnetic parameters in the ionosphere obtained in quiet and disturbed geomagnetic conditions with high spectral resolution and large dynamic range allowed us to identify specific characteristics of a number of ionospheric and magnetospheric radiations, characterizing space weather and global lightning activity.

The MWCs in these experiments operated in two modes:

- registration and transmission by telemetry channels of waveforms of electromagnetic radiations - *"waveform"* mode;
- signals registration with subsequent calculation by on-board computer of the spectra of electromagnetic radiations and their transfer by telemetry channels - *"monitoring"* mode.

For space weather research (as well as for atmospheric weather) and ionosphere dynamic studies, in the first place, it is necessary to conduct continuous monitoring of the parameters. This is because the properties and structure of the ionosphere vary according to season (winter-summer), time of day (day and night) and geomagnetic conditions.

In the ionosphere there are three areas (fig. 1): high-latitude, mid-latitude, equatorial. For mid-latitude ionospheric model IRI, its structure and conditions in it are fairly well defined. High-latitude and equatorial ionosphere are the "problematic" regions of the ionosphere.

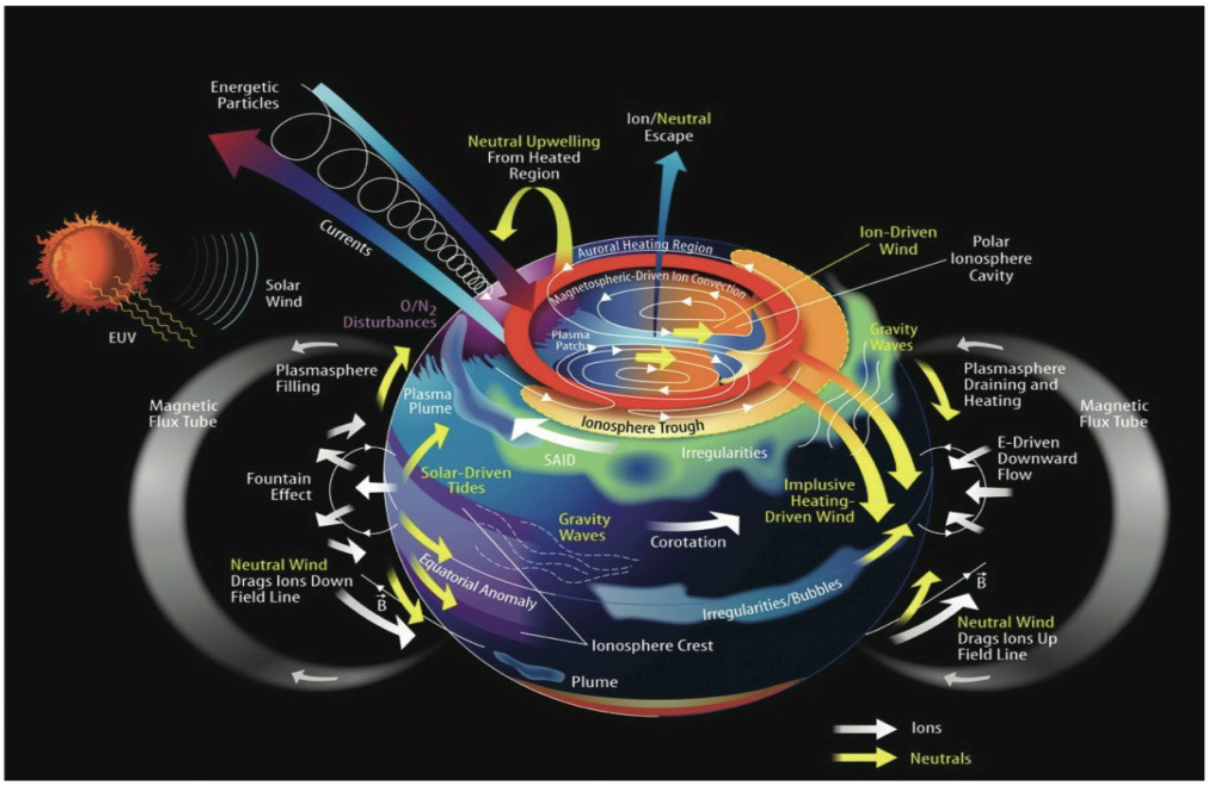

Figure 1. Schematic structure of the ionosphere.

In "Long-term Program of scientific research and experiments planned for the Russian segment of the ISS," the KNTC of the Roscosmos realized 2 space experiments with the use of the MWC:

- "***Obstanovka (1 stage)***",
- **Micro-satellite "*Chibis-M*"**.

It should be noted that the orbit of the ISS does not reach high latitudes. Because of this in the mentioned experiments the high-latitude ionosphere is not examined. More details of these experiments are given below.

"Obstanovka (1 stage)",2013-2015 .

In the experiment "Obstanovka (1 stage)" [6, 7] mostly monitoring studies were conducted. The main goals of the "Obstanovka 1-st stage" experiment were:

- Investigation of the influence of the factors of space weather on the state of the middle-latitude and equatorial ionosphere.
- Geophysical studies of the plasma-wave processes, connected with the manifestation in the ionosphere of solar-magnetosphere-ionosphere-atmosphere connections.
- Monitoring of the low-frequency electromagnetic radiations of anthropogenic nature.

A typical example (fig. 2) of monitoring studies (0.01-22kHz) in this experiment are presented for *2013-07-05 (UT+3 18:00-24:00* - 4 orbits*).*

According to the monitoring data of Figure 2 mid-latitude (L> 3) and equatorial regions are clearly distinguished from orbit to orbit.

The observed (Fig. 2) difference of the intensity of broadband electromagnetic noise (E and B) at mid-latitudes in the Northern and Southern hemispheres is due, primarily, with the change of illumination along the ISS orbit (*Sun* and *Shd)* of the ionosphere and especially of the electric sensors measuring E component. In the example shown in Fig. 2, in the Northern hemisphere (*Sun* area of the orbit) at L~5 the broadband radiation of hiss type is observed (19:06:08, 20:39:03 and 22:11:58 UT).

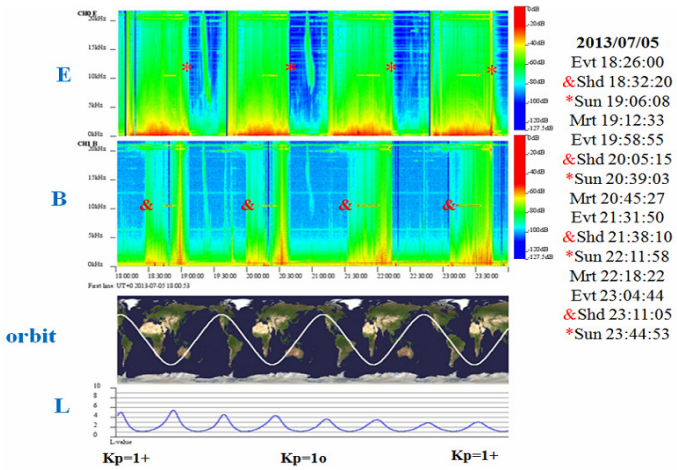

Figure 2. "Obstanovka (1 stage)". Monitoring of electric E (1st- upper panel) and magnetic B (2nd) components at frequences 0.01-22kHz at 2013-07-05 (start time: UT+3 18:00) during 4 orbits (3rd panel– projection of the ISS orbit; 4th– L-parameter) during quiet geophysical conditions (Kp < 1+). The table at right shows the times when the ISS was at: Evt - evening terminator on the Earth's; Shd - joining in the Earth's shadow; Sun - coming out of solar part of the orbit; Mrt - morning terminator.

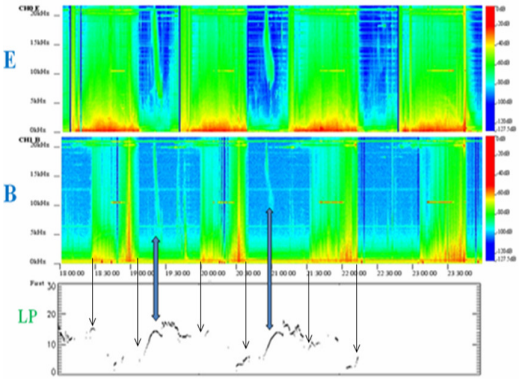

*Figure 3. "Obstanovka (1 stage)". Monitoring of electric **E** (1st- upper panel) and magnetic **B** (2nd panel) components Data identical to Fig. 2. Bottom panel - synchronous potential data of the ISS outer surface measured by the LP device.*

Of course, the ISS, as a very large spacecraft, has an impact on the nature of the distribution of surrounding plasma sheath, and hence the impedance of the MWC sensors. This is influencing the electrical components E sensor. As to the magnetic component B sensor, its data is well correlating with the change of the illuminated and shadowed parts of the ISS orbit, when there are commutations in the power supply system of the station. Intense low-frequency (<1 kHz) radiation in the E component is observed almost continuously along the shadowed parts of the ISS orbits, what may be also attributed by power supply system influence.

Significant changes in the ISS surrounding environment is confirmed also by the synchronous measurement data (Fig. 3) of potential of the external surface of the station, carried out by the Langmuir Probe (LP) [8], which is the part of the "Obstanovka (1 stage)" space experiment [9].

Sudden changes in the intensity of E and B radiation at the illuminated and shadowed parts of the orbit (in the figure 3 marked by thin arrows) correlate well with the changes of LP potential, especially B component. The current-voltage LP characteristics in shadowed areas are very noisy and the definition of potential is impossible. The observations of the hiss type radiation (thick arrows) are associated with the precipitation of electrons and correlate with the increase of surface potential. The discussed example of registering of the hiss gives the confidence of the possibility to use the ISS as a base for the monitoring of this and other geophysical phenomena in the ionosphere.

The study of nature and the intensity of low-frequency noise (~ <3 kHz) and E and B peaks in shadowed areas of the orbit requires additional information on the operation modes of all systems of the ISS. An important factor in confirming the reliability of data about the electromagnetic environment in the surrounding surface layer of ISS is a good long-term repeatability of these events, as shown in Fig. 4.

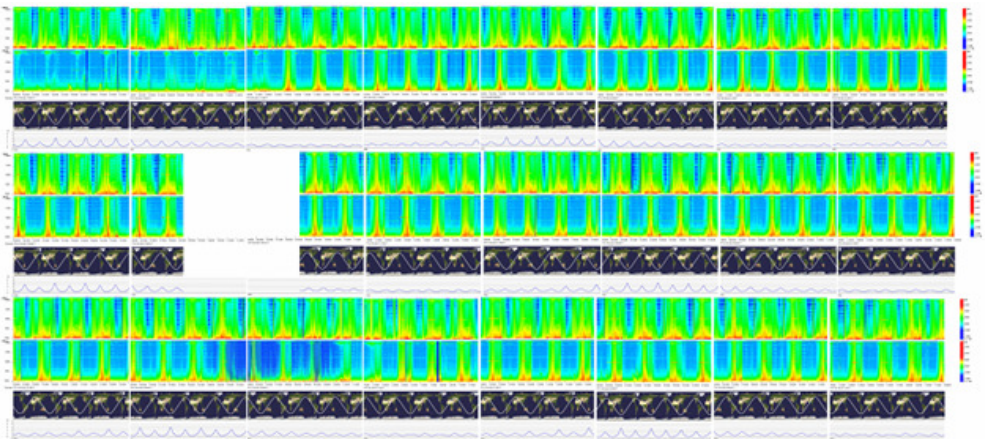

Figure 4. "Obstanovka (1 stage)". An example of the electromagnetic environment monitoring 15-19 June 2013. The overall picture is composed of 6-hourly data, similar to Fig. 2.

It is important to note that the data in Figure 4 are obtained at different geomagnetic activity (June 15, Kp sum = 7,0; June 16, Kp sum = 3-; June 17, Kp sum = 5+; June 18, Kp sum = 7-; June 19, Kp sum = 8+) and at various geomagnetic latitudes (L = 1.2 - 6.0).

Micro-satellite "Chibis-M", 2012-2014 http://chibis.cosmos.ru .

As presented above, the ISS, as a very large long-lived spacecraft has several important advantages for long-term monitoring in the ionosphere, and a number of specific features in different parts of the orbit were registered. ISS was also used for the launch of the "Chibis-M" microsatellite (fig. 5, left). This was realized after the separation of the "Progress" space vehicle from the ISS: it raised its orbit altitude using residual fuel and delivered microsatellite at the circular orbit with the height 513 km and the same inclination = 52 deg like of the ISS.

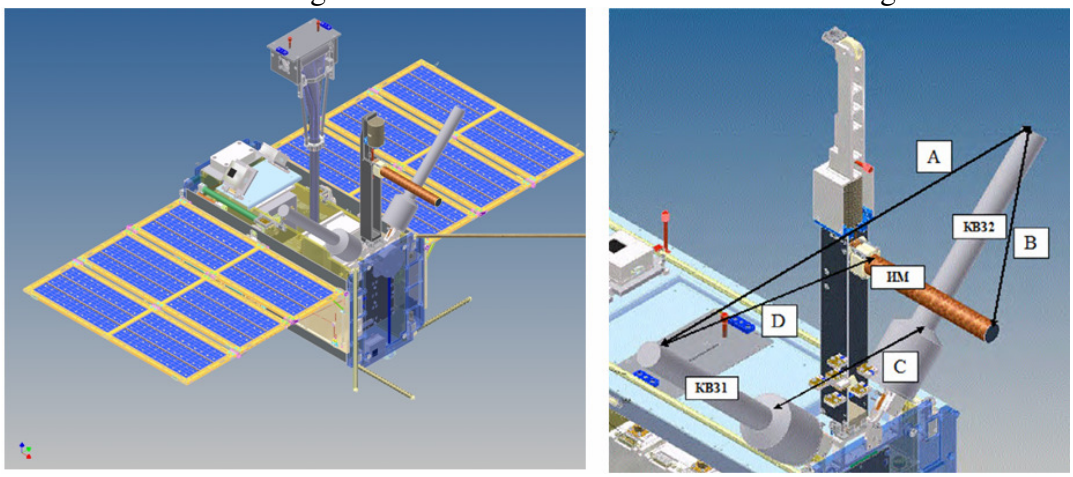

Figure 5. Left - "Chibis-M" general view; right - MWC sensors.

In Fig. 5, left, the MWS sensors are shown: KB31 and KB32 – combined wave probes WP [5], each containing inside one component induction coil magnetometers (Bx and By components correspondingly), ИМ – induction magnetometer, Bz component. The sensors dimensions may be estimated from the onboard configuration: A = 597 mm; B = 376 mm, C = 250 mm, D = 299 mm. With these dimensions the outer surfaces of WPs are forming the electric channel Ex meter with the base 42 cm only. As the flight results showed, this allowed nevertheless getting Ex channel sensitivity threshold about 1 mcV/m.

The synchronously registered data of the microsatellite "Chibis-M" which studied the electromagnetic waves using the same MWC [10] and of the experiment "Obstanovka (1 stage)" are given in Fig. 6.

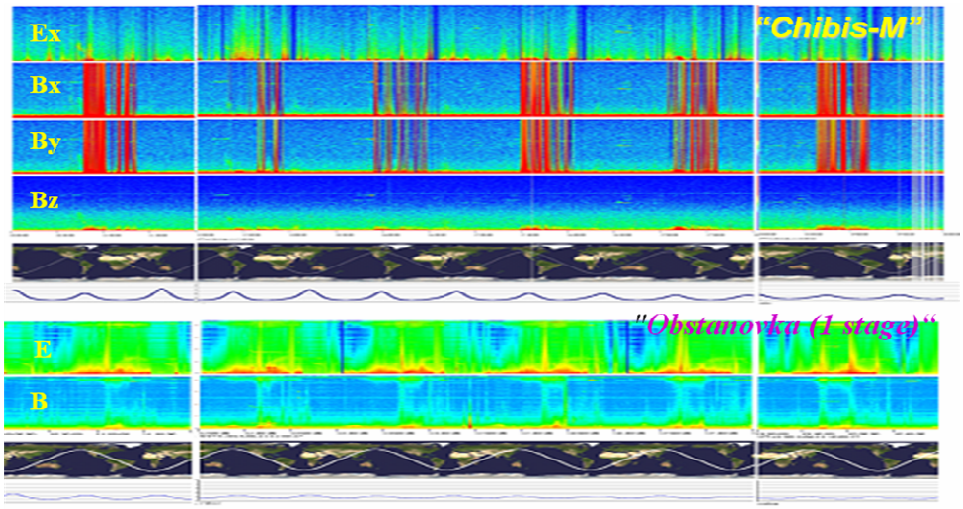

Figure. 6. Synchronous data from "Chibis-M" and "Obstanovka 1st stage" from 2013.06.11 10:00-20:00 (UT+3). Top to down: "Chibis-M": Ex, Bx, By, Bz – frequency 0.01-39kHz;"Obstanovka (1-st stage)": E, B – frequency 0.01-23кГц.

Synchronous data of "Chibis-M" and "Obstanovka (1-st stage)" in Figure 5 are presented for *2013.06.11 (10:00-20:00, UT+3)*. The synchronism of processes at the shadowed and illuminated parts of the orbit may be observed. Important factor is that the "Chibis-M" data have considerably lower noise level [11]. The obvious drawback of this is the presence of intense radiation (red vertical lines) in the channels Bx and By as placed much closer to the microsatellite surface than Bz channel (see Fig.5), determined as electromagnetic interference from the gyroscopes of the microsatellite guidance system, which switched on periodically.

The data presented in Figure 7 confirmed low level of electromagnetic noise of "Chibis-M" sensors, what allowed registration of geophysical processes, including sub-auroral low-frequency electrostatic noise in both hemispheres and the sub-auroral hiss recorded in the disturbed geophysical conditions in the Northern hemisphere [12].

A kind of applied research can be the study of propagation of recorded signals of the radio navigation VLF transmitters (Fig. 7, the horizontal cuts at fixed frequencies).

The data presented in Figure 7 confirmed low level of electromagnetic noise of "Chibis-M" sensors, what allowed registration of geophysical processes, including sub-auroral low-frequency electrostatic noise in both hemispheres and the sub-auroral hiss recorded in the disturbed geophysical conditions in the Northern hemisphere [12].

A kind of applied research can be the study of propagation of recorded signals of the radio navigation VLF transmitters (fig. 7, the horizontal cuts at fixed frequencies).

Satellite "VERNOV", 2014

In the experiments "Chibis-M" and "Obstanovka (1-st stage)" monitoring of electromagnetic parameters using MWC were carried out at sub-auroral (< 52°) and Equatorial latitudes. The "Vernov" spacecraft, onboard of which the RELEC (**R**elativistic **ELEC**trons) experiment was installed, was launched at sun-synchronous orbit with altitude from 640 to 830 km and inclination of 98.4° (Fig. 8). Main goal of this experiment was complex study of Transient Luminous Events (TLE) and Terrestrial Gamma-ray Flashes (TGF) in radio, optical and gamma energy ranges [13]. Investigation of impacts on the upper atmosphere of high energy electron precipitated from the radiation belts, and electromagnetic waves of cosmic and atmosphere origin are supplementary goals of the mission.

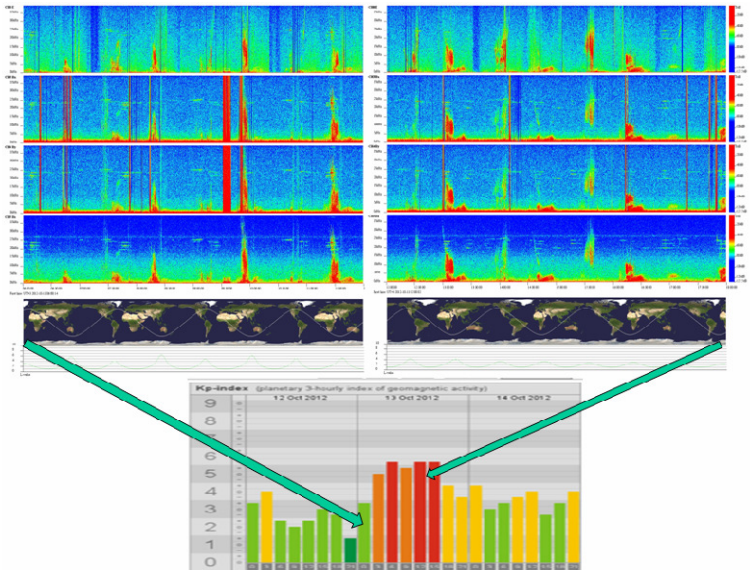

Figure 7. "Chibis-M" data from 2012.10.12-14. Top to down: Ex, Bx, By, Bz (see Fig. 5); projection of the "Chibis-M" orbit; L-parameter; Kp-index.

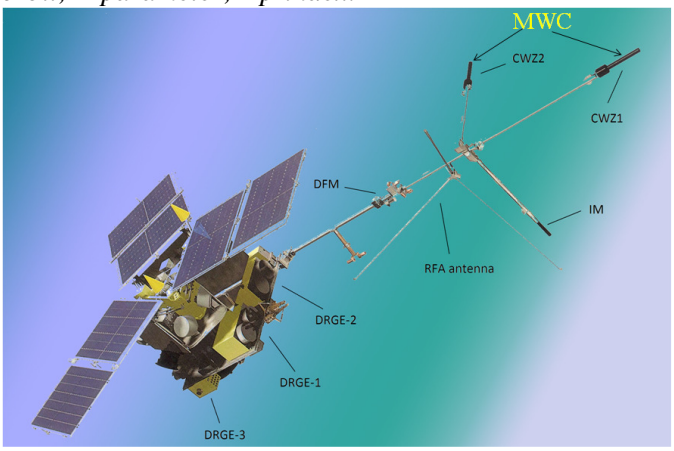

Figure 8. RELEC experiment on-board "Vernov" spacecraft: detectors of X- and gamma-rays of high temporal resolution (DRGE-1 and DRGE-2), detectors of energetic electrons and protons mounted along Cartesian frame (DRGE-3), ultraviolet TLE imager (MTEL), ultraviolet high time resolution detector (DUV), Magnetic Wave Complex (MWC: CWZ1, CWZ2, IM), radio-frequency analyser (RFA).

The high inclination of the spacecraft allowed monitoring in the auroral region and polar cap. A typical example of monitoring in frequency range 0.01-22kHz by the MWC experiment are presented at Fig. 9 for *2014-10-01* and *2014-10-00.*

These data suggest that, despite the placement of sensors MWC (KB31, KB32) on the boom end, the level of electromagnetic noise is significantly higher than in the experiment at a microsatellite "Chibis-M" and even at very large spacecraft like the ISS. Apparently, taking into account the practical identity of MWC equipment in all three experiments, this was because of low electromagnetic compatibility of equipment onboard RELEC, especially noisy were the magnetic component (Bx, By, Bz). However, the data of the electric components E (Fig. 9) are sufficiently close to the data "Chibis-M". Analyzing these data, it is necessary to consider that the orbit of the satellite VERNOV was sun-synchronous, and thus the illumination of the sensors of the MWC was close to permanent.

Monitoring data of the RELEC, as well as by the aforementioned experiments, revealed an intense radiation at sub-auroral latitudes. At auroral latitudes and in the polar cap radiation is more broadband. A single short-term narrow-band radiation at frequency of ~5 kHz (Fig. 10, shown by arrows) was observed in polar cap 2014/10/05 03:40 UT.

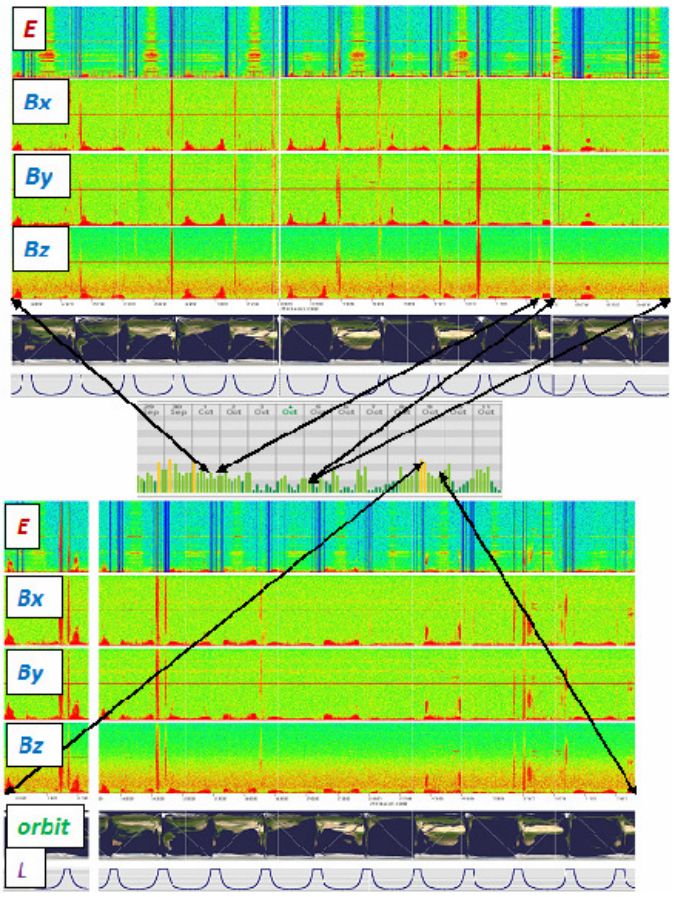

Figure 9. The experiment RELEC. Monitoring of electromagnetic parameters (0.01-22kHz): the top line 2014/10/01 13:40-22:00 UT; the bottom line 2014/10/09 10:18-22:20 UT. Arrows show the values of the Kp index (in the middle) at selected time intervals.

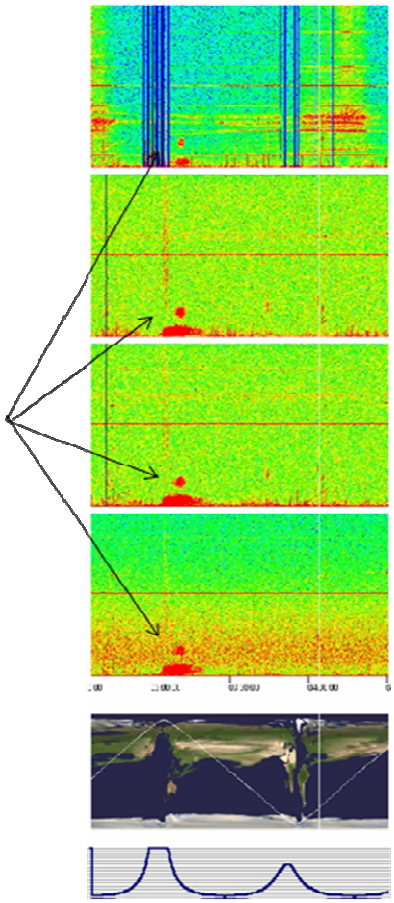

Figure 10. The experiment RELEC 2014/10/05 02:37-04:30 UT. A single short-term narrow-band radiation at frequency of ~5 kHz shown by arrows

Preliminary analysis of monitoring data (fig. 9) shows that in the downturn of geomagnetic activity (reduction of Kp index), the intensity of radiation was also reduced, see the data from 2014/10/01 and 2014/10/09 (top and bottom of Fig. 9). At the same time, a decrease in the intensity of the signals from radio navigation transmitters in the electric E component was revealed that will require special consideration from the practical point of view.

These studies are planned to prolong in frames of the program "Long-term Program of scientific research and experiments planned on the Russian segment of the ISS which is planning 3 space experiments with use of the MWC [14]:

1. ***Micro-satellite "Chibis-AI,*** *2019-2023.*

Its goal is the study of the nature of high-altitude lightning and related processes in the atmosphere and ionosphere on the basis of the microsatellite "Chibis" using the cargo ship "Progress". 2016 - end of phase A, transition to phase B.

2. Experiment «Obstanovka 2-nd stage», *2019-2025.*

The subjects of the study of "Obstanovka 2-nd stage" experiment are:

- Parameters of the electromagnetic situation with the vector measurements in the zone of the installation of equipment.
- Geophysical and anthropogenic processes study in the ionosphere plasma.
- Recommendations regarding the monitoring of geophysical and anthropogenic processes with the use of a method of combined wave diagnostics.

***3. Micro-satellite "Trabant"**, 2019-2023.*

Basic objective mission of the "Trabant" is the development of the electromagnetically clean micro-satellite, which will be integrated into the infrastructure of the RS ISS. Development of MWC for the frequency range of 0.1 Hz – 80 kHz and of the instrument for study of high-frequency fluctuations of the ionospheric plasma concentration is a key scientific tools "Trabant".

Conclusion.

1. *The use of the ISS for monitoring measurements provides an opportunity to investigate short-period and 11-years variations of ionospheric electromagnetic parameters of space weather. The observed anthropogenic impact of the ISS infrastructure is main restricting factor for this.*
2. *Monitoring measurements on the micro-satellites integrated into the infrastructure of the ISS ensure the high spectral - temporal resolution. It is necessary to take special measures to reduce the impact of houskeeping electromagnetic devices, especially of systems for orientation of micro-satellites* [12].
3. *Monitoring measurements using polar orbiting satellites will significantly widen the range of research of electromagnetic parameters of space weather.*
4. *The intensity of the electromagnetic parameters in the sub-auroral regions can serve as nowcasting tool of space weather in the ionosphere.*

References

[1] Märcz, F. et al. 2003. Long-term changes in atmospheric electrical parameters observed at Nagycenk (Hungary) and the UK observatories at Eskdalemuir and Kew //. Ann. Geophys. 21, 2193–2200.

[2] Inan U.S., Slingeland A., Pasko V.P., Rodriges J.V. VLF and LF signatures of mesospheric/lower ionospheric response to lighting discharges // J. Geophys. Res. 1996. V. 101, p. 5219-5238.

[3] Sátori, G., Mushtak, V., Williams, E., 2009. Schumann resonance signatures of global lightning activity // In: Betz, H.-D., Schumann, U., Laroche, P. (Eds.), Lightning: Principles, Instruments and Applications: Review of Modern Lightning Research. Springer, ISBN, 978-1-4020-9078-3.

[4] Ferencz, Csaba et al. Ionosphere Waves Service (IWS) – a problem-oriented tool in ionosphere and Space Weather research produced by POPDAT project // J. Space Weather Space Clim. 4 (2014) A17.

[5] Korepanov, V., Klimov, S. Wave Probe – a new instrument for space research // Geophysical Research Abstracts, Volume 9, 2007, EGU General Assembly 2007, EGU2007-A-00678.

[6] Klimov, S.I. et al. "Obstanovka" Experiment Onboard International Space Station for Space Weather Research // Space Weather Workshop: Space Weather Applications Pilot Project. 16-18 Dec 2002, ESTEC, Noordwijk Netherlands, Proceeding www.estec.esa.int/wmwww/wma/spweather/workshops/spw_w4/proceedings/PaperFinal.pdf

[7] Rothkaehl H. et al. Diagnostics of Space Plasma on Board International Space Station // Article in Beiträge aus der Plasmaphysik 51(2□3):158 - 164 March 2011. DOI: 10.1002/ctpp.201000066

[8] Kirov, B. et al. A remote upgrading of the special software for the Langmuir probe aboard the international Space Station // Solar-Terrestrial Influences, Eleventh International Scientific Conference, Sofia, Bulgaria, 23-25 November 2005 pp 185-188, 2005.

[9] Kirov B. et al. Langmuir probe measurements aboard the International Space Station // «Солнечная и солнечно-земная физика – 2015», Санкт-Петербург, Пулково, 5 – 9 октября, 2015 http://www.gao.spb.ru/russian/publ-s/conf_2015/conf_2015.pdf c. 205-208

[10] Zelenyi, L.M. et al. Academic microsatellite "Chibis-M"// Cosmic Research, 2014, 52, (2), p. 87–98.

[11] Klimov, Stanislav et al First results of MWC SAS3 electromagnetic wave experiment on board of the Chibis-M satellite // Advances in Space Research 54 (2014) 1717–1731.

[12] Klimov, Stanislav.I. et al. Implementation of a micro-satellite program in the infrastructure of the Russian segment of the International Space Station // J. Aeronaut Aerospace Eng 2016, 5:2(Suppl), p. 33.

[13] Panasyuk, M.I. et al RELEC Mission: Relativistic Electron Precipitation and TLE study on-board small spacecraft // Adv. In Space. Res. 12/2015.

[14] Klimov S.I. et al. Microsatellite "Chibis-M" (25.01.2012 – 15.10.2014). Results, lessons and prospects // Small Satellites for Earth Observation. 10th International Symposium of the International Academy of Astronautics (IAA), Berlin, April 20-24, 2015. Editors: Rainer Sandau, Hans-Peter Roeser, Arnoldo Valenzuela. Wissenschaft und Technik Verlag, Berlin, p. 181-184.

Proceedings of
Eighth Workshop "Solar Influences on the Magnetosphere, Ionosphere and Atmosphere"
Sunny Beach, Bulgaria, May 30 - June 3, 2016

Are geomagnetic disturbances and pulsations really hazardous?

N.G. Kleimenova [1,2]

[1] Schmidt Institute of the Physics of the Earth RAS, Moscow, Russia
[2] Space Research Institute RAS, Moscow, Russia

Abstract

Different types of geomagnetic disturbances including geomagnetic pulsations represent an important factor of the space weather which may seriously impact on the biosphere and human health. This problem is widely discussed more than 50 years surrounding by supporters and sceptics. The Interest to this problem grew after the discovery of the biogenic magnetite in different leaving systems and in the human body. However, there are a lot of conflicting opinions and myths. Some people believe magnetic storms as a main hazard for the human health. The morphology and the seasonal variations of magnetic storms accompanied by different geomagnetic pulsations are considered. It was shown that the magnetic storms are hazardous not always. The strongest negative effects of magnetic storms are observed in the winter season, while in summer such effect became very weak. It is found that one of plausible agents which could have a negative impact on the health is a specific type of geomagnetic pulsations (Pc1) with the periods of few seconds coinciding with the human heartbeat. The relationship between the occurrence of geomagnetic Pc1 pulsations and infarction has been found, but at different latitudes this effect seems to be different.

Introduction

It is generally accepted that the Earth' magnetic field is one of the necessary conditions for the biosphere and human life emerging and developing. Change of the solar and geomagnetic activity can influence to different processes in the Earth atmosphere, including the climate, biosphere [e.g., Adey 1993, Chibisov et al 1995], and even the human health [e.g., Baevsky et al., 1994; Watanabe et al 1994, Breus et al 1995, Gurfinkel et al 1995]. Different types of geomagnetic disturbances including geomagnetic pulsations represent an important factor of the space weather which may seriously impact on the biosphere and human health. This problem is widely discussed more than 50 years surrounding by supporters and sceptics [e.g., Lipa et al., 1976]. The interest to this problem grew after the discovery of the biogenic magnetite in different leaving systems and in the human body [e.g., Kirschvink and Gould, 1981]. However, there are a lot of conflicting opinions and myths. Some people believe magnetic storms as a main hazard for the human health.

Myocardial infarctions and geomagnetic disturbances

It was established that the human heart and cardiovascular system could be the main targets of the negative influence of the solar and geomagnetic activity [e.g., Watanabe et al 1994, Breus et al 1995, Gurfinkel et al 1995]. Here we present results [Ivanova et al., 2002] of the statistical study the time variation of the mortality (monthly numbers) from heart attack (myocardial infarction) in Bulgaria (Fig. 1, left panel) in comparison with the simultaneous variations of solar (Wp) and geomagnetic activity (Kp) for period of 26 years data (1970-1995). The mortality increasing can be a result of the population increasing as well as life conditions decreasing.

It is seen that the relationship between the solar and geomagnetic activity and the infarction mortality is absent. However, the infarction mortality demonstrates the strong season quasi-periodicity with the winter maximum and the summer minimum. The right panel of Fig 1 demonstrates the averaged seasonal variation of mortality, the similar for everybody: men, women, urban and villager residents. The strong the winter maximum and the summer minimum is seen.

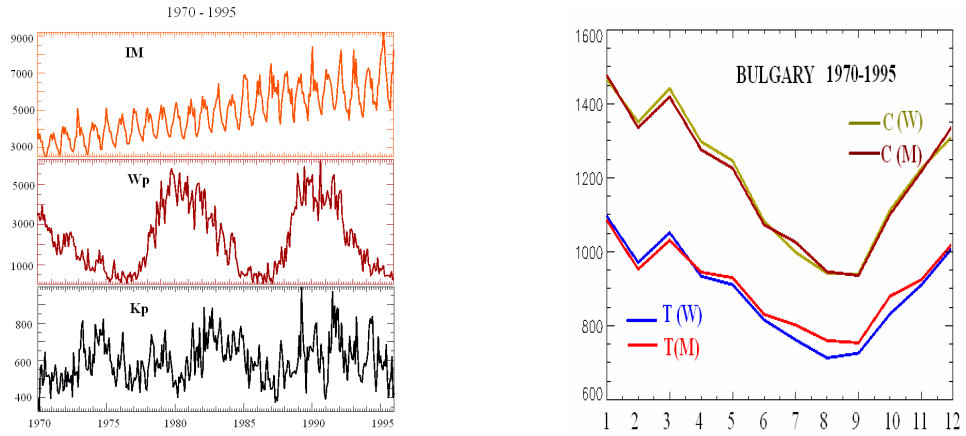

Fig.1. Variations of the infarction mortality (Bulgaria) and solar (Wp) and geomagnetic activity (Kp) for period of 1970-1995 (left panel) and season variations of the mortality in for 16 years; M - men, W – women, T – in towns, C - in the country (right panel).

However, it is well known that the maximum of magnetic storm occurrence is attributes to equinox, not to winter. Thus, we suggest that a biotropic efficacy of the magnetic storms may depend on the season.

The comparison of this data with the ambulance calls in Moscow on the occasion of the myocardial infarction (85,700 events) during 1979--1981 years shows their good agreement (Fig. 2) with the correlation coefficient 0.84.

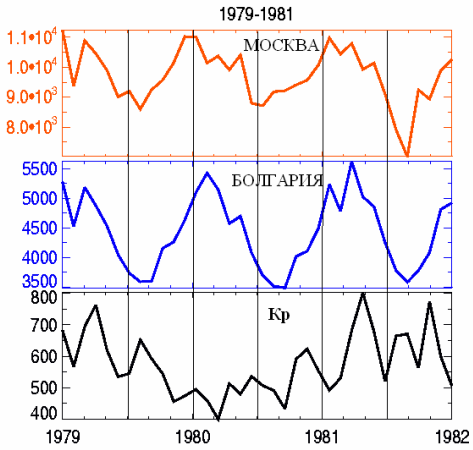

Fig.2. Monthly numbers of ambulance calls for three years (1979 – 1981) in Moscow (red) of myocardial infarctions (85,700 cases) and the myocardial infarction mortality in Bulgaria (blue) and geomagnetic activity (monthly values of the Kp index).

One can see that there is no real agreement between the medical data and geomagnetic activity (Kp).

We analyzed 129 geomagnetic storms with Dst from –50 nT to –250 nT in 1979-1981 (near solar activity maximum) and found that 75 storms were observed in spring/autumn, 32 – in summer, and 22 – in winter. About of 75% of the spring/autumn and about of 95% of the winter magnetic storms were accompanied by the infarction enhancement, but only 3% of the summer magnetic storms accompanied by an infarction enhancement. Thus, all winter storms were biotropic, however, the biotropic of the summer storms was negligible small.

It is necessary to note that the decreasing of the strength of geomagnetic field even during the strongest magnetic storms represents not more than 1-2% of the main Earth magnetic field, i.e. such small variations cannot influence to the human health. Thus, during magnetic storms should present another agent which could effect to the human health. Such agent could be wave geomagnetic phenomena, i.e. geomagnetic pulsations at different periods.

The daytime pulsations (pulsations continues – *Pc*) are divided into *Pc1* (T=0.2-5.0 c), *Pc2* (T=5-10 c), *Pc3* (T=10-45 c), *Pc4* (T= 45-150 c), *Pc5* (T=150-600 c). The average pulsation amplitudes increase with increasing of the periods. The night-time (pulsations

irregular –Pi) are divided in *Pi1* (T=1-40 c), *Pi2* (T=40-150 c) and *Pi3* (T>150 c). It can be suggested that one of critical factors which affect a human cardiovascular system could be geomagnetic *Pc1* pulsations (Fig. 3) having the frequency comparable with frequency of heart rate beatings.

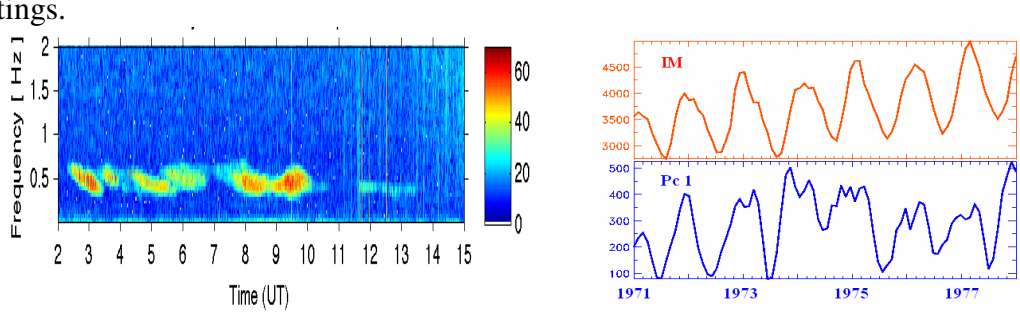

Fig.3. An example of typical Pi1 pulsation spectrogram (left panel) and the monthly variations of infarction mortality (IM) in Bulgaria and simultaneous monthly duration of mid-latitude geomagnetic pulsations Pc1 (right panel).

The frequency range of Pc1 geomagnetic pulsations is 0.5 – 2.0 Hz with the amplitudes from 10 to 100 pT. The diurnal occurrence maximum of these pulsations is observed at 00 - 06 MLT with the duration –from several minutes to several hours. Pc1 pulsations are typical for the recovery phase of magnetic storm. Many authors show that a number of events of Pc1 pulsation occurrence significant increases in the winter time. The typical spectrogram of Pc1 pulsations is given in Fig. 3 (left panel).

The comparison of the variation of the mortality from infarctions in Bulgaria (IM) and the monthly duration of geomagnetic pulsations Pc1 at the middle latitude station Borok presents in Fig.3 (right panel) for the period of 7 years. The similar season variations of IM and Pc1 are seen.

We also found that the different magnetic storm phases demonstrated the different MI influence. As usually, the storm main phase was not accompanied by the MI increasing, except the events when the storm main phase was developed on the recovery phase of the previous storm. The most part of the storm associated MI increasing was observed during the storm recovery phase as well as Pc1 geomagnetic pulsations.

Another possible agent of magnetic storm "negative" influence could be the Pc5 geomagnetic pulsations (T~ 3-10 min, f = 2-7 mHz) due to their high temporal gradient of magnetic field, as it was suggested by Kleimenova and Troitskaya (1992). However, the possible "negative" influence of Pc5 pulsations on sick persons did not investigated till now.

Discussion

Apparently, due to life evolution, the living organisms (except sick persons) should be adopted to the typical magnetosphere wave phenomena; however, non-typical events could give an unexpected respond. It is shown that not every magnetic storm is bio-effective, the magnetic storm bio-efficacy does not depend on the storm intensity as well as bio-efficacy of geomagnetic pulsations does not depend on their amplitudes. It is shown that the strongest negative influence of the magnetic storm wave disturbances on the sick organisms is observed in the winter time and in the storm recovery phase.

We suggest that summer minimum of the cardio-vascular system disease could be due to availability of some physiological factors making human organisms stronger in summer than in winter. One possible reason of the infarction seasonal effects could be the seasonal variations of the pineal gland hormone (melatonin) production [Sakotnik et al., 1999]. The melatonin is well known as a multifunctional key regulator of the circadian rhythms [Arend, 1995].

Summary

It was shown the existence of the strong season variations of the myocardial infarction at the middle latitudes with winter maximum and summer minimum which does not coincided with the season variation of solar and geomagnetic activity. The seasonal variations of myocardial infarctions at the middle latitudes (Moscow and Bulgaria) show a great similarity. But at subauroral latitudes (Yakutsk), in the seasonal variations of the myocardial infarctions, there are the addition maxima associated with the geomagnetic activity maxima.

One of the biotropic factors affected to the human cardio system could be geomagnetic Pc1 or Pi1 pulsations with frequencies comparable with the frequency of human heart beatings.

It was found that in summer, even very strong magnetic storms and Pc1 pulsations are not biotropic, while in winter, even small and moderate magnetic storms became biotropic.

The sensitivity of human organism is, probably, violated during the winter time due to instability related to the lack of luminosity which regulated the production of the pineal gland hormone – melatonin.

Acknowledgements.

The paper was partly supported by the Program No 18 of the Presidium of the Russian Academy of Sciences (RAS).

Referances

Adey, W.R., Biological effects of electromagnetic fields, J. Cell Biochemistry 51 (4), 410–416, 1993.

Arend, J. Melatonin and the mammalian pineal gland London, Chapman and Hall, 331 p, 1995.

Baevsky, R.M., Petrov, V.M., Cornélissen, G. et al. Meta-analyzed heart rate variability, exposure to geomagnetic storms, and the risk of ischemic heart disease, Scripta medica, 70, 99–204, 1994.

Breus, T., Cornelissen, G., Halberg, F., and Levitin, A.E. Temporal associations of life with solar and geophysical activity, Ann. Geophys., 13, 1211–1222, 1995.

Chibisov, S.M., Breus T.K., Levitin A.E., and Dragova G.M., Biological effects of planetary magnetic storms, Biofizika, 40, 959-968, 1995.

Gurfinkel, Yu.I., Liubimov, V.V., Oraevsky, V.N, Parfenova, L.M., and Yuriev, A.S., The effect of geomagnetic disturbances in capillary blood flow in ischemic disease patients Biofizika, 40, 793-799, 1995.

Ivanova, P., Kleimenova, N.G., and Gamburtsev, A.G., Myocardial infarction mortality in Bulgaria, Atlas of the time variations in natural, anthropogenic, and social processes. Moscow, Yanus-K, 3, 561-563, 2002.

Kirschvink, J.L., and Gould, J.L. Biogenic magnetite as a basic for magnetic field detection in animals, Biosystems, 13, 181–201, 1981.

Kleimenova, N.G., and Troitskaya, V.A., Geomagnetic pulsations as one of the ecological factors of the environment, Biophysics 37(3), 429-338, 1992.

Kleimenova, N.G., Kozyreva, O.V., Breus, T.K., and Rapoport S.I., Pc1 geomagnetic pulsations as a potential hazard of the myocardial infarction, J. Atmos. Space. Terr. Phys. 69 (14), 1759-1764. 2007.

Lipa, B.G., Sturrock, P.A., and Rogot, G., Search for correlation between geomagnetic disturbances and mortality, Nature, 259 (5541), 302–304, 1976.

Sakotnik, A., Liebman, P.M, Stoschitzky, K. et al. Decreased melatonin synthesis in patients with coronary artery disease, Eur. Heart J., 20, 1314–317, 1999.

Watanabe, Y., Hillman, D.C., Otsuka, K. et al. Cross-spectral coherence between geomagnetic disturbance and human cardiovascular variables at non-societal frequencies, Chronobiologia, 21, 265–272, 1994.

Proceedings of
Eighth Workshop "Solar Influences on the Magnetosphere, Ionosphere and Atmosphere"
Sunny Beach, Bulgaria, May 30 - June 3, 2016

Application of new mathematical methods of data processing to study solar-wind-magnetosphere interactions: a case study

N.R. Zelinsky [1,2], N.G. Kleimenova [2,3], R.Y. Arkhipov [1]

[1] Data Analysis Center under the Moscow Government, Moscow, Russia
[2] Institute of Physics of the Earth, Russian Academy of Sciences, Moscow, Russia
[3] Space Research Institute, Russian Academy of Sciences, Moscow, Russia

Abstract

Some new methods of the discrete mathematical analysis (DMA) were applied to study the wave-like disturbances in the solar wind and Interplanetary Magnetic Field (IMF) and its magnetosphere effects. The multi-station ground geomagnetic data collected from the Scandinavian IMAGE magnetometers chain, spaced from the polar to middle latitudes, have been used in the analysis. The geomagnetic disturbances during the main phase of the strong magnetic storm on 22 June 2015 have been studied. The original row magnetic digital data as well as the solar wind and IMF data were previously filtered by applying the sixth order Butterworth filter for the analysis of the irregular Pi3 (2-7 mHz) geomagnetic pulsations. To study the occurrence of wave bursts (the anomalies in the term of DMA analysis) in the solar wind and IMF and at the ground stations, we use the DMA method of the Generalized Variance of the covariance matrix eigenvalues. The algorithms of this new mathematical method of the data processing have been developed. It is shown that the combination of the mathematical methods such as the Generalized Variance estimation with the econometrics cointegration and the Granger causality test can be a useful tool in the investigations of the solar-terrestrial interaction. Some new Pi3 pulsation behavior was established due to applying these new mathematical methods. It was shown, that, the strong bursts of Pi3 which are not seen in the initial magnetograms, occurred near 20 UT (23 MLT) at high latitude ground-based stations (at 67-75□ geomagnetic latitude) under the IMF Bz>0. The second Pi3 burst was observed in the morning at 02-05 UT (05-08 MLT) at the auroral and subauroral geomagnetic latitudes (64-58□) under the IMF Bz<0. It was established that the solar wind density (Np) fluctuations can influence on the Pi3 behavior with the time lag of a few minutes. However, the relationship between the IMF Bz and By fluctuations and ground-based Pi3 pulsation bursts did not found.

Introduction

Nowadays there is a huge of deal of observed geomagnetic data collected by multi-stations ground-based observations. One of the actual problems becomes the developing different mathematical methods of their analysis. We try to apply some of methods of the discrete mathematical analysis (DMA) to study the characteristics of the geomagnetic pulsation. First at all, the original row magnetic digital data have been filtered in the given frequency range to extract the of pulsation bursts. Here we applied the sixth order Butterworth filter. Some new methods of the discrete mathematical analysis (DMA) were applied to study the wave-like disturbances (anomalies) in the solar wind and Interplanetary Magnetic Field (IMF) and its magnetosphere effects. The calculations of the eigenvalues of covariance matrix of the magnetic components in the moving time window have been performed. The covariance matrix calculation is the known procedure for the polarization analysis; the absolute values of the covariance matrix eigenvectors determine the values of the polarization ellipsoid semi-axes (Means, 1972).

The aim of this paper is to apply some new methods of the discrete mathematical analysis (DMA) which algorithms we developed in the paper [Kleimenova et al., 2013], and combine that with the econometrics cointegration and the Granger causality test to analyze of the

irregular Pi3 (2-7 mHz) geomagnetic pulsations during the main phase of the strong magnetic storm on 22 June 2015

Mathematical methods

Discrete mathematical analysis (DMA) is a formalized mathematical approach to simulation in the processing of geophysical data. The practical application of the concept is expressed in the construction of algorithms of pattern identification, fuzzy logic, adaptive filtering, and clustering, which use the same definitions and properties within DMA (Zlotnicki et al., 2005; Bogoutdinov et al., 2007).

In the context of the DMA approach implemented in this work, we developed the magnetogram rectification (i.e., functional taking on non-negative values) by two components: X and Y. Based on the fact that the investigated oscillations have a frequency on the order of 2-7 mHz (which leads to instabilities in the case of direct calculation of polarization with a sampling rate of 16,7 mHz), the chosen rectification for this analysis was a generalized variance (further Gd), calculated as the Kolmogorov mean of the eigenvectors of the covariance matrix of two-component data (Means, 1972).

During the last step we choose a running window width (actually it was 9 min) to calculate covariation matrix and its eigenvalues $\lambda_1(t_i),\lambda_2(t_i)$ for every time stamp t_i (the center of the running window). Functional values are

$$f(\lambda_1,\lambda_2,t_i) = \frac{((\lambda_1(t_i)-\lambda(t_i))^2+(\lambda_2(t_i)-\lambda(t_i))^2)^{\frac{1}{2}}}{2}, \lambda(t_i) = \frac{\lambda_1(t_i)+\lambda_2(t_i)}{2}$$

In further analysis it was found that using this rectification allows for separation of the main features of filtered signals within the selected time interval, while the regulated parameter (window width for the covariance matrix calculation) enables this process to be controlled.

The rectification called "DMA energy" is

$$E(\Delta^k y) = \sum_{j=k-\Delta/h}^{k+\Delta/h} \left(y_j - \bar{y}_k\right)^2, где\ \bar{y}_k = \frac{h}{2\Delta+h}\sum_{j=k-\Delta/h}^{k+\Delta/h} y_j$$

there Δ – time gap, h – sampling rate, y – initial time series. "DMA Energy" is a signal normalized sample variance, calculated in the running window (2Δ + h) width.

The rectification called "DMA energy" is

$$L(\Delta^k y) = \sum_{j=k-\Delta/h}^{k+\Delta/h} |y_{j+1} - y_j|$$

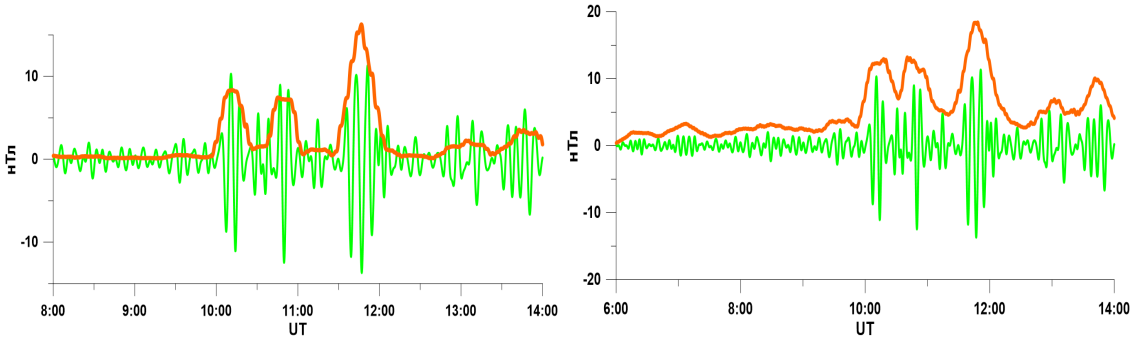

Fig.1. Rectifications "DMA energy" (left panel) and "DMA energy" (right panel).

Then we use Granger causality test [Granger, 1980] to estimate the time lags between ground stations and OMNI IMF data. The Granger causality test is a statistical hypothesis test for determining whether one time series is useful in forecasting another. Ordinarily, regressions reflect "mere" correlations, but Granger [1980] argued that causality in economics

could be tested for by measuring the ability to predict the future values of a time series using prior values of another time series. This method differs from the correlation which is a statistical measure that indicates the extent to which two or more variables fluctuate together. We calculate the Granger causality test

$$X = \{x_1, x_2, \dots, x_T\} \quad Y = \{y_1, y_2, \dots, y_T\}$$

$$E\left((\hat{y}_{T+1} - y_{T+1})^2 \middle| y_1, y_2, \dots, y_T, x_1, x_2, \dots, x_T\right) \leq E\left((\hat{y}_{T+1} - y_{T+1})^2 \middle| y_1, y_2, \dots, y_T\right)$$

According to Granger, if it is so, a causality between X and Y exists. When we have long non-stationary time series, we apply the KPSS test (Kwiatkowski et al., 1992) to make sure that the first differences are stationary. We repeat Granger test with different lags from 0 to 12 until the p-value become less than 0.1. So the optimal lag was the first order in which p-value is significant.

Results of the analysis

We applied the considered mathematical methods for the analysis of the multi-station ground geomagnetic observations during the main phase of the strong magnetic storm on 22 June 2015 (Fig. 2, left panel) under the strong values of the solar wind density (Np). We used the data collected from the Scandinavian IMAGE magnetometers (Fig. 2, right panel) located in the night sector along the geomagnetic meridian MLT=UT+3 from the polar to middle latitudes. Some geomagnetic disturbances are seen at high latitudes around the midnight (21 UT) and in the morning 02-06 UT, i.e. 05-09 MLT) at the auroral (SOD) and subauroral (HAN) latitudes.

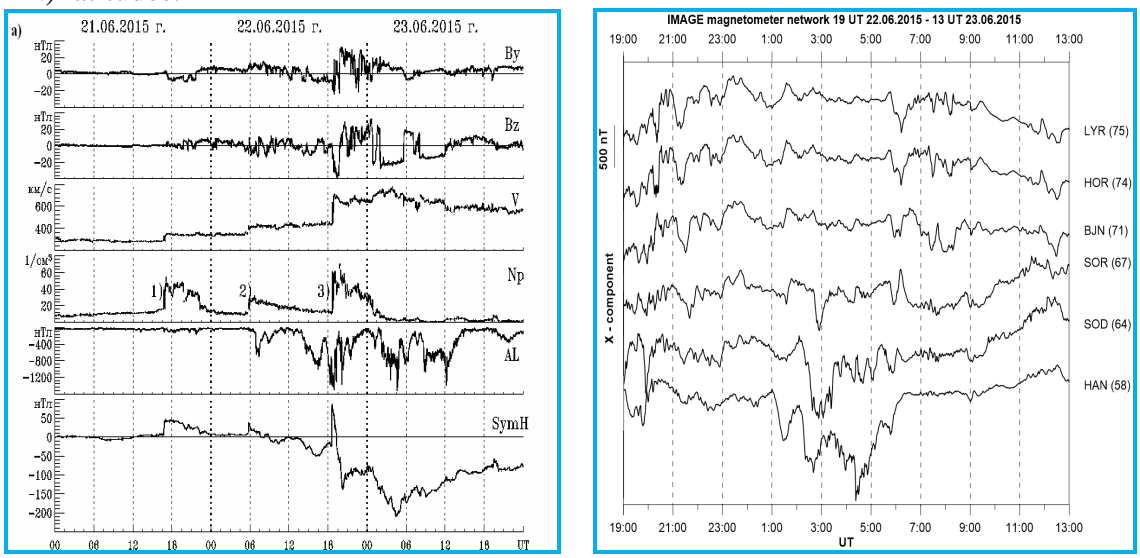

Fig.2. IMF and solar wind data and the AL and SimH indexes (left panel), magnetograms from selected IMAGE stations, geomagnetic latitudes are given in brackets.

We have applied the DMA method of the Generalized Variance of the covariance matrix eigenvalues to the analysis of the geomagnetic Pi3 pulsations (2-7 mHz). The algorithms of this new mathematical method of the data processing have been developed.

The obtained results are presented in Fig. 3. The strong burst of Pi3 was discovered near 20 UT at high latitude stations under IMF Bz>0 and at 02-05 UT at SOD and HAN under IMF Bz<0.

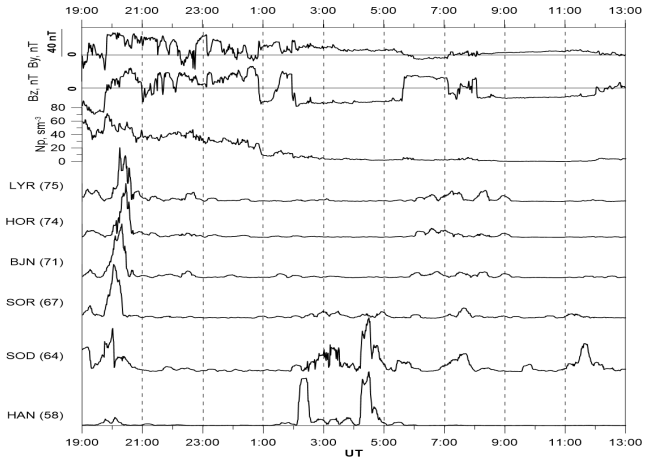

Fig.3. Results of Pi3 geomagnetic pulsation study.

The Granger test of the time lag between the Generalized Variance of Pi3 at different stations and the fluctuations in the solar wind density (Np) demonstrates that the Np fluctuations can influence on the high-latitude Pi3 behavior with the time lag of few minutes.The relationship between IMF Bz and By fluctuations and ground-based Pi3 pulsations did not found.

Summary

The algorithms of new mathematical methods of data processing have been developed based on the conception of the discrete mathematical analysis (DMA). Several functionals taking on non-negative values have been proposed. One of them is the general dispersion of the covariance matrix. It is shown that the combination of the Generalized Variance estimation method with the econometrics cointegration and the Granger causality test can be a useful tool in the investigations of the solar-terrestrial interaction. Some new behavior of Pi3 geomagnetic pulsations was found.

Acknowledgements.

This study was supported by the RFBR Grant № 16-35-00069 (N.Z.) and partly by the Program No7 of the Presidium of the Russian Academy of Sciences (N.K.).

References

Bogoutdinov, Sh.R., Agayan, S.M., Gvishiani, A.D.,Graeva, E.M., Rodkin, M.V., Zlotnicki, J., and Le Muel, J.L., Fuzzy logic algorithms in the analysis of electrotelluric data with reference to monitoring of volcanic activity, Izv., Phys. Solid Earth, 7, 597–609. 2007.

Granger, C. W. J., Testing for causality: A personal viewpoint, J. Economic Dynamics and Control, 2, 329-352, 1980.

Kleimenova, N.G., Zelinsky, N.R., Kozyreva, O.V., Malysheva, L.M., Solov'ev, A.A., and Bogoutdinov, Sh.R. , Pc3 geomagnetic pulsations at near-equatorial latitudes at the initial phase of the magnetic storm of 5 April 2010, Geomagn. Aeron., 53(3), 313-320, 2013.

Kwiatkowski, D., Phillips, P.C.B., Schmidt, P., and Shin, Y., Testing the null hypothesis of stationarity against the alternative of a unit root, J. of Econometrics 54 (1–3), 159-178, 1992,.

Means, J.D., Use of the three dimension covariance matrix in analyzing the polarization properties of plane waves, J. Geophys. Res., 77 (28), 5551-5559, 1972.

Zlotnicki, J., LeMouel, J.L., Gvishiani, A., Agayan, S., Mikhailov, V., and Bogoutdinov, Sh, Automatic fuzzy logic recognition of anomalous activity on long geophysical records. Application to electric signals associated with the volcanic activity of la Fournaise volcano (Rйunion Island), Earth Planet. Sci. Lett., 234, 261-278, 2005.

Proceedings of
Eighth Workshop "Solar Influences on the Magnetosphere, Ionosphere and Atmosphere"
Sunny Beach, Bulgaria, May 30 - June 3, 2016

Ozone Determination by GUV 2511 Ultraviolet Irradiation Measurements at Stara Zagora

Werner R.[1], Petkov B.2, Valev D.[1], Atanassov At.[1], Guineva V.[1], Kirillov A.[3]

[1] Space Research Institute – Bulgarian Academy of Sciences, Stara Zagora Department, Bulgaria
[2] Institute of Atmospheric Sciences and Climate (ISAC), CNR, Bologna, Italy
[3] Polar Geophysical Institute (PGI), Apatity, Russia
E-mail: rolwer52@yahoo.co.uk

Abstract

A ground-based Ultraviolet Radiometer (GUV) 2511, designed to measure the downwelling global solar irradiances at 305, 313, 320, 340, 380, 395 nm wavelengths and in the visible range from 400 to 700 nm was installed at Stara Zagora, Bulgaria in February 2015. The instrument allows obtaining a realistic estimate of the total column ozone (TCO) in the atmosphere. This report presents the first measurement results concerning TCO that has been assessed by comparing the ratio of irradiances registered at 313 and 340 nm, with the corresponding ratio computed trough the Tropospheric Ultraviolet and Visible (TUV) radiation transfer model for different solar elevations and TCO. The results were compared with the TCO amounts provided by the Ozone monitoring instrument (OMI) onboard the Aura satellite and the correlation coefficient between the OMI values and those retrieved by the GUV 2511 surface measurements, both referred to the Stara Zagora station was found to be higher than 0.975.

Introduction

Routinely total column ozone (TCO) observations began with the design of the Dobson-spectrometer in 1924 [1]. After the International Geophysical Year 1957 a global network of ground-based ozone measurements was established mainly consisting of Dobson and Brewer spectrophotometers with a typical spectral resolution of 1 nm approximately. Dobson and Brewer spectrometers are widely used for the calibration of other ground-based instruments and for the validation of satellite ozone measurements. Dobson instruments allow the determination of TCO with an accuracy of 1% in the case of direct solar observations and 2-3% for zenith sky observations [1]. The error of the ozone retrieval by Brewer instruments is about 1% [2]. In the 90-ties broadband filter instruments were developed to increase the global coverage of the measurements. In February 2015 a Ground-based Ultraviolet Radiometer (GUV) 2511 was installed in Stara Zagora. GUV 2511 instruments were designed for measurements of the downwelling global irradiances in six broadband channels and of the irradiance in the visible range from 400 to 700 nm. The instruments allow obtaining of the total column ozone (TCO) in the atmosphere, the determination of the UV-index and the retrieval of the cloud optical thickness. In the paper the methodology to derive TCO is described and the first results are presented.

Brief Description of the GUV 2511 Instrument

The GUV instrument measures the global irradiances at 305, 313, 320, 340, 380, 395 nm with a bandwidth of 10 nm FWHM as well as the Photosynthetically Available Radiation (PAR) irradiance in the visible spectral range from 400 to 700 nm. All channels have an own photodiode with amplifier. A heater blanket placed in the instrument head stabilizes the photodiodes, filters and amplifiers at the temperature of 50°C. A portion of the heat is used to warm the diffuser and to keep it free from ice and snow. Melt water or rain on the diffuser and occluding ring is lead outside by drain holes. The instrument functioning is operated by a controller including the power management, the temperature control and the data transfer via the interface RS232. The main advantage of the GUV instrument series is that they have not

moving components and therefore they work very stably. Moreover the measurements are carried out very fast.

The GUV instrument was installed in February 2015 on the roof of the Stara Zagora Observatory (Fig.1). The observatory is located at 3 km from the City Stara Zagora at an altitude of 430 m.

Brief Description of the OMI-AURA Measurements

The ozone monitoring instrument (OMI) together with other instruments is installed on the Earth observing system (EOS) Aura satellite platform. The Aura spacecraft sun synchronous orbit allows performing measurements over an Earth location approximately at the same mean solar time every day. OMI is an ultraviolet/visible (UV/VIS) nadir solar backscatter spectrometer with a spectral resolution of 0.42 nm in the UV-1 channel (270-310 nm) and 0.45 nm in the UV-2 channel (310-365 nm). The spectrometer provides nearly global coverage in one day with a spatial resolution of 13 km x 24 km [3].

To retrieve TCO from the OMI measurements two different algorithms are used – one of them is based on the TOMS Version 8 algorithm and a second algorithm is based on the Differential Optical Absorption Spectroscopy (DOAS) technique. The satellite OMI ozone data were validated by the help of ground based Brewer and Dobson spectrometers.

Here we used OMI-TOMS like ozone data (OMTO3) to compare with the ozone results of our measurements. The data are gridded in steps of 1 degree by 1 degree and are available at https://ozoneaq.gsfc.nasa.gov/data/ozone/ (OMI-Aura Global Ozone Data). The data were bilinearly interpolated for the Stara Zagora observatory location (Lat = 42.413 deg., Long = 25.633 deg.). The Aura satellite passes over Bulgaria in about 13.30 o'clock local time (LT) with time differences of approximately 50 min. caused by the satellite orbit perturbation and deviations of the apparent solar time from the mean solar time. An additional time difference of approximately 40 min. results from the deviation of the view angle from the nadir direction.

Preliminary Results

From February 2015 to the middle of May 2016 daily measurements with an integration time of 10 sec. were carried out with some interrupts for technical reasons. The irradiance maxima are observed at noon about 12:30 Local time or 13.30 Local summer time. The minimum zenith angle at the summer solstice is 19.25° and at the winter solstice the zenith angle do not exceed 66.12° at the latitude of Stara Zagora. About 70% of the irradiances are concentrated in the time interval of 3 hours before and 3 hours after noon. Fig.1a shows the observed irradiances during days with different cloudiness: for an almost clear day (left), for a day with fast changing of the solar disc cloud cover (middle) and for a day with large cloud fraction (right). Fig.1b presents the irradiances ratios for the same days. The obtained irradiances are much more sensitive against changes of the overhead cloudiness in comparison with the observed irradiance ratios. High frequency variations are obtained for days with very fast changes of the cloudiness, probably connected with Cirrus clouds (in the middle of Fig. 2b). The irradiance variations registered at 340 nm are some more than about 40% of the maximum. For the 313 nm filter the variations achieve about one third of the maximum value at noon. And vice versa, the obtained irradiance ratio is much stable. The ratio varies only about 10%. In the case of strong cloudiness, the variations have a more low frequency character and the irradiance ratios decrease approximately by 0.5, which generates a great error in the TCO determination. Strong cloudiness often is connected to low clouds and raining.

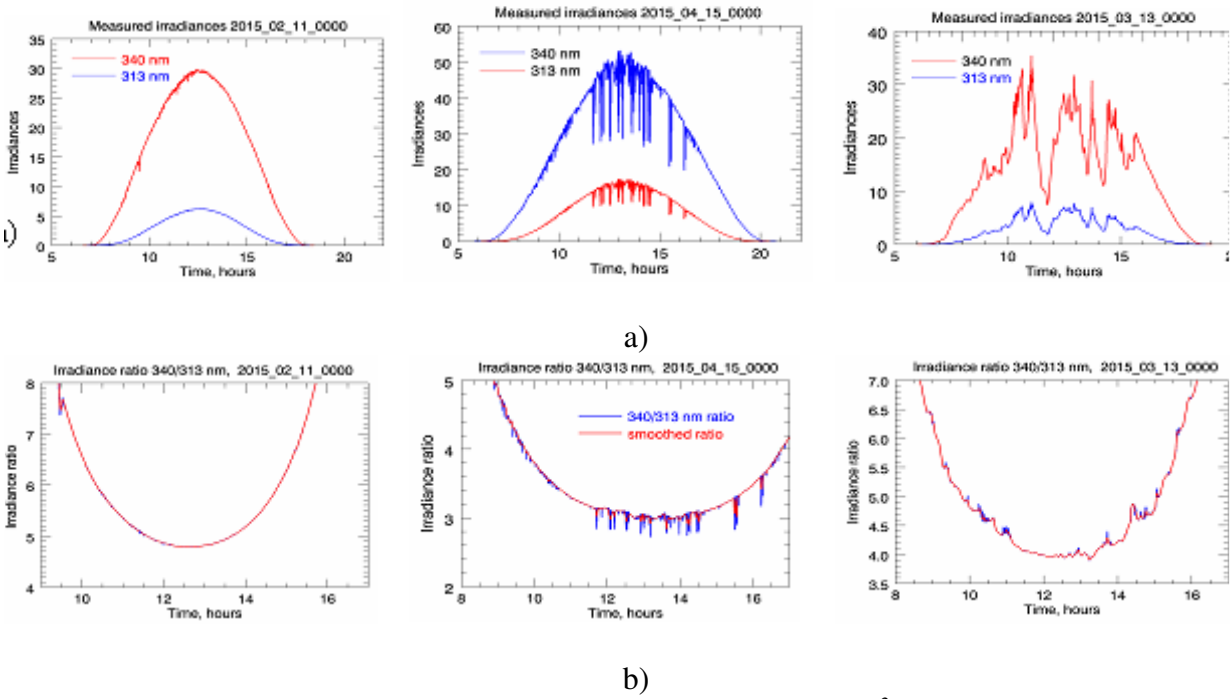

Fig. 1. a) Measured irradiances at 313 nm and 340 nm, given in μmW/(cm^{2}nm), for days with different cloudiness and b) the irradiances ratios (see text).

Methodology of TCO Determination

Data pre-processing

To reduce the cloudiness influence at first the average irradiances at 340 nm from 10:30 to 14:30 LT were calculated. If these radiances were lower than the estimated monthly value (approximately 1/3 of the average monthly mean for cloudless days) then we assumed, that the ozone determination would be wrong because of strong cloudiness. In the second stage the ratios were smoothed by a running boxcare over 17 values, e. g. over 170 sec. Under strong cloudiness the irradiance ratios variations decrease only up to 0.5 (see e.g. the right panel of Fig.4b). Therefore an upper envelope for each daily ratio development was determined. A detailed description of this procedure was given in [4].

The TCO retrievals were successfully carried out for 379 days during the studied time period. Strong cloudiness was established for 54 days. For six days the polynomial shows strong oscillations, which does not allow TCO determination with high accuracy. The number of almost cloudless days was obtained by inspection of the daily progress of the 340 nm irradiation. By this subjective evaluation 103 days were determined as almost cloudless. For 249 days coincidences with OMI measurements were found. 81 of them are cloudless days.

Calculation of Stamnes table for Stara Zagora location

By GUV instruments the global, the diffuse and the direct components of the downwelling irradiation are measured. The ratio of the irradiances at different wavelengths depends on the scattering properties of the air particles and molecules as well as on the solar elevation. Therefore TCO cannot be determined directly by the observed irradiance ratios as it is possible for Dobson and Brewer spectrophotometers for direct solar measurements. To determine TCO from UVA/UVB ratios simulations by radiation transfer models including the UV spectral range are necessary. Here we used Tropospheric Ultraviolet and Visible (TUV) model, version 4.1., developed by Madronich [5]. The spectra were calculated for the Stara Zagora location for different TCO from 0 up to 700 DU with a step of 20 DU and zenith angles from 20° to 90° with a step of 1°. A ground albedo of 0.2 was used as input parameter. We used the climatology mean ozone profile of the U.S. Standard Atmosphere 1976, since the

real ozone profile has a noticeable influence on the ozone retrieval only for large zenith angles [6]. The mean ozone profile of the U.S. Standard Atmosphere 1976 is part of the TUV model library. The obtained spectra were multiplied with the relative filter response functions, approximated by a Gaussian with 10 nm Full Width at the Half-Maximum. The ozone content values were determined by interpolation of the calculated tables for the observed irradiance ratios for the wavelengths 340 nm and 313 nm found by the irradiance measurements and for the zenith angles at 13.30 LT. The zenith angles were calculated by an astronomical algorithm [7]. The irradiance ratios depend on the real filter functions (more correct from the spectral instrument responses). Our GUV instrument is not calibrated against a standard normal (Dobson or Brewer) spectrometer. Therefore we regressed our TCO results with the OMI satellite ones using different wavelength maxima locations for the 313 nm filter in the

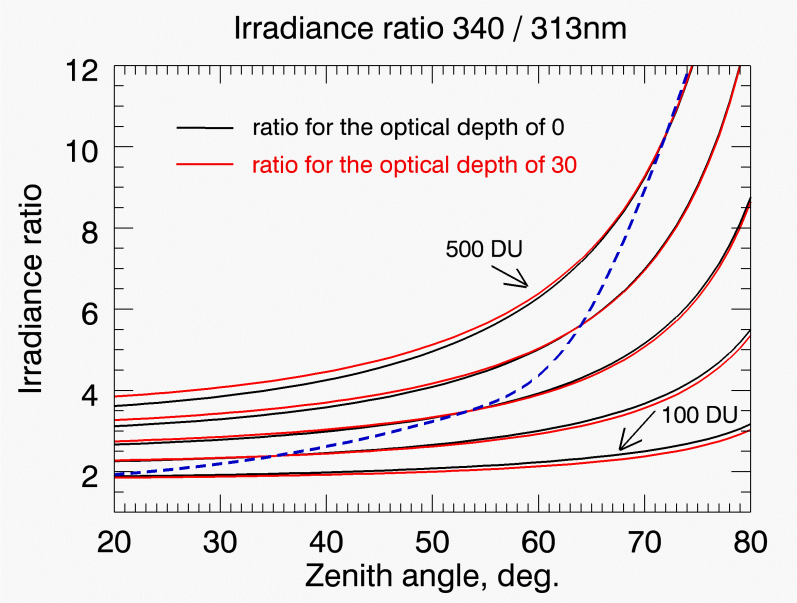

Fig.2. Calculated Stamnes table (ground albedo of 0.2) for two optical depths for the Stara Zagora location. The irradiance ratios are shown for TCO from 100 to 500 DU in steps of 100 DU and for zenith angles from 20° to 80°.

Stamnes table calculation procedure. The best TCO results were obtained with filters centered at 340 nm and at 313.55 nm. The applied here regression doesn't allow us to specify a systematic error between the two measurements – GUV and OMI. As it was mentioned above TCO was determined only in the case when the irradiance at 340 nm was greater than about 30% of the measured irradiance at almost cloudless days. A two third decrease of the 340 nm irradiance is generated by a cloud optical depth of 30. To test the influence of cloudiness up to an optical depth of 30 the Stamnes table was calculated just for this parameter (see Figure 2). If the cloudiness is not taken into account than for smaller zenith angles TCO would be overestimated, but for greater zenith angles an underestimation will follow. The blue line in figure 2 indicate the limit between the over and underestimated TCO values. In the case of small zenith angles (up to 50°) the non-observance of the real mean cloud depth up to 30 a maximal error of the order of 10 DU is to be expected, which is in good agreement with the estimations of Stamnes [6].

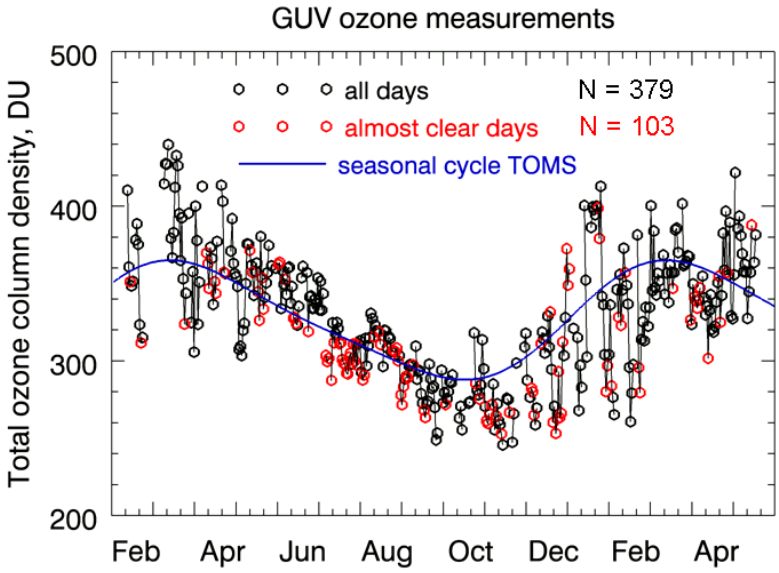

Fig.3. TCO for Stara Zagora determined for the observation period since February 2015 (circles connected by a continuous line for uninterrupted measurements). The TOMS TCO seasonal means are presented by a thick blue line. The TCO values for Stara Zagora in clear days are shown by red dots.

Results

The determined time series of TCO during the time period from the GUV 2511 installation in February 2015 up to the middle of May 2016 is shown in Fig.3. Consecutive daily GUV ozone values are connected by a continuous line. Long interruptions mark periods without data for technical reasons. Interruptions of some days could be a result of bad weather conditions with strong cloudiness. A sensitivity of the results to different albedos between 0.05 and 0.5 was not found. The observed TCO (Fig. 3) follows closely the multi-annual seasonal mean determined from TOMS measurements. An abrupt ozone maximum in spring and a decrease to the minimum in autumn. A higher variability during spring can be seen as it is typical for mid-latitudes. The TCO for almost cloudless days are closer to the TOMS

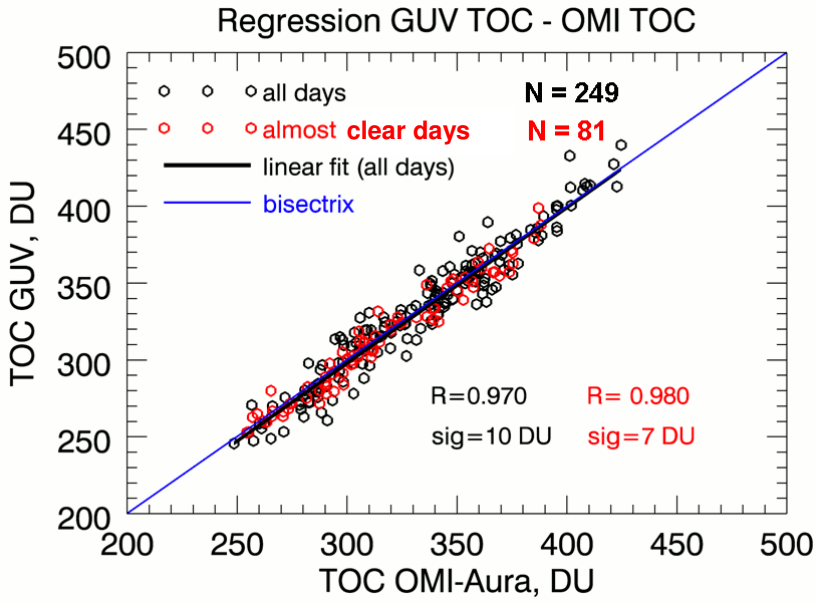

Fig.4. Linear relation between the TCO GUV and the TCO OMI data. The thick black line presents the regression fit.

seasonal mean. Fig. 4 shows both our ground based TCO and the OMI satellite ozone data for days when measurements with both instruments are available. The figure represents the result of the linear regression of the GUV 2511 TCO data against the OMI TCO. It is clearly seen that our observed TCO values reproduce the satellite OMI TCO very well. The slope of the best fit line between GUV and OMI TCO for all days is 1.013 with a 1σ error of 0.031. At the significance level of 0.05 the slope is not distinguishable from 1. The found correlation coefficient is 0.97, meaning that the explained variance of the deviations of the GUV ozone values from the OMI ones is about 0.94. The observed TCO at days almost cloudless are better correlated to the OMI TCO. The explained variance is 0.96. The agreement between the GUV and OMI TCO is very good, however a remained cloud influence is evident. The relative errors of our TCO determinations (related to the OMI TCO) do not exceed 10%. The mean relative standard deviation is about 3.1%.

Conclusions

The retrieved TCO data from ground based UV measurements by the help of the GUV 2511 instrument at Stara Zagora are in good accordance with satellite OMI-Aura data obtained by the TOMS v.8 algorithm. However a systematic deviation of both instrument results cannot be established because our instrument is not calibrated against a Dobson spectrometer or a Brewer instrument. Regardless the measurements allow the determination of daily TCO with an error of 3%, corresponding to about 10 DU. It was found a cloud influence on the TCO. An improvement of the retrieval procedure is envisaged. The instrument has to be calibrated by the help of standard spectrometers. We state, that a high quality ground-based ozone time series are to expect for the Stara Zagora location in the future.

Acknowledgements

The GUV instrument was provided by the project BG161PO003-1.2.04-0053 "Information Complex for Aerospace Monitoring of the Environment" (ICASME) implemented with the financial support of Operational Programme „Development of the Competitiveness of the Bulgarian Economy 2007-2013", co-financed by the European Regional Development Fund and the national budget of the Republic of Bulgaria.

References

[1] Basher R.E. Review of the Dobson spectrophotometer and its accuracy // Global Ozone Res. Monit. -1982- Proj., Rep. 13, World Meteorol. Organ., Geneva, Switzerland, (Available at http://www.esrl.noaa gov/gmd/ozwv/dobson/papers/report13/report13.html)

[2] Kerr J. B., Asbridge I. A., Evans W. F. J. Intercomparison of total ozone measured by the Brewer and Dobson spectrophotometers at Toronto // J. Geophys. Res. -1988- 93(D9) - P: 11129-11140,

[3] Levelt P. F., van den Oord G. H. J., Dobber M. R., M¨alkki, A.,Visser H., de Vries J., Stammes P., Lundell J. Saari, H. The Ozone Monitoring Instrument // IEEE Trans. Geo. Rem. Sens – 2006 - 44 (5) - P: 1093-1101.

[4] Werner R., Petkov B., Valev D.,Atanassov At., Guineva V., Kirillov A. Ozone determination by GUV 2511 measurements at Stara Zagora // Proceedings of the Eighth Scientific Conference with International Participation, Space, Ecology, Safty, Sofia, Bulgaria -2015- P: 19-26 (in Bulgarian).

[5] Madronich S. UV radiation in the natural and perturbed atmosphere // in Environmental Effects of UV (Ultraviolet) Radiation, M. Tevini, ed. Lewis, Boca Raton -1993- P:17–69.

[6] Stamnes K., Slusser J., Bowen M. Derivation of total ozone abundances and cloud effects from spectral irradiance measurements //Appl.. Optics -1991- 30(30)- P:4418-4426.

[7] Meeus J. Astronomische Algorithmen // Johann Ambrosius BarthVerlag, Leipzig-Berlin-Heidelberg- 1993.

Proceedings of
Eighth Workshop "Solar Influences on the Magnetosphere, Ionosphere and Atmosphere"
Sunny Beach, Bulgaria, *May 30 - June 3, 2016*

Intercosmos Bulgaria-1300 - Electric Field Generation in the Magnetotail

Podgorny I. M. [1], *Minami S.* [2], *A. I. Podgorny A. I.* [3]

[1] Institute of Astronomy RAS, Moscow, Russia;
[2] Osaka City University, Osaka, Japan;
[3] Lebedev Physical Institute RAS, Moscow, Russia
E-mail: podgorny@inasan.ru

Abstract

Measurements of the space craft IKB-1300 have shown that the generator of field-aligned currents is located in the geomagnetic tail, where the earthward electric field is created. Two-fluid MHD analysis of the plasma behavior in the current sheet (CS) explains that the electric field generation is made by the Hall effect. Connection of the pair of opposite directed field-aligned currents occurs in the ionosphere, and the westward electrojet is located between this pair of field-aligned currents. It is pointed out here that the idea to explain the current generation in CS by the drift of particles in electric and magnetic fields of the tail, in which the origin is independent from the solar wind, cannot be justified. For such an approach, the magnetic field configuration represents the closed system which does not depend on the solar wind, and the stable electric field exists due to the temperature gradient across the tail. Such temperature gradient existance contradicts to the assumption of the collisionless conditions. The generator of the current in the tail CS is localized at the interface between the solar wind plasma flow and the tail magnetic field. The generated current is closed in the tail CS.

Introduction

The geomagnetic tail is formed at interaction between the solar wind and the magnetic field of the Earth. The force of plasma flow (solar wind) extending lines of the magnetic field is applied to the interface, where the electric generator is located. The current generated in the tail lobe boundaries is closed in the current sheet (CS) separating the magnetic field lines of an opposite direction. Two independent closed circuits are formed as shown in fig. 1a. These currents can be overlapped, creating of current distribution with a single maximum in the central plane (fig.1b) of CS. Conditions of overlapping currents, I_1 and I_2, are difficult to formulate. Results of [1] show that two maximum currents are observed at the very high magnetic fluxes in the tail.

The strong temperature gradient across the sheet ($T_{e\ max}$ ~ 1 keV) and the earthward plasma ejection show the fast magnetic energy dissipation. An important feature of CS is the existence of a normal magnetic field component. The CS is not a neutral line. The force of the magnetic tension can be compensated by the pressure gradient along the sheet and mainly by inertia of ions. If the current in CS is transferred by electrons, the force of a magnetic tension accelerates electronic gas. The electric charge separation takes place. Ion acceleration to the Earth occurs by the electric field of the formed space charge. Plasma in quasi stationary state is flowing in CS in a vicinity of the X-type singular line, where the magnetic field lines are reconnected. Magnetic energy released by the reconnection is used for the plasma heating in CS and acceleration to the Earth. The compensation of the reconnected magnetic flux apparently occurs, when the southward magnetic field component in the solar wind appears. The magnetic energy sharply decreases during a substorm because of the reconnection rate increasing.

The Earthward Electric Field in the Geomagnetic Tail

The Soviet-Bulgarian spacecraft IKB-1300 was launched in August 7, 1981 with a polar circular orbit at the altitude of 900 km [2, 3]. Three-axis stabilization is supplied for the unique possibility of measurements of three components of the electric and magnetic fields, and the plasma velocity. The tip - tip distance of electric field sensors was 7.5 m. X – axis is directed along the spacecraft velocity; Z - axis is directed upward normal to the Earth surface. In the auroral regions, the Z- axis almost coincides with a magnetic field line. The electron temperature, the fluxes of fast electrons, the electron spectrum, and the atmosphere luminosity in several spectral lines are also measured. The measured value of the electric field component perpendicular to the Earth magnetic field is controlled by plasma drift velocity measurements in the XY-plane.

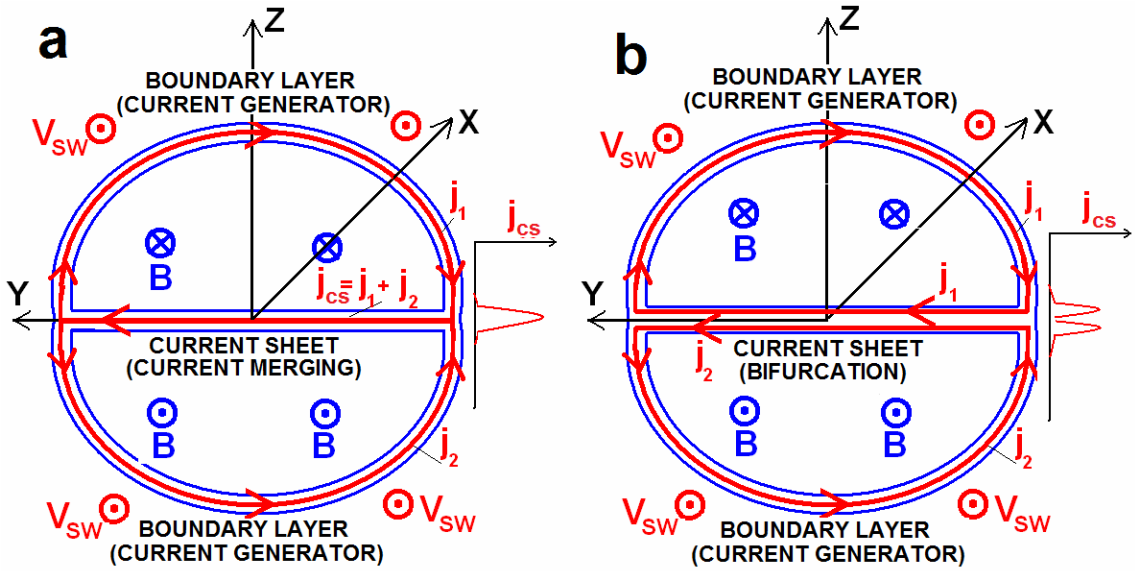

Fig.1. Two different models of the electric circuit system in the geomagnetic tail. The CS is a dissipative element of the electric circuit.

Electric and magnetic field measurements during the crossing of the pair of field-aligned currents at the night side region are as shown in fig. 2, when the chain of IZMIRAN magnetic stations has demonstrated an enhancement of the westward electrojet. This successful coincidence of circumstances occurred on December 21, 1981. The measured electric field E_z normal to the Earth has been very small, and the B_z magnetic field component has not been disturbed. The main upward and downward field-aligned current (FAC) layers in the night sector are recorded. The increasing magnetic field $\Delta\mathbf{B}$ is situated in the plane perpendicular to the Earth magnetic field (X-Y plane). The $\Delta\mathbf{B}$ is located between the upward (at lower latitude) and downward (at higher latitude) FAC layers. The angle between the normal to the FAC layer and the X-axis is arc-tan $(\Delta B_X/\Delta B_y) \sim 50^o$. The electric field between the opposite directed FAC is revealed. This electric field is directed perpendicular to opposite directed FAC layers. The total potential drop exceeds ~10 kV. The direction of the electric field corresponds to the closing upward and downward currents in the ionosphere.

However, electric field distribution between the upward and the downward FAC layers shows asymmetry in the north-south direction. The maximum electric field is shifted to the downward current. Such distribution is a consequence of local increasing of the Pedersen conductivity of the ionosphere in the region of the upward current due to the electron precipitation. Electrons are accelerated in the upward FAC to the Earth somewhere above the spacecraft height (900 km). The electron flux produces aurora and neutral particle ionization in the ionosphere. The Pedersen integrated height conductivity is increasing [4] in the

precipitation region with electron energy flux according to $\Delta_{\sum \mathbf{P}} = 4.7\times10^{12}$ W cm s^{-1}. Here W in erg cm^{-2} s^{-1}. The increasing ionospherice conductivity in the region of the upward FAC produces redistribution of the potential drop. So, the maximum electric field is shifting to the downward current. In the region of the upward current, the weak upward electron flux is also observed. Apparently these electrons appear due to the scatterings by the ionospheric plasma.

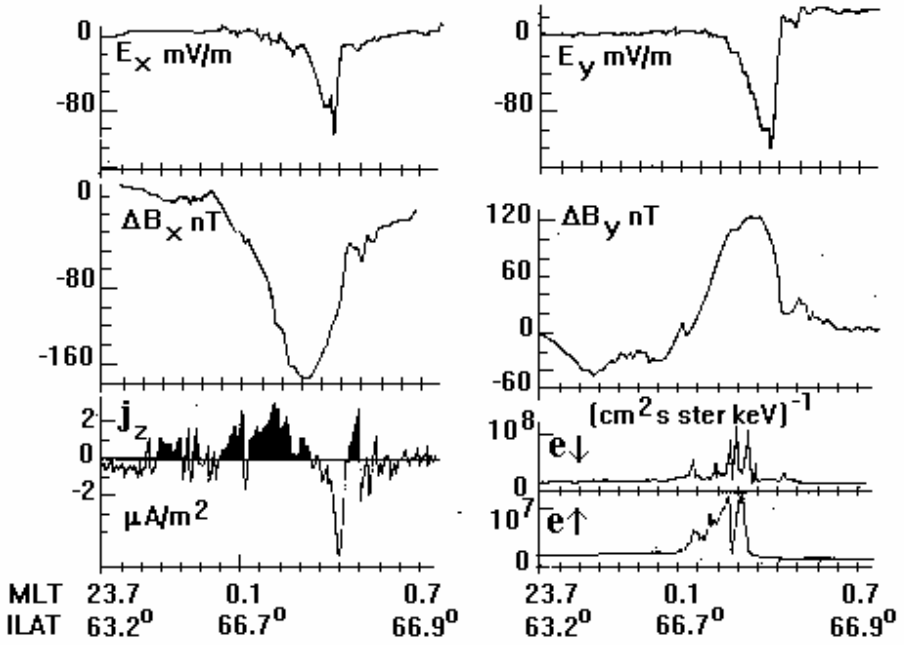

Fig.2. Electric and magnetic fields, current density, and electron flux at crossing field-aligned currents by the spacecraft.

The direction of the electric field between upward and downward current layers shows that field-aligned currents are generated in the CS of the geomagnetic tail. Such generation demands the appearance of the earthward electric field in the tail CS. The potential drop ~10 kV is projected in the tail along the field line up to the distance order of 20 R_E The Ohm's law, $\mathbf{j} = \sigma[\mathbf{E} + \mathbf{V}\times\mathbf{B}/c - \mathbf{j}\times\mathbf{B}/nec + \nabla p_e/ne]$, shows that the earthward electric field can be only the Hall electric field $\mathbf{j}\times\mathbf{B}/nec$. The term ∇p_e can be neglected in the long CS. For the tail length $L\sim20R_E$ and the temperature drop ~1 kV, the electric field appeared due to the temperature gradient does not exceed ~ 10^{-6} V/cm. It is important to emphasize that normal magnetic field components always presented in all CSs in the laboratory simulated magnetosphere and in space. The plasma is definitely accelerated by the $\mathbf{j}\times\mathbf{B}/c$ force.

The tail current density increases during a substorm due to decreasing of CS thickness up to ~ $0.1R_E$. As a result, the $\mathbf{j}\times\mathbf{B}/c$ force increases and produces the accelerated plasma injection into the Earth's magnetosphere. The Hall electric field $\mathbf{j}\times\mathbf{B}/nec$ also increases. For the tail magnetic field, B_t =20 nT, the normal magnetic field component B_n ~ 2 nT in the tail CS, the plasma density n ~ 0.2 cm^{-3}, and the CS thickness at a substorm $\delta = 0.1R_E$ the potential drop at distance $L = 10R_E$ can be estimated as $B_tB_n/(2\pi\delta ne)L$ ~50 kV.

For Hall effect appearance, it is necessary that a considerable part of the current should be transferred by electrons. The principal role of electrons in the current is seen in valuable measurements of ion fluxes in the tail CS of the Earth magnetosphere [5]. The data is acquired from the AMTE/IRM satellite. It has been shown that the ion velocity component, V_{iy}, directed along the current in CS is always very weak, and the earthward ion flux has been detected. This data contradicts the conclusions made in [6, 7] about the current production in the tail CS by ions. The conclusions about the current transferring by ions have been made

from the consideration of ion trajectories in the Harris type CS magnetic field. The inaccuracy of such a conclusion has been established by the analysis of direct measurements of electron fluxes in the geomagnetic CS and the comparison with rot**B** measurements. In the works [8, 9] it has been shown that the basic contribution of the current in CS is due to the electrons.

The independent proof of the Hall effect existence in CS is made in the laboratory experiment [10]. The magnetotail is created by the supersonic and super Afvenic plasma flow interaction with the dipole magnetic field. It has been shown that the Hall electric field generation occurs in the tail CS. The electric field is directed to the dipole. The stream of the ions which have been accelerated by the Hall field enters the strong dipole magnetic field creating a positive space charge accumulation. In this place, the opposite directed electric field is registered.

Another independent evidence of the importance of the Hall effect in the geomagnetic tail has been obtained in [11]. It shows the existence of the anti-earthward current order of 1 MA in the geomagnetic CS.

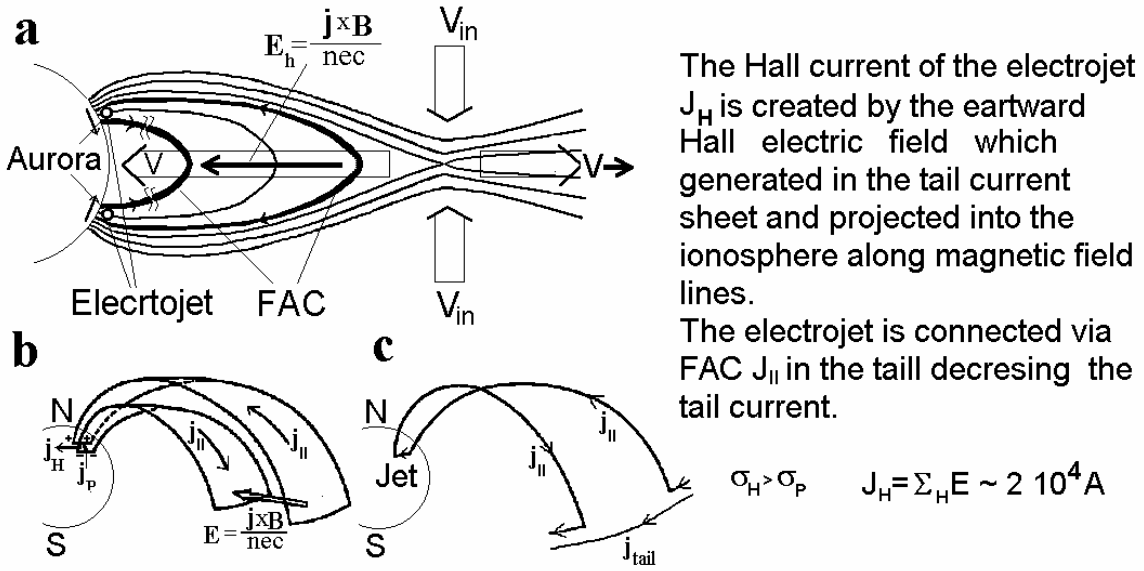

Fig.3. (a) Magnetic field lines and field-aligned currents (thick lines). (b) The layers of field-aligned current and the electrojet. (c) Electrojet connection with the tail current.

Westward Electrojet

The electric field between the layers of opposite directed FAC is perpendicular to the magnetic field. Besides the Pedersen current, it must induce westward Hall current in the ionosphere along the polar oval. The strong FAC appears during a substorm when the IKB-1300 space craft was moved above the chain of IZMIRAN magnetic stations. The westward electrojet is measured by the magnetic stations with the current ~2 10^4 A [3]. The jet is located above the measured ΔB maximum, e.g. between the upward and the downward FAC layers (fig.3b). Here the Hall current $J_H = (c/4\pi)\ (\Sigma_H/\Sigma_p)\ \Delta B$ has to exist., where Σ is the height integrated conductivity. Apparently the ratio Σ_H/Σ_p is increased due to the fast electron precipitation. According to [12] this ratio is $\Delta\Sigma_H/\Delta\Sigma_p \sim W^{5/8}$, where W is the electron energy in keV.

The most probable scheme of the closed auroral electrojet has been offered in [13] (fig.3c). During a substorm the part of the current of CS is connected with the electrojet via FAC, and the dipolization of the Earth's magnetic field occurs.

The Possibility of the Earthward Electric Field Estimated by Using the Ion Drift Approximation

Recently, Zelenyi et al. published the paper [14] in which the other mechanism of the earthward electric field generation in the geomagnetic tail is offered. The two-dimensional stationary existing configuration of the CS with anti-parallel magnetic field lines B_x on which a normal component of the magnetic field B_z is imposed is considered. The two-dimensional stationary existing configuration of the CS with anti-parallel magnetic field lines B_x is considered with the imposed normal magnetic field component B_z. Such artificial configuration exists independently of external conditions (the Earth's magnetic field, the solar wind, etc.). Existence of any external sources of current generation in this magnetic configuration is completely neglected. It is supposed that a stationary CS is created by the current generation inside the sheet, instead of in the boundary layer of the magnetospheric tail, where the current is generated at interaction between the solar wind and the tail magnetic field. It is supposed that current in such CS is created by the electron drift in the crossed fields B_z and E_x. The earthward electric field E_x in CS appears as a consequence of electric field E_z existance directed across a sheet. The X axis is directed to the Earth, and Z axis is directed upwards, perpendicular to the CS. For a generation of the electric field E_x directed to the Earth, the electric field component E_z is set in [15]. As the mechanisms of generation of the electric field E_z across the CS, the gradient of electron pressure across CS is set and pushing out electrons due to the magnetic mirror force is proposed. The electric field E_z, which unequivocally defines a drift of particles in CS, is not connected at all with the mechanism of geomagnetic tail formation at the expense of interaction of the solar wind with the magnetic field of the Earth's dipole. Authors [14] connect the origin of E_z components with potential occurrence ~kT_e,~ 1 kV arising because of "motion of un-magnetized non-adiabatic ions and magnetized electrons in the vicinity of CS central region should be different". In the work [14] for setting the electric field E_z the potential difference across a sheet is estimated from the electron temperature of a hot CS on the basis of two-liquid MHD as ~$kT_e/2e$.The strong temperature gradient can stationary exist only at strong energy dissipations. However, within the limits of used drift approach, the energy dissipation is completely absent. Strong energy dissipation is inconsistent with the conditions of collisionless. In [14] it is affirmed correctly that the magnetic field configuration of CS cannot be influenced by the electric field distribution in CS, if the magnetic field is independent on X. However, Zelenyi et al. [14] supposed, if the normal magnetic field component depends on X, the electric field distribution should be changed, and the electric field component E_x directed to the Earth will arise. The scheme [14] (fig.4) gives the relationship $E_x' = E_x + \frac{\partial(\Delta S)}{\partial \varphi}\frac{\partial \varphi}{\partial S}$ from which E_x directed to the Earth has been estimated. Here, S is the coordinate along the magnetic field line, and φ is the potential. E_x is directed to the Earth. The second term describes the electric field directed to the Earth that was calculated under the assumption that the potential drops on ΔS_1 and ΔS_2 are different. In the written formula, the physically un-defensible assumption is made. It is assumed that the electric field component, directed along the magnetic field line, $\partial\varphi/\partial s$, is invariant at any change of the inclination of the magnetic field line. The further calculation with the use of such CS model gives value E_x ~ 1 mV/m in this CS configuration. Zelenyi et al. [14] conclude that the electric field E_x directed to the Earth obtained by such a way is a hidden one. It cannot influence plasma outside the sheet and create FAC. The assumption that $\partial\varphi/\partial s$, is invariant at any change of the inclination of the magnetic field line is wrong, $d\varphi/ds$ changes with the inclination of the magnetic field line. Namely, $\partial\varphi/\partial s = (\partial\varphi/\partial z)\cos\alpha$, where α is the angle of inclination of the magnetic line to the Z axis. Instead of relationships among φ_1', φ_1, φ_2' and φ_2 written in fig. 4 it should be written: $\varphi_1' = \varphi_1+(\partial\varphi/\partial s)_1 \Delta s_1$; $\varphi_2'=\varphi_2+(\partial\varphi/\partial s)_2$

Δs_2 , where $(\partial\varphi/\partial s)_1=(\partial\varphi/\partial z)(\Delta z/\Delta s_1)$, $(\partial\varphi/\partial s)_2=(\partial\varphi/\partial z)(\Delta z/\Delta s_2)$. It means that $\varphi_2'-\varphi_1' = \varphi_2-\varphi_1$, so $E_x'=E_x=const=0$, the electric field E_x must not appear in such conditions.

As an additional mechanism connecting with increase of the earthward electric field E_x, in [14] is considered plasma drift to the Earth. For this purpose, the existence of E_y field component is also introduced, but in this case energy dissipation ($E_yJ_y > 0$) is inconsistence with the collisionless plasma. It is proposed that the ion drift velocity is bigger than the electron drift velocity: $V_{xi} - V_{xe} = \Delta V_x \sim \rho_i^2\nabla^2 (E_y/B_z)$. However, ions moving forward create the field of polarization directed not to the Earth, but from the Earth! Therefore, the account of the fast ion drift will lead to the reduction of the field directed to the Earth, or to change of the electric field direction on the opposite. Thus, within the frame of drift approach, it is impossible to estimate not only the electric field value along CS, but also field direction.

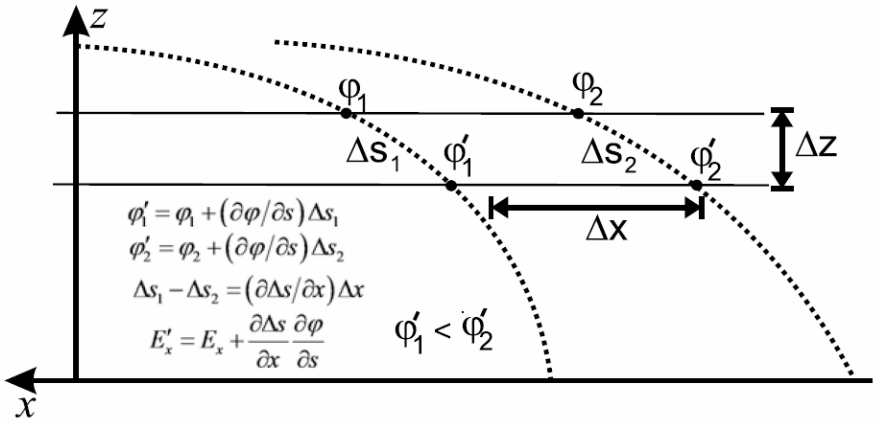

Fig.4. Magnetic field lines (broken lines) and potential drops in CS according to [14].

The drift approach used in [14] is useful only for rough estimates of plasma behavior. However, it does not consider several effects of basic plasma physics. It does not consider the force of magnetic tension in the real CS, forces of inertia and a pressure gradient counteract. In the absence of such forces, a magnetic configuration must turn in the potential one. In the Zelenyi model, only electrons are connected with magnetic field lines (magnetized). This means that the force of a magnetic tension is enclosed to the electrons. Forward electron motion induces electric charge polarization. Due to the plasma polarization, the electric field directed to the Earth is created. Thus, the Hall effect, which is absent in drift approach, is gracefully described in magnetohydrodynmics by the formula $E = j\times B/nec$.

Conclusion

Measurements performed on the spacecraft (space craft) IKB-1300 show that field-aligned currents generation during the substorm takes place in the current sheet of geomagnetic tail. The field-aligned currents have to be generated by Hall electric field, if the current in the sheet is carried by electrons. It is shown in [8, 9] that the current in the sheet is carried by electrons. It is contrary to previously made erroneous conclusions in [6, 7] based on consideration of the motion of particles in the current sheet in the drift approximation.

Application of the drift approximation assumes the conditions of collisionless, i.e. absence of energy dissipation including heating due to anomalous resistivity in CS. However, using the drift approximation the existence of strong temperature gradient across CS is assumed in [14]. This gradient indicates efficient energy dissipation. Existence of a temperature gradient contradicts the requirement of the drift approximation applicability.

The earthward electric field in the geomagnetic tail is a result of plasma polarization due to the $F=j\times B/c$ force applied to electrons. This electric field is responsible for FAC and westward electrojet creation.

References

[1] Israelevich P.L., Ershkovich A.I. Bifurcation of the tail current sheet and ion temperature anisotropy // Annales Geophysicae. – 2008. – 26(7). – P:1759-1765.
[2] Podgorny I.M., Dubinin E.M., Israilevich P.L. Nicolaeva N.S. Large-scale structure of the electric field and field-aligned currents in the auroral oval from the Intercosmos-Bulgaria satellite data // GRL. – 1988. – 15(12). – P:1538-1540.
[3] Dubinin E.M., Israilevich P.L., Kuzmin A.K., Nicolaeva N.S. Podgorny I.M., Zayzev A.N., Petrov V.G. Electrodynamics of midnight aurora oval in weak disturbed period // Kosmicheskie Issledovaniia. - 1987. – 25(2). – P:223-227.
[4] Harel M., Wolf R.A., Reiff P.H., Spiro R.W., Burke W.J., Rich F.J., Smiddy M. Quantitative simulation of a magnetospheric substorm. I - Model logic and overview // JGR. – 1981. – 86(4). – P:2217-2241.
[5] Baumjohann W., Paschmann G., Luehr H. Characteristics of high-speed ion flows in the plasma sheet // JGR. – 1990. - 95(4). - P:3801-3809.
[6] Zelenyi L.M., Delcourt D.C., Malova H.V., Sharma A.S., Popov V.Yu., Bykov A.A. Forced current sheets in the Earth's magnetotail: Their role and evolution due to nonadiabatic particle scattering // Adv. Space Res. – 2002. – 30(7). – P:1629-1638
[7] Sitnov M.I., Zelenyi L.M., Malova H.V., Sharma A. S. Thin current sheet embedded within a thicker plasma sheet: Self-consistent kinetic theory // JGR. – 2000. – 105(A6). – P:13029-13044.
[8] Runov A., Sergeev V.A., Nakamura R., at al. Local structure of the magnetotail current sheet: 2001 Claster observations // Annales Geophysicae. – 2006. – 24(1). – P:247-262.
[9] Israelevich P.L., Ershkovich, A.I., Oran R. Current carriers in the bifurcated tail current sheet: Ions or electrons? // JGR. - 2008. – 113(A4). – P:A04215(1-8).
[10] Minami S., Podgorny A.I., Podgorny I.M. Laboratory evidence of earthward electric field in the magnetotail current sheet // GRL. – 1993. – 20(1). – P:9-12.
[11] Israelevich P.L., Ershkovich A.I., Tsyganenko, N.A. Magnetic field and electric current density distribution in the geomagnetic tail, based on Geotail data // JGR. – 2001. – 106(A11). – P:25919-25928.
[12] Reiff P.H. Models of auroral-zone conductances // Geophys. Monograph. Ser. Vol. 28. AGU. Ed. by Poterma, T.A.: 1984, Chapman Conference. Washington, DC, P:180-191.
[13] McPherron R.L., Russell C.T., Aubry M.P. Satellite studies of magnetospheric substorms on August 15, 1968: 9. Phenomenological model for substorms // JGR. - 1973. – 78(15). – P:3131.
[14] Zelenyi L.M., Artemyev A.V., Petrukovich A.A. Earthward electric field in the magnetotail: Cluster observations and theoretical estimates // JGR - 2010. – 37(6). – L06105(1-4).
[15] Zelenyi L.M., Artemyev A.V., Petrukovich A.A. Electric field Ex in thin current sheets. - 2010 - http://solarwind.cosmos.ru/news.htm.

Author's index